eXPRESS Polymer Letters Vol.3, No.8 (2009) 469
Available online at www.expresspolymlett.com
DOI: 10.3144/expresspolymlett.2009.57

Editorial corner – a personal view
Challenge with the scatter in ductile to brittle transition fracture transition of polymers

*P. M. Frontini**

Instituto de Ciencia y Tecnología de Materiales (INTEMA), CONICET Universidad Nacional de Mar del Plata, Juan B. Justo 4302, B7608FDQ Mar del Plata, Argentina

It is well known that the mechanical behaviour of a plastic component is determined by several factors like deformation rate, material composition, design, processing, and service conditions. Many commercially significant polymers exhibit abrupt changes in fracture behavior from ductile to brittle – or vice versa – over relatively narrow intervals of test or structural variables. The discontinuous transition from unstable to stable crack propagation has been described as 'brittle to ductile transition'. Conversely, within the ductile-to-brittle region materials display mixed ductile and brittle behaviour. This pattern is characterized by a broad distribution of failure energies. The scatter does not arise from differences in specimen preparation or in testing procedures, but because both brittle and ductile failure micromechanisms occur simultaneously. Consequently, plastic parts exhibit a random spatial fluctuation of material toughness characteristics. Although plenty of research has been devoted into trying to understand the role of the different parameters contributing to this phenomenon, a consistent fundamental model in which to base the interpretation of empirical data regarding this transition is still absent. The inherent scatter in toughness values displayed by polymers within ductile-brittle transition has been rarely reported on in the specific literature nor has it been taken into account in fracture mechanics determinations. Assuming that the fracture resistance can be measured in terms of a single critical parameter, this problem is not amenable to a conventional linear and non-linear fracture mechanics analysis. When scatter is considered, a single average toughness parameter fails to describe properly the experimental results. Nowadays, new methodologies and strategies, based on micromechanical analysis of materials, have been developed. They have demonstrated to be of use in characterizing and interpreting the inherent scatter of fracture energy values in other engineering materials which show a similar phenomenon. These approaches require to know the full micromechanisms acting during crack propagation and the modifications in the stress field ahead of a propagating crack. This type of knowledge in the field of integral structural of polymer parts is still incipient. It is my belief that such investigations will contribute to understand and model ductile to brittle fracture transition in plastics, and to give insight into the difficult problem of transferring laboratory results to real applications. Therefore, new plastic parts with improved fracture performance and enhanced reliability can be produced in the near future.

Prof. Dr. Patricia Maria Frontini
Member of International Advisory Board

*Corresponding author, e-mail: pmfronti@fi.mdp.edu.ar

eXPRESS Polymer Letters Vol.3, No.8 (2009) 470–476
Available online at www.expresspolymlett.com
DOI: 10.3144/expresspolymlett.2009.58

Environment-friendly synthesis of long chain semiaromatic polyamides

*W.-Z. Wang, Y.-H. Zhang**

College of Material Science and Engineering, South China University of Technology, 381 Wushan Road, Guangzhou 510640, P. R. China

Received 24 March 2009; accepted in revised form 17 May 2009

Abstract. Long chain semiaromatic polyamides were synthesized by the reactions of p-phenylenediacetic acid with long chain aliphatic diamines, and characterized by Fourier transform infrared spectroscopy (FTIR) and by proton nuclear magnetic resonance (^{1}H NMR). The thermal behaviors were determined by differential scanning calorimetry (DSC) and thermogravimetric analysis (TGA). The solubility, dynamic mechanical, physical and mechanical properties of the polyamides were also investigated. The resultant polyamides have intrinsic viscosity ranging from 1.8 to 2.1 dl·g^{-1}, their melting temperatures range from 254 to 290°C, and their glass transition temperatures obtained from dynamic mechanical analysis are in the range 87–113°C. The physical and mechanical properties of long chain semiaromatic polyamides were compared with those the PA9T. The results show that the heat resistance and the mechanical properties of poly(decamethylene-p-phenylenediacetamide) (PA10P) are near to those of PA9T, so PA10P is a promising heat resistant engineering plastic.

Keywords: *polymer synthesis, long chain diamine semiaromatic nylon*

1. Introduction

Polyamides, also known as nylons, are a class of engineering thermoplastics that play an important role in modern industrial and commercial applications [1]. They can be economically produced by melt processing, but their poor dimensional stability and thermal properties impose limitations on successful applications in some industrial and other fields, especially in the surface mount technology (SMT) and the shell of automobile engine. For improving the heat resistance and strength of polyamides, aromatic rings were incorporated into the backbone of them [2–10]. According to these strategies, lots of aromatic and semiaromatic polyamides are commercially available, such as poly(p-phenylene terephthalamide) (PPTA) [11], Poly(m-phenyleneisophthalamide) (PMIA) [12], poly(hexamethyleneterephthalamide) (PA6T) [13], poly(hexamethyleneisophthalamide) (PA6I) [14, 15], poly(nonamethylene-terephthalamide) (PA9T) [16–19]. These aromatic and semiaromatic polyamides have been noted for their high thermal stability, chemical resistance, high strength, and high modulus as fibers. However, it is impossible to produce them except for PA9T by melting process due to their high glass transition and melting temperatures. So authors prepared aromatic and semiaromatic polyamides based on p-phenylenediacetic acid and 2,6-naphthalenedicarboxylic acid [20–22], however few people prepared long chain semiaromatic polyamides based on p-phenylenediacetic acid. These polyamides could have good physical and mechanical properties, good flow and low water-absorbance therefore, it is of great significance to synthesize novel long chain semiaromatic polyamides based on p-phenylenediacetic acid.

*Corresponding author, e-mail: pszhyhua@scut.edu.cn

We have synthesized semiaromatic polyamides based on p-phenylenediacetic acid and decanediamine [23]. In this contribution, we synthesized a series of novel semiaromatic polyamides: poly (decamethylene-p-phenylenediacetamide) (PA10P), poly(undecanediamine p-phenylenediacetic amides) (PA11P), poly(dodecanediamine p-phenylenediacetic amides) (PA12P) and poly(tridecanediamine p-phenylenediacetic amides) (PA13P) by using 1,10-decanediamine, 1,11-undecanediamine, 1,12-dodecanediamine, 1,13-tridecanediamine and respectively. The long chain diamines are prepared from the corresponding long chain diacids by cyanating and aminating subsequently, which can be facilely obtained from light wax. The resultant polyamides were investigated by Fourier transform infrared spectrum (FTIR) and nuclear magnetic resonance (^{1}H NMR), thermal analysis, physical and mechanical properties, and dynamic mechanical analysis (DMA).

2. Experimental

2.1. Materials

p-Phenylenediacetic acid was purchased from Beijing Yanshan Lithification Chemical Co. Ltd (China) and 1,10-decanediamine, 1,11-undecanediamine, 1,12-dodecanediamine, 1,13-tridecanediamine were provided commercially by Zibo Guangtong Chemical Co. Ltd (China). They were purified by vacuum distillation before use.

2.2. Synthesis

PA10P was synthesized as follows (Figure 1). 1,10-decanediamine (258 g, 1.5 mol) was dissolved in distilled water (1000 ml) at 70°C. Then the solution was added slowly into 500 ml distilled water mixture of p-phenylenediacetic acid (291.2 g, 1.5 mol) with vigorous stirring and then stirred for 120 min at 85–95°C. The white 1,10-decanediamine-p-phenylenediacetic acid salt (PA10P salt) precipitated from the solution was filtered over a Buchner funnel and then repeatedly washed with distilled water. After drying in a vacuum desiccator for 12 h, the salt was obtained as a white powder (476.6 g, 94%).

PA10P salt (476.6 g) was added into an autoclave and distilled water (400 g) was added to reduce volatilization of diamine during the polymerization. The autoclave was filled with carbon dioxide at room temperature and then heated to 220°C meanwhile the pressure up to 2.3 MPa. After 2 h, the pressure of the autoclave was gradually decreased to atmospheric pressure in 2 h by deflating and the reaction temperature of the autoclave was increased to 240°C. After reaction for another 2 h, the prepolymer of PA10P was obtained (433.6 g, 91%, intrinsic viscosity $[\eta] = 1.3$ dl·g^{-1}, $T_m = 279$°C).

The prepolymer of PA10P was added into a solid-state polymerization kettle. Then, the kettle was evacuated to 10 Pa and the reaction temperature was increased to 220°C. After 24 h, the kettle was cooled to room temperature and the high molecular weight of PA10P was obtained (412 g, 95%, $[\eta] = 2.1$ dl·g^{-1}, $T_m = 290$°C).

PA11P, PA12P and PA13P were prepared by the similar procedures with 1,11-undecanediamine, 1,12-dodecanediamine, and 1,13-tridecanediamine instead of 1,10-decanediamine, respectively.

2.3. Characterization

The polyamides were characterized by FTIR, ^{1}H NMR, intrinsic viscosity, DSC, DMA and TGA. The physical and mechanical properties were also investigated.

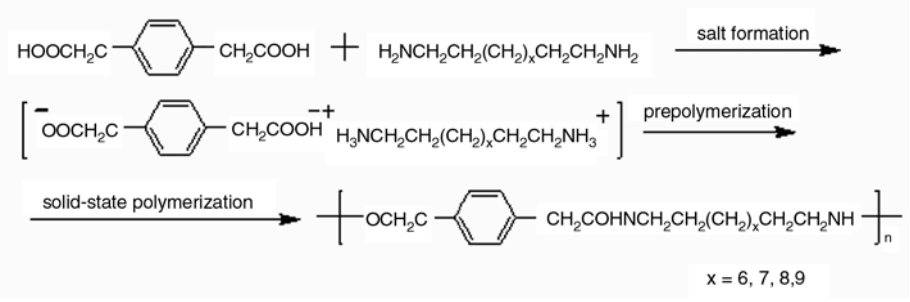

Figure 1. Synthesis routes of the obtained polyamides

The intrinsic viscosities of the polyamides dissolved in concentrated sulfuric acid were determined in an Ubbelohde viscometer at 25 ± 0.1°C. The FTIR spectra were prepared by melting pressed-disc technique on a NICOLET 460 spectrometer. Proton nuclear magnetic resonance spectra were recorded with a Bruker DPX-400 (400 MHz), using deuterated trifluoroacetic acid as solvents and tetramethylsilane (TMS) as an internal reference.

DSC and TGA were carried out in a nitrogen stream using a NETSCH 204 calorimeter with a heating rate of 10°C·min^{-1}. DMA was performed on a NETZSCH DMA-242 apparatus operating in tensile mode at a frequency of 2 Hz in the temperature ranged from –160 to 160°C with a heating rate of 3°C·min^{-1}.

3. Results and discussion

3.1. Syntheses of PA10P, PA11P, PA12P and PA13P

A series of novel high molecular weights semiaromatic polyamides were synthesized by using p-phenylenediacetic acid with long chain diamines. For improving the molecular weights of the polyamides, polyamide salts were prepared beforehand so as to maintain the accurately equal reaction ratio of the diacid and the diamine. It is worth noting that the solvent for the salt forming reaction is water, which is cheaper and environmental friendly compared with ethanol used in preparing other common polyamides. At the stages of the prepolymerization, high vapor pressure was applied to reduce the diamine loss. In the step of solid-state polycondensation, high vacuum was maintained, which is benefit for improving the molecular weights of the polyamides. The molecular weights of the polyamides were characterized by intrinsic viscosities, which are listed in Table 1.

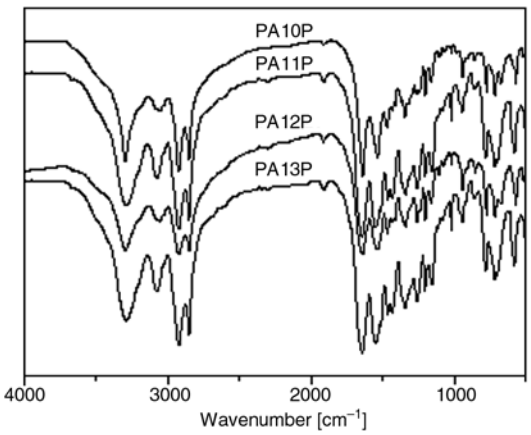

Figure 2. FT-IR spectra of the obtained polyamides

3.2. Fourier transform infrared spectra

FTIR spectra of the PA10P, PA11P, PA12P and PA13P are shown in Figure 2. All the characteristic absorptions of amide groups and methylene segments of polyamide are listed as following: 3301 cm^{-1} (hydrogen-bonded and N–H stretching vibration), 2925 cm^{-1} (N–H in-plane bending vibration and CH_2 vibration), 1647 cm^{-1} (amide I, C=O stretching vibration), 1539 cm^{-1} (amide II, C–N stretching and CO–N–H bending vibration), 1020 cm^{-1} (amide IV, C–CO stretching vibration), 795 cm^{-1} (CH_2 wagging), 716 cm^{-1} (amide V, N–H out-of-plane bending vibration) and 846 cm^{-1} (CH of phenylene vibration).

3.3. Proton nuclear magnetic resonance

Figure 3 presents the proton nuclear magnetic resonance spectra of the resultant polyamides in deuterated trifluoroacetic acid. The chemical shifts in the range at 7.2–7.4 ppm (4H) are attributed to the aromatic protons (position *a*). The chemical shifts at 3.9–4.1 ppm (4H) originate from the protons of methylene adjacent to aromatic ring at the position *b* while that at 3.4–3.6 ppm (4H) come from

Table 1. The physical and mechanical properties of the obtained polyamides compared to PA9T

	PA10P	PA11P	PA12P	PA13P	PA9T
density [g·cm^{-3}]	1.13	1.12	1.10	1.09	1.14
intrinsicviscosity [dl·g^{-1}]	2.1	1.9	2.0	1.8	–
water absorption [%]	0.14	0.14	0.12	0.11	0.17
melting temperature [C°]	290	279	270	254	308
glass transition temperature [°C]	113	102	96	87	126
tensile strength [MPa]	89	86	85	81	92
breaking elongation [%]	42	47	52	63	20
bengding modulus [GPa]	2.4	2.1	2.1	1.9	2.6

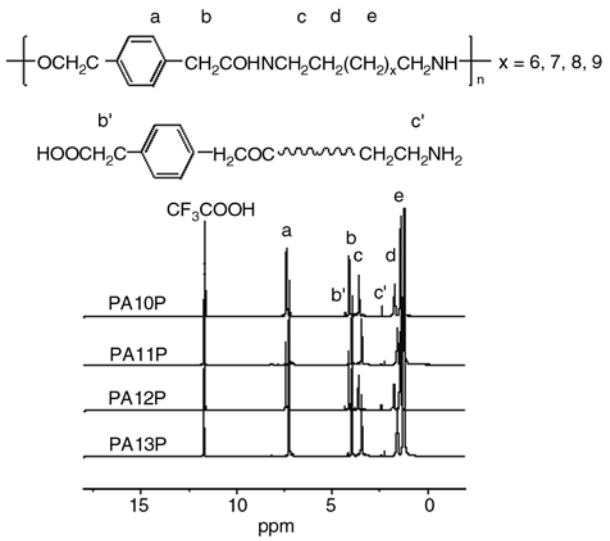

Figure 3. [1]H NMR spectra of the obtained polyamides

the protons of methylene adjacent to NH group at the position *c*. The peak at 1.6–1.7 ppm (4H) belong to protons at the position *d*. The peak at 1.6–1.7 ppm belong to the other protons of the aliphatic chains (position *e*). The peak at 11.6 ppm is attributed to trifluoroacetic acid.

The Chemical Shifts of the proton nuclear magnetic resonance and FTIR spectra of the resultant polyamides agree well with the theoretical values of the title compounds.

3.4. Water absorption of the obtained polyamides

The water absorptions of the obtained polyamides were measured according to ASTM D570 Standard, and the results are listed in Table 1. It can be seen the water absorption of the obtained polyamides decrease slowly with increasing the amount of methylene of polymer backbone, and all of them are lower than that of PA9T. The low water absorption is conducive to maintain dimensional and mechanical stability of products.

3.5. Thermal behaviors

Figure 4 depicts the DSC curves of the polyamides. The obtained polyamides exhibit double-melting endotherms, which is a common phenomenon observed in semicrystalline polymers [24–26]. Additionally, the melting temperatures (T_m) of the polyamides decrease with increasing the amount of methylene of polymeric backbone. PA13P has the

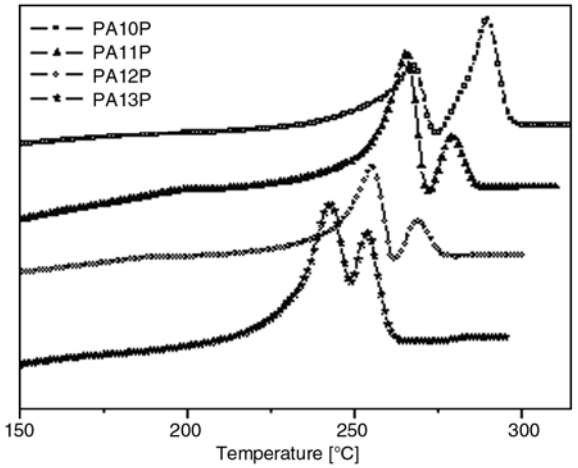

Figure 4. DSC curves of the obtained polyamides

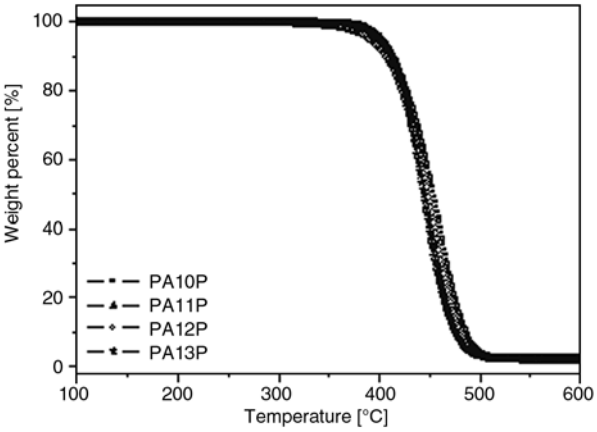

Figure 5. TG curves of the obtained polyamides

lowest melting point among the series of the resultant polyamides. T_m of the PA10P, PA11P, PA12P and PA13P are 290, 279, 270 and 254°C.

TG curves of the resultant polyamides are shown in Figure 5. All the polyamides begin decomposition at *ca*. 426°C, with the framework collapses temperatures (T_d) at *ca*. 482°C, which are higher than those of nylon 66. The results suggest that the thermal stability of the polyamides has been improved by insetting phenylated linkage into the polymeric backbone.

3.6. Dynamic mechanical analysis

DMA was used to characterize the obtained polyamides and the curves are shown in Figure 6. Three obvious transition behaviors can be observed, and are defined as α, β and γ relaxation, respectively. It is well known that the glass transition temperature (T_g) of polyamide can be determined by α relaxation, since it is usually related to the segment

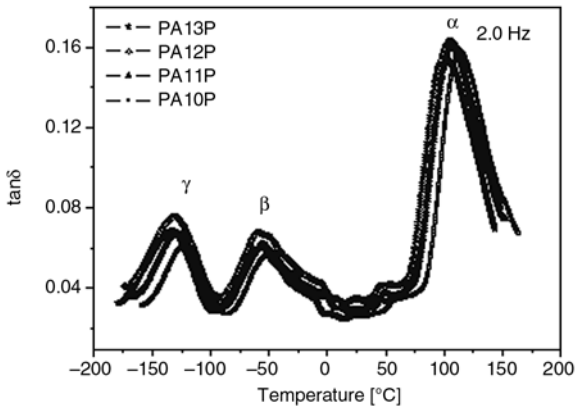

Figure 6. DMA curves of the obtained polyamides

movements in the noncrystalline area [27]. The β relaxation reflects the mobility of carbonyl group of amorphous region, and the γ relaxation reflects the co-moving of amido and methenes. The γ relaxation also reflects the resultant polyamides exhibit fine low-temperature mechanical properties. The temperatures of α relaxation of the polyamides are 113.2, 102.4, 96.5 and 87.1°C, the temperatures of β relaxation are –48.9, –54.1, –56.2 and –60.2°C, and the temperatures of γ relaxation are –122.9, –126.6, –128.8 and –130.6°C. The α, β and γ relaxation temperatures decrease with increasing the amount of methylene of polymeric backbone.

3.7. Mechanical properties

Dry and standard specimens of the obtained polyamides by injection-moulding were prepared and their mechanical properties were measured according to ASTM D638 Standard. From Table 1, it can be observed the tensile strength and bending strength of PA10P are almost the same as that of PA9T at room temperature [28] and water absorption are lower than that of PA9T.

3.8. The solubility of the resultant polyamides

The solubility of the resultant polyamides was tested with different organic solvents which are shown in Table 2. The sample (100 mg) of the polyamides was added into test tube (10 ml) containing appropriate solvent, and the solubility was observed. The resultant polyamides can easily dissolve in acidic solvents such as concentrated sulfuric acid and trifluoroacetic acid (TFA) at room temperature, while they are insoluble in dimethylsulphoxide (DMSO), N,N′-dimethylformamide (DMF), 1-methyl-2-pyrrolidenone (NMP), dimethylacetamide (DMAc), m-cresol, tetrahydrofuran (THF), and chloroform. The result shows that the resultant polyamides exhibit good chemical solvents resistance.

Table 2. The solubility of the obtained polyamides

	PA10P	PA11P	PA12P	PA13P
DMF	–	–	–	–
NMP	–	–	–	–
DMAc	–	–	–	–
DMSO	–	–	–	–
sulfuric acid	+	+	+	+
m-Cresol	+–	+–	+–	+–
pyridine	–	–	–	–
chloroform	–	–	–	–
tetrachloroethane	–	–	–	–
chlorobenzene	–	–	–	–
toluene	–	–	–	–
methanol	–	–	–	–
TFA	+	+	+	+

+: soluble at room temperature, +–: partial soluble at room temperature, –: not soluble at room temperature

4. Conclusions

A series of novel high molecular weights semaiaromatic polyamides including PA10P, PA11P, PA12P and PA13P were synthesized by using p-phenylenediacetic acid with 1,10-decanediamine, 1,11-undecanediamine, 1,12-dodecanediamine and 1,13-tridecanediamine, respectively. FTIR and proton nuclear magnetic resonance spectra confirmed the chemical structure of the prepared polyamides. The thermal, mechanical properties and dynamic mechanical properties were studied. Among the long chain polyamides, the mechanical properties of PA10P achieved the best performance, which are almost the same as those of PA9T. It's worth noting that PA10T can be prepared from convenient raw materials using the environmental friendly solvents (water). Compared to PA9T, the low water absorption and good flexibility of PA10P demonstrates it could be a promising, heat resistant and processable engineering plastic and its applications in wide fields could be desired.

References

[1] Levchik S. V., Weil E. D., Lewin M.: Thermal decomposition of aliphatic nylons. Polymer International, **48**, 532–533 (1999).
DOI: 10.1002/(SICI)1097-0126(199907)48:7<532::AID-PI214>3.0.CO;2-R

[2] Kudo K., Suguie J., Hirami M.: Melt-polymerized aliphthatic-aromatic copolyamides I. Melting points of nylon 66 copolymerized with aromatic diamines and terephthalic acid. Journal of Applied Polymer Science, **44**, 1625–1629 (1992).
DOI: 10.1002/app.1992.070440916

[3] Liu Y., Donovan J. A.: Miscibility and crystallization of semicrystalline nylon 6 and amorphous nylon 6IcoT blends. Polymer, **36**, 4797–4803 (1995).
DOI: 10.1016/0032-3861(95)99295-6

[4] Zhang G. Z., Yoshida H., Kawai T.: Miscibility of Nylon 66 and Nylon 48 blend evaluated by crystallization dynamics. Thermochimica Acta, **416**, 79–85 (2004).
DOI: 10.1016/j.tca.2003.01.002

[5] Khanna Y. P., Murthy N. S., Kuhn W. P., Day E. D.: Pseudo super-miscibility: Blends of semi-crystalline nylon pairs exhibiting a single T_g and a single T_m. Polymer Engineering and Science, **39**, 2222–2232 (1999).
DOI: 10.1002/pen.11610

[6] Brisson J., Breault B.: Miscibility of polyamide blends. 1. Molecular modeling of poly(n-methyleneisophthalamide)-poly(meta-phenyleneisophthalamide) blends. Macromolecules, **24**, 495–504 (1991).
DOI: 10.1021/ma00002a024

[7] Persyn O., Miri V., Lefebvre J-M., Ferreiro V., Brink T., Stroeks A.: Mechanical behavior of films of miscible polyamide 6/polyamide 6I-6T blends. Journal of Polymer Science Part B: Polymer Physics, **44**, 1690–1701 (2006).
DOI: 10.1002/polb.20825

[8] Shibayama M., Uenoyama K., Oura J-I., Nomura S., Iwamoto T.: Miscibility and crystallinity control of nylon 6 and poly(m-xylene adipamide) blends. Polymer, **36**, 4811–4816 (1995).
DOI: 10.1016/0032-3861(95)99297-8

[9] Endo M., Morishima Y., Yano S.,Tadano K., Murata Y., Tsunashima K.: Miscibility in binary blends of aromatic and alicyclic polyamides. Journal of Applied Polymer Science, **101**, 3971–3978 (2006).
DOI: 10.1002/app.22912

[10] Ellis T. S.: Aromatic polyamide blends: Enthalpy relaxation and its correlation with phase phenomena. Macromolecules, **23**, 1494–1503 (1990).
DOI: 10.1021/ma00207a042

[11] Rao Y., Waddon A. J., Farris R. J.: Structure-property relation in poly(*p*-phenylene terephthalamide) (PPTA) fibers. Polymer, **42**, 5937–5940 (2001).
DOI: 10.1016/S0032-3861(00)00905-8

[12] Ferreiro J. J., de la Campa J. G., Lozano A. E., de Abajo J.: Polyisophthalamides with heteroaromatic pendent rings: Synthesis, physical properties, and water uptake. Journal of Polymer Science Part A: Polymer Chemistry, **43**, 5300–5311 (2005).
DOI: 10.1002/pola.21000

[13] Ballistreri A., Garozzo D., Giuffrida M., Maravigna P.: Thermal decomposition processes in aliphatic-aromatic polyamides investigated by mass spectrometry. Macromolecules, **19**, 2693–2699 (1986).
DOI: 10.1021/ma00165a005

[14] Siciliano A., Severgnini D., Seves A., Pedrelli T., Vicini L.: Thermal and mechanical behavior of polyamide 6/polyamide 6I/6T blends. Journal of Applied Polymer Science, **60**, 1757–1764 (1996).
DOI: 10.1002/(SICI)1097-4628(19960606)60:10<1757::AID-APP29>3.0.CO;2-#

[15] Eersels K. L., Groeninckx G.: Influence of interchange reactions on the crystallization and melting behaviour of polyamide blends as affected by the processing conditions. Polymer, **37**, 983–984 (1996).
DOI: 10.1016/0032-3861(96)87281-8

[16] Uddin A. J., Ohkoshi Y., Gotoh Y., Nagura M., Hara T.: Influence of moisture on the viscoelastic relaxations in long aliphatic chain contained semiaromatic polyamide, (PA9-T) fiber. Journal of Polymer Science Part B: Polymer Physics, **41**, 2878–2891(2003).
DOI: 10.1002/polb.10602

[17] Uddin A. J., Ohkoshi Y., Gotoh Y., Nagura M., Hara T.: Melt spinning and laser-heated drawing of a new semiaromatic polyamide, PA9-T fiber. Journal of Polymer Science Part B: Polymer Physics, **42**, 433–444 (2004).
DOI: 10.1002/polb.10710

[18] Uddin A. J., Gotoh Y., Ohkoshi Y., Nagura M., Endo R., Hara T.: Hydration in a new semiaromatic polyamide observed by humidity-controlled dynamic viscoelastometry and X-ray diffraction. Journal of Polymer Science Part B: Polymer Physics, **43**, 1640–1648 (2005).
DOI: 10.1002/polb.20446

[19] Uddin A. J., Ohkoshi Y., Gotoh Y., Nagura M., Endo R., Hara T.: Effects of take-up speed of melt spinning on the structure and mechanical properties of maximally laser drawn PA9-T fibers. International Polymer Processing, **21**, 263–271 (2006).

[20] Ridgway J. S.: Structure-property relationships of ring-containing nylon 66 copolyamides. Journal of Polymer Science Part A-1: Polymer Chemistry, **8**, 3089–3111 (1970).
DOI: 10.1002/pol.1970.150081105

[21] Scandola M., Pizzoli M., Drusiani A., Garbuglio C.: Dynamic mechanical properties and melting pointis of some aliphatic and partially aromtic polyamides. European Polymer Journal, **10**, 101–107 (1974).
DOI: 10.1016/0014-3057(74)90058-5

[22] Yang S. H., Liu M. Y., Wang Y. D., Fu P., Chen Z. Y., Zhang Y. C., Zhao Q. X.: Synthesis and characterization of PA12N (in Chinese). Material Science and Technology, **16**, 117–119 (2008).

[23] Wang W. Z., Liu B. Y., Li R. X., Zhang Y. H.: Synthesis and physical mechanical properties of poly (decanediamine p-phenylenedacetic amide). Polymer Materials: Science and Engineering, **25**, 144–146 (2009).

[24] Li Y. J., Zhu X. Y., Tian G. H., Yan D. Y., Zhou E.: Multiple melting endotherms in melt-crystallized nylon 10,12. Polymer International, **50**, 677–678 (2001).
DOI: 10.1002/pi.682

[25] Ramesh C., Keller A., Eltink S. J.: Studies on the crystallization and melting of nylon 66:3. Melting behaviour of negative spherulites by calorimetry. Polymer, **35**, 5300–5302 (1994).
DOI: 10.1016/0032-3861(94)90483-9

[26] Hybart F. J., Platt J. D.: The melting of 66 nylon: Observations by differential thermal analysis. Journal of Applied Polymer Science, **11**, 1449–1453 (1967).
DOI: 10.1002/app.1967.070110808

[27] Li W. H., Yan D. Y.: Synthesis and characterization of nylons based on hexadecane diacid. Journal of Applied Polymer Science, **88**, 2462–2467 (2003).
DOI: 10.1002/app.12048

[28] Ma J. M., Song S. W., Guo J.: New heat resistance polyamide. Modern Plastics Processing and Applications, **15**, 41–44 (2003).

eXPRESS Polymer Letters Vol.3, No.8 (2009) 477–482
Available online at www.expresspolymlett.com
DOI: 10.3144/expresspolymlett.2009.59

Catalytic effect of carbon nanotubes on polymerization of cyanate ester resins

A. Fainleib[1], *L. Bardash*[1,2*], *G. Boiteux*[2]

[1]Institute of Macromolecular Chemistry of the National Academy of Sciences of Ukraine, 48, Kharkivske shose, 02160 Kyiv, Ukraine
[2]Université de Lyon, Lyon, F-69003, France ; Université Lyon 1, IMP/LMPB Laboratoire des Matériaux Polymères et Biomatériaux, Bât ISTIL, 43 bd du 11 Novembre, Villeurbanne, F-69622, France ; CNRS, UMR5223, Ingénierie des Matériaux Polymères,Villeurbanne, F-69621 , France

Received 9 March 2009; accepted in revised form 20 May 2009

Abstract. Kinetic peculiarities of polycyclotrimerization process of dicyanate ester of bisphenol A (DCBA) in the presence of multi-walled carbon nanotubes (MWCNTs) have been investigated using Fourier Transform Infrared Spectroscopy (FTIR) spectroscopy technique. It has been found that even very small amounts of MWCNTs (0.01–0.1 wt%) catalyze the reaction of polycyclotrimerization of DCBA leading to formation of polycyanurate network (PCN)/MWCNTs nanocomposite. However, some decrease in final degree of conversion for nanocomposites compared to the neat PCN within the temperature/time schedule used was observed. The kinetic rate constants increased with addition of MWCNTs and energies of activation were found to be significantly decreased even at low contents of MWCNTs.

Keywords: *nanocomposites, thermosetting polymers, polycyanurates, carbon nanotubes, sonication*

1. Introduction

Polycyanurates (PCN) offer a variety of excellent thermal and good mechanical properties, which commend them for use in high performance technology (e.g. as matrices for composites for high-speed electronic circuitry and transportation). For the electronics market, attractive features of PCN are their low dielectric loss characteristics, dimensional stability at molten solder temperatures (220–270°C), high purity, inherent flame-retardancy (giving the potential to eliminate brominated flame retardants) and excellent adhesion to conductor metals at temperatures up to 250°C [1]. Since the late 1970s, cyanate ester resins have been used with glass or aramid fibre in high-speed multilayer circuit boards and this remains their primary application. Several reviews [1–5] collected the numerous publications (papers and patents) in the field of PCN synthesis, processing, characterization, modification and application have appeared since 1990s. In addition, like conventional FR-4 diepoxides, cyanate ester laminates retain the desirable (ketone) solution processing characteristics and the ability to be drilled, making it possible to employ them in printed circuit board manufacture. In the last two decades, aerospace composites have evolved into damage-tolerant primary and secondary structures utilizing both thermoset and thermoplastic resins. PCN homopolymers develop approximately twice the fracture toughness of multifunctional epoxies while qualifying for service temperatures of at least 150°C, intermediate between epoxy and bis-maleimides capabilities. PCN have already flown in prototype radomes and high gain antennae, with

*Corresponding author, e-mail: lyubabardash@yahoo.com

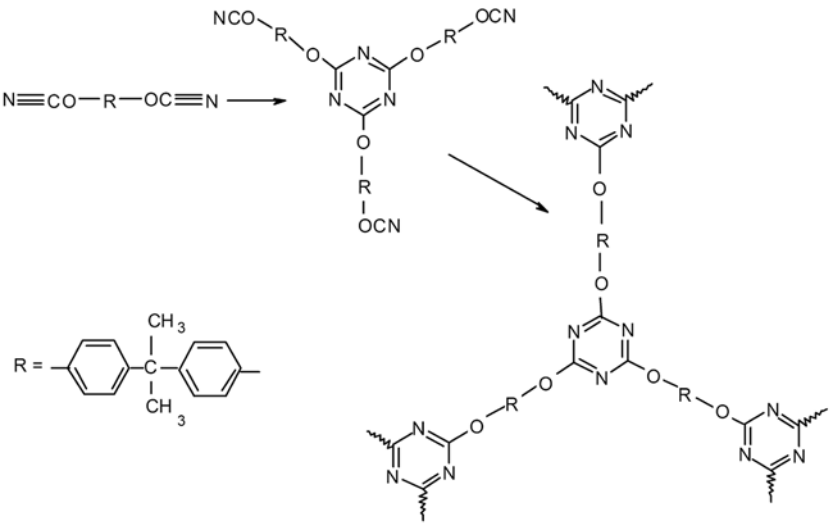

Figure 1. Generalized monomer structure and polycyanurate network formation

possible applications in primary and secondary structures of the High Speed Civil Transport (HSCT) and European Fighter Aircraft. PCN are also being qualified for satellite truss and tube structures and cryogenic, radiation-resistant components in the Superconducting Supercollider [3].

PCN are synthesized by a polycyclotrimerization reaction of cyanate esters (CER) of bisphenols (cf. Figure 1).

In the review [6] the kinetic peculiarities of the homopolycyclotrimerization of cyanate esters (see Figure 1) is analyzed. It is noted that full conversion of the cyanate groups can be achieved at sufficiently high temperature. At this some catalysts are used to accelerate the reaction and to decrease the final temperature of curing. The most popular catalysts are metal acetyl acetonates with nonyl phenol as a co-catalyst.

In our previous works [7, 8] at synthesis of polycyanurate/polyurethane semi-IPNs we have found that the polycyclotrimerization process of cyanate esters is accelerated by polyurethane component. Thus the synthesis was carried out without using any traditional catalysts. Recently [9] at synthesis of polycyanurate/montmorillonite (MMT) nanocomposites we have also demonstrated the catalytic effect of MMT on conversion of cyanate groups.

Zhou *et al.* [10] have reviewed several publications on the effect of unmodified CNTs on the cure reaction of some epoxy systems. The results showed that, at the initial curing stage, MWCNTs act as catalyst and facilitate the curing, moreover, this accelerating effect is already noticeable at the lowest content of MWCNTs investigated (1 wt%).

Few papers were published [11, 12] on synthesis of PCN/CNTs nanocomposites but no information of kinetic effect of CNTs was reported. Tang *et al.* [13] described the kinetics of polymerization of the mixture of epoxy resin and cyanate esters with addition of functionalized MWCNTs. Authors explained the catalytic effect of MWCNTs by the presence of hydroxyl groups on CNTs surface that were formed due to their functionalization. No data on catalytic effect of CNTs on polymerization of cyanate esters have been found in the literature.

Logically, we have decided to check if there is any acceleration at polymerization of cyanate ester in the presence of carbon nanotubes (CNTs). Thus the purpose of this work was study of possible catalytic effect of carbon nanotubes on conversion of cyanate groups at synthesis of PCN/CNT nanocomposites

2. Experimental section

Pre-polymer of 2,2'-Bis(4-cyanatophenyl)isopropylidene (DCBA) was used for PCN synthesis. DCBA was kindly supplied by Lonza Ltd. as Primaset BADCy (purity > 99%) was used as received. The pre-polymer was prepared by heating of DCBA at 150°C for 40 h.

MWCNTs were furnished from TM Spetsmash, Kiev, Ukraine. MWVNTs have outer diameter 10–20 nm, the length is about 100 μm and the specific surface is 0,286 m^2/kg.

The nanocomposites were prepared by sonication of MWCNTs in a liquid pre-polymer at room temperature at 44 Hz during 45 min on the ultrasound equipment UZDN-2E. The step by step curing schedule for all the systems consisted of the following stages: 3 h at 180°C, 1 h at 210°C, 1 h at 230°C, 1 h at 250°C. The concentration of MWCNTs was 0.01 and 0.1 wt%. Kinetic peculiarities of the polymerization reaction were studied by using FTIR spectroscopy technique. FTIR measurements were made by a Bruker TENSOR 37 spectrometer in the range of 4000–500 cm^{-1}. The mixture of MWCNTs dispersed in pre-polymer was deposited between two NaCl windows and the measurements were performed after each stage of curing.

3. Results and discussion

The conversion of cyanate groups was determined from changes of absorbance of the band with maximum at 2236–2272 cm^{-1}, corresponding to the valence vibrations of the –O–C≡N group. As an internal standard band the band at 2968 cm^{-1} of the valence vibrations of CH_3-group in FTIR spectra of the reactive composition was chosen. On Figure 2 the FTIR spectra of DCBA monomer, DCBA pre-polymer and PCN synthesized without using any catalyst are shown. It is seen that at polymerization of the DCBA an intensity of the peaks of cyanate groups at 2236–2272 cm^{-1} decreases and the peaks at 1367 and 1564 cm^{-1} corresponding to polycyanurate cycle [3] appear in the FTIR spectra.

The conversion of resin was calculated using Equation (1):

$$\alpha(t) = 1 - \frac{\dfrac{A_{(t)2236-2272}}{A_{(0)2236-2272}}}{\dfrac{A_{(t)2968}}{A_{(0)2968}}} \tag{1}$$

where $A_{(t)2236-2272}$ is the area under absorbance peak of –O–C≡N at 2236–2272 cm^{-1} at time t; $A_{(t)2968}$ is the area under absorbance peak of $–CH_3$ at 2968 cm^{-1} at time t; $A_{(0)}$ are the areas under absorbance peaks of corresponding groups in initial DCBA monomer.

The conversion of cyanate groups in DCBA pre-polymer was found to be 28% and that in PCN sample – 92.5%. It should be noted here that for achieving full conversion post-curing is needed at 270–300°C even at using conventional catalysts [3].

On Figure 3 the conversion of cyanate groups of DCBA pre-polymer as well as in the presence of the small amounts of MWCNTs *versus* time is shown. The FTIR data evidence an acceleration effect of MWCNTs on kinetics of the early stages of PCN formation. The higher the MWCNTs content in the system the higher the conversion of the cyanate groups into cyanurate cycles at least in the range of the concentrations used. The attempt to study the system with 0.5 wt% of MWCNTs has led to vitrification as early as in a stage of components blending in 2 min after starting ultrasound action.

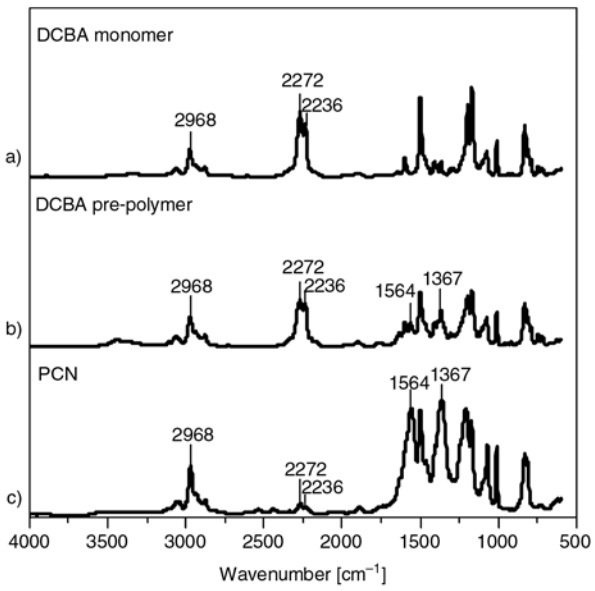

Figure 2. FTIR spectra for a) DCBA monomer; b) DCBA pre-polymer; c) PCN

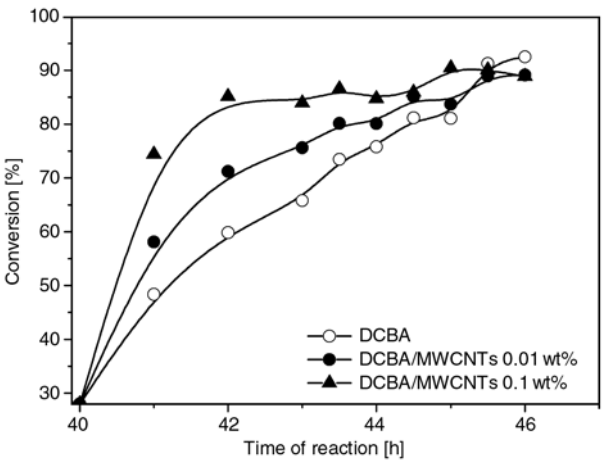

Figure 3. The conversion of DCBA in dependence of reaction time

Table 1. Effect of MWCNTs content in the reactive composition on final conversion of cyanate groups

MWCNTs content [wt%]	Conversion of –O–C≡N groups [%]
0	92.5
0.01	89.1
0.10	88.8

However, as can be seen from Table 1, in spite of the higher reaction speed of polycyclotrimerization process of the cyanate ester in the presence of MWCNTs the final conversion of –O–C≡N groups for the temperature/time schedule used was some lower compared to that for neat PCN.

One can suppose that the acceleration effect of carbon nanotubes on polymerization of cyanate ester is due to adsorption of DCBA pre-polymer molecules on high surface of MWCNTs. However, this phenomenon can play negative role in the final stage of PCN network formation, when some unreacted molecules are not easy accessible, and the probability of elementary reaction act is very low (as can be seen from Figure 1 three molecules of cyanate ester have to meet each other to react with cyanurate cycle formation).

As it was above mentioned this problem can be solved by post-curing of the polymer product at higher temperatures, when the mobility of the reactive molecules and fragments is higher.

The manufacturer of MWCNTs used in this study reports that catalyst residue in MWCNTs is the mixture of SiO_2, Al_2O_3, Fe_2O_3, MoO_3. For the moment, there are no references in the literature that describe the catalytic action of such oxides on reaction of cyclotrimerization of cyanate esters. Normally, reaction of cyclotrimerization of the aryl dicyanates can be catalyzed by the mixture of catalyst and co-catalyst. The most common types of catalyst are carboxylate salts and chelates of transition metal ions (Cu^{2+}, Co^{2+}, Zn^{2+}, Mn^{2+} …) [3] that facilitate the reaction of cyclotrimerization by formation of co-ordination complexes. The co-catalyst serves a dual purpose of acting as a solvent for catalyst and completing ring closure of the triazine ring via hydrogen transfer. The most commonly used co-catalyst is nonylphenol.

The data obtained from FTIR studies for DCBA and DCBA with 0.01 and 0.1 wt% of MWCNTs were analyzed using an empirical Equation 2 [3]:

$$\frac{\partial \alpha}{\partial t} = k(1-\alpha)^n \tag{2}$$

where k is the rate constant and n is the order of overall reaction. The parameters k and n are evaluated from the data region where the reaction rate depends on monomer concentration and sharp increase in conversion is observed. Equation (2) was integrated and fitted to experimental concentration profiles of both the unfilled and the filled with MWCNTs systems. It was observed that the data calculated from FTIR spectra is in a good agreement with Equation (2) when the order of reaction $n = 1$. This means that DCBA or DCBA/MWCNTs systems can be described by a first-order autocatalytic rate law.

The values of the observed rate constants obtained from the first-order reaction analysis for DCBA and DCBA/MWCNTs nanocomposites are listed in the Table 2. The values of kinetic constants for

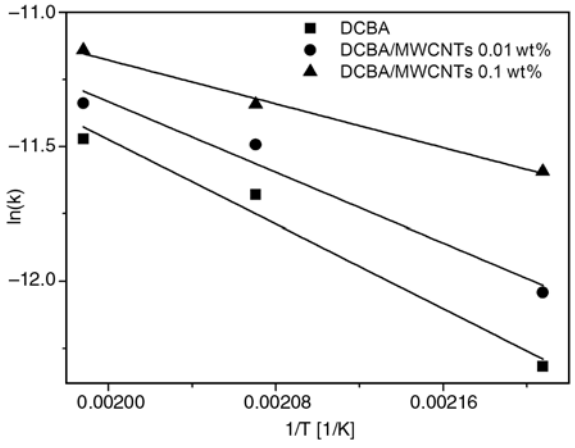

Figure 4. Arrhenius plot for the cure of DCBA and DCBA/MWCNTs

Table 2. Values of the observed rate constants obtained from the first-order reaction analysis for DCBA and DCBA/MWCNTs nanocomposites

Temperature [°C]	Rate constant $k \cdot 10^4$ $(conc.s)^{-1}$		
	DCBA	DCBA/MWCNTs 0.01 wt%	DCBA/MWCNTs 0.1 wt%
150	0.02	0.02	0.02
180	0.05	0.06	0.09
210	0.08	0.10	0.12
230	0.10	0.12	0.14

Table 3. Results of the Arrhenius plot of the first-order reaction analysis for DCBA and DCBA/MWCNTs nanocomposites

MWCNTs content [wt%]	E_a [kJ/mol]	lnA [s^{-1}]
0	32.7	1.3
0.01	27.3	1.6
0.10	16.9	2.0

unfilled DCBA are lower than the values reported for the catalyzed DCBA [14]. The results show that the kinetic constant increases with the addition of MWCNTs on each isothermal step of polymerization of DCBA. The activation energies and pre-exponential factors were determined from Arrhenius plots, shown on Figure 4. A summary of the results is given in Table 3. The activation energies for the reaction ranged from 17 to 33 kJ/mol for pure system of DCBA and for the systems filled with MWCNTs and agree with the values reported earlier [14, 15]. The activation energies for the samples cured with MWCNTs are much lower than the values obtained for virgin DCBA and they decrease with increasing MWCNTs content. This effect is quite similar to the decrease of activation energy with adding catalysts in reactive systems [16].

Presence of low molar mass compounds (for example, conventional catalysts) in polymer networks can influences negatively the thermal properties of the final material. In this work we have shown that synthesis of PCN/CNTs nanocomposites can be effectively realized without using the conventional catalysts.

4. Conclusions

The kinetics of polymerization of DCBA and DCBA containing MWCNTs was investigated by FTIR analysis. It was found that the conversion of –O–C≡N increases significantly with adding of even small quantities of MWCNTs (e.g. 0.01 and 0.1 wt%). However, the final degree of reaction for nanocomposites is slightly decreased in comparison with pure PCN matrix. This can be changed by a post-curing procedure. The reaction of DCBA was determined as the first-order autocatalytic reaction. The rate constants were calculated and they were found to be higher for filled systems in comparison to pure DCBA. The obtained data follows the Arrhenius relationship and activation energies estimated from the Arrhenius plots decrease with the addition of MWCNTs. It has been established that due to catalytic effect of MWCNTs on polycyclotrimerization process of cyanate ester resins the polycyanurate/MWCNTs nanocomposites can be synthesized without application of complicated traditional catalytic systems.

References

[1] Fainleib A. M., Shantalii T. A., Pankratov V. P.: Copolymers of cyanate esters and plastics based on them (in Russian). Polymer Composite Materials, **49**, 39–53 (1991).

[2] Fainleib A. M., Sergeeva L. M., Shantalii T. A.: Triazinecontaining interpenetrating polymer networks (in Russian). Polymer Composite Materials, **50**, 63–72 (1991).

[3] Hamerton I.: Chemistry and technology of cyanate ester resins. Chapman and Hall, Glasgow (1994).

[4] Hamerton I., Hay J. N.: Recent technological developments in cyanate ester resins. High Performance Polymers, **10**, 163–174 (1998).
DOI: 10.1088/0954-0083/10/2/001

[5] Nair C. P. R., Mathew D., Ninan K. N.: Advantages in cyanate ester resins. Advances in Polymer Science, **155**, 1–99 (2000).
DOI: 10.1007/3-540-44473-4_1

[6] Bauer M., Bauer J.: Aspects of the kinetics, modeling and simulation of network build-up during cyanate ester cure. in 'Chemistry and technology of cyanate ester resins' (ed.: Hamerton I.) Chapman and Hall, Glasgow, 58–85 (1994).

[7] Fainleib A. M., Novikova T. I., Shantalii T. A., Sergeeva L. M.: Kinetic of formation semi-interpenetrating polymer networks based on crosslinked polycyanurate and linear polyurethane. Polymer Science Series B, **33**, 60–67 (1992).

[8] Fainleib A. M., Novikova T. I., Shantalii T. A., Sergeeva L. M.: Synthesis, structure and some properties of the polycyanurate-polyurethane semi-IPNs. Polymeric Materials: Science and Engineering, **66**, 131–132 (1992).

[9] Fainleib A. M., Bei I.: Influence of montmorillonite on curing kinetics of dicyanate ester of bisphenol A. Reports of the National Academy of Sciences of Ukraine, **7**, 157–161 (2006).

[10] Zhou T., Wang X., Liu X., Xiong D.: Influence of multi-walled carbon nanotubes on the cure behavior of epoxy-imidazole system. Carbon, **47**, 1112–1118 (2009).
DOI: 10.1016/j.carbon.2008.12.039

[11] Fang Z., Wang J., Gu A.: Structure and properties of multiwalled carbon nanotubes/cyanate ester composites. Polymer Engineering and Science, **46**, 670-679 (2006).
DOI: 10.1002/pen.20487

[12] Hopkins R., Lipeles R. A.: Preparation and characterization of single wall carbon nanotube-reinforced polycyanurate nanocomposites. Polymer Preprints, **46**, 787 (2005).

[13] Tang Y-S., Kong J., Gu J-W., Liang G-Z.: Reinforced cyanate ester resins with carbon nanotubes: Surface modification, reaction activity and mechanical properties analyses. Polymer-Plastics Technology and Engineering, **48**, 359–366 (2009).
DOI: 10.1080/03602550902725340

[14] Li W., Ling G., Xin W.: Triazine reaction of cyanate ester resin systems catalyzed by organic tin compound: Kinetics and mechanism. Polymer International, **53**, 869–876 (2004).
DOI: 10.1002/pi.1446

[15] Osei-Owusu A., Martin G. C., Gotro J. T.: Catalysis of cyclotrimerization of cyanate ester resin systems. Polymer Engineering and Science, **32**, 535–541 (1992).
DOI: 10.1002/pen.760320805

[16] Carey F. A., Sundberg R. J.: Advanced organic chemistry- Part A: Structure and Mechanisms. Springer Verlag, Berlin (2007).

eXPRESS Polymer Letters Vol.3, No.8 (2009) 483–491
Available online at www.expresspolymlett.com
DOI: 10.3144/expresspolymlett.2009.60

Preparation of fluorescent DNA probe by solid-phase organic synthesis

Z. Dai, P. Li, X. X. Sun, J. M. Zhang, S. C. Xu, N. Guo, X. Wang*

Tianjin Key Laboratory of Fiber Modification and Functional Fiber, School of Environment and Chemical Engineering, Tianjin Polytechnic University, 300160 Tianjin, China

Received 12 April 2009; accepted in revised form 20 May 2009

Abstract. Fluorescent DNA probe based on fluorescence resonance energy transfer (FRET) was prepared by solid-phase organic synthesis when CdTe quantum dots (QDs) were as energy donors and Au nanoparticles (AuNPs) were as energy accepters. The poly(divinylbenzene) core/poly(4-vinylpyridine) shell microspheres, as solid-phase carriers, were prepared by seeds distillation-precipitation polymerization with 2,2′-azobisisobutyronitrile (AIBN) as initiator in neat acetonitrile. The CdTe QDs and AuNPs were self-assembled on the surface of core/shell microspheres, and then the linkage of CdTe QDs with oligonucleotides (CdTe-DNA) and AuNPs with complementary single-stranded DNA (Au-DNA) was on the solid-phase carriers instead of in aqueous solution. The hybridization of complementary double stranded DNA (dsDNA) bonded to the QDs and AuNPs (CdTe-dsDNA-Au) determined the FRET distance of CdTe QDs and AuNPs. Compared with the fluorescence of CdTe-DNA, the fluorescence of CdTe-dsDNA-Au conjugates (DNA probes) decreased extremely, which indicated that the FRET occurred between CdTe QDs and AuNPs. The probe system would have a certain degree recovery of fluorescence when the complementary single stranded DNA was introduced into this system, which showed that the distance between CdTe QDs and AuNPs was increased.

Keywords: *nanocomposites, fluorescent DNA probe, FRET, microspheres, solid-phase organic synthesis*

1. Introduction

Fluorescent DNA probe is known as DNA biosensor based on fluorescence resonance energy transfer (FRET) which occurs when the electronic excitation energy of a donor chromophore is transferred to an acceptor molecule nearby via a through-space dipole–dipole interaction between the donor-acceptor pair [1]. The strong distance-dependence of the FRET efficiency has been widely exploited in studying the structure and dynamics of proteins and nucleic acids, in the detection and visualization of intermolecular association and in the development of intermolecular binding assays [2].

As novel luminescent inorganic fluorophores, Quantum dots (QDs) are currently being widely used in biological probes, *in vitro* assay detection, *in vivo* cell labeling and imaging, because QDs show a broad and continuous excitation spectrum, narrow size-tunable symmetric emission spectrum and high fluorescence quantum yield [3–8]. Recently, complex nanostructures formed by linking QDs as energy donors and gold nanoparticles (AuNPs) as energy acceptors through DNA hybridization or streptavidin-biotin interaction have also been realized [9–13] and applied in the sensing biomolecular concentration [10]. AuNPs have a high extinction coefficient and a broad absorption spectrum in visible light that is overlapped by the emission wavelength of the usual energy donors. The key challenge of the hybrid DNA probe is to immobilize single-stranded DNA

*Corresponding author, e-mail: daizhao@gmail.com

(ssDNA) onto the surfaces of QDs and AuNPs, respectively. The Gueroui and Libchaber [11] reported that carboxyl-modified QDs, activated with 1-ethyl-3-(3-dimethylaminopropyl) carbodiimide hydrochloride (EDC) and sulpho N-hydroxysuccinimide (NHS), could be covalently linked to ssDNA, streptavidin-coated QDs also could be conjugated with ssDNA [9]. ssDNA modified AuNPs were achieved by ssDNA being covalently linked to AuNPs functionalized with a single NHS ester [11, 14]. In our previous works, we utilized the self-assembly of mercapto group modified ssDNA (HS-DNA) on AuNPs to simplify the process of probe preparation, and prepared DNA probe by the hybridization between QDs linked with a DNA sequence and AuNPs with a DNA strand [15]. However, because QDs and AuNPs both were less than 20 nm in diameters, it was hard to separate DNA probe from this mixture system. In reported works, the amount of nanoparticles (QDs or AuNPs) exceeded that of DNA [11, 15], thus less unreacted DNA would exist in system and the separation and purification of ssDNA conjugated AuNPs (Au-DNA) and QDs (QD-DNA) from reaction system could be mainly focused on the utilization of the differences between free nanoparticles and ssDNA conjugated nanoparticles. In traditional way, nanoparticles which were not linked to DNA were not subject to purification processes [12, 15] or removed by ethanol precipitation [11] or spin filtration [13], and so on. Free ssDNA and nanoparticles which remained in system would influence the precision of detection and repetition ability of DNA probe. On the other hand, the structures of ssDNA conjugated AuNPS (Au-DNA) and QDs (QD-DNA) and hybridized double-stranded DNA (dsDNA) probe were very complicated. Fu *et al.* [9] confirmed that a CdTe QD could be conjugated with 1 to 4 ssDNA, which resulted in the differences of the solubility and molecular weight of QD-DNA with different DNA number. Therefore, a more effective purification way with another mechanism should be investigated.

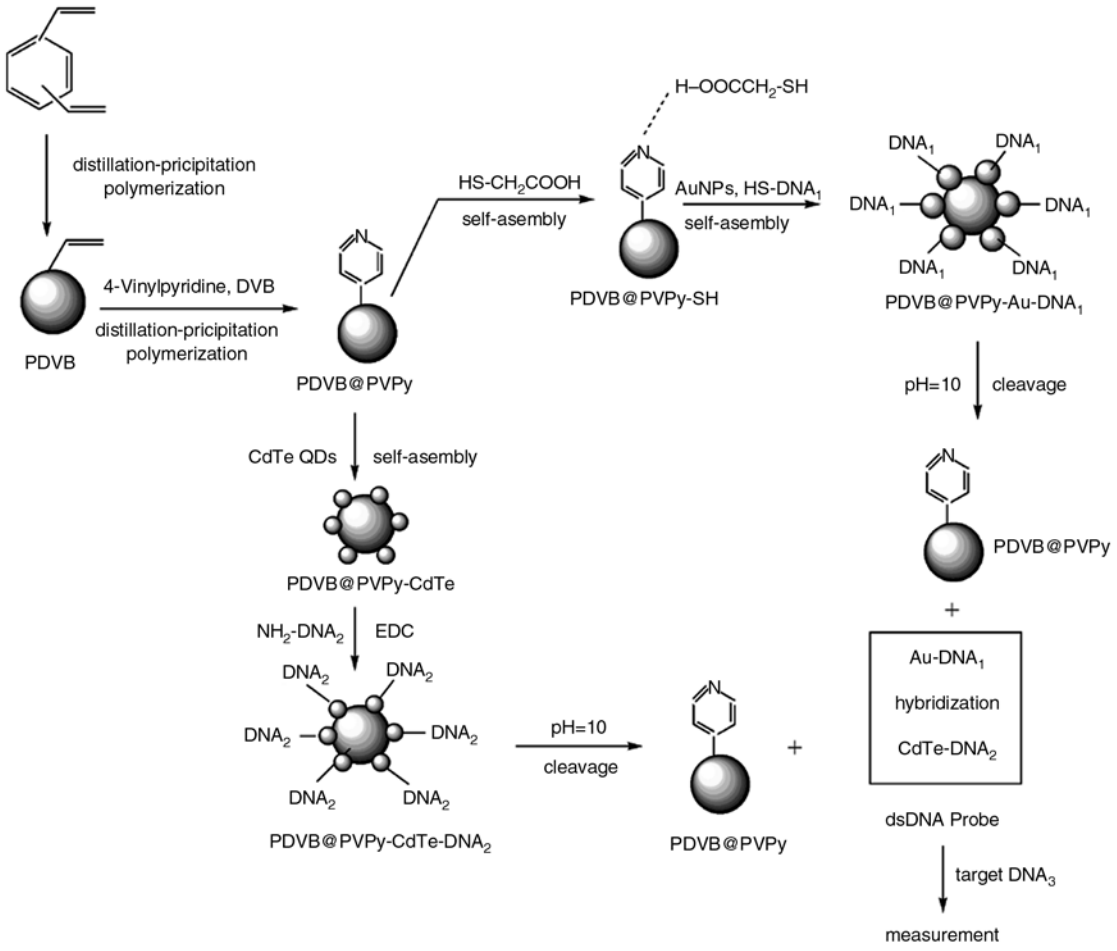

Figure 1. Illustration of preparation of fluorescent DNA probe on microspheres, and the base sequence of DNA_2 was complementary with the base sequence of DNA_1

The objective of the present work was to utilize functional polymeric micospheres as solid-phase carriers to simplify the process of probe purification. Because of the larger size of carriers, the free ssDNA and nanoparticles could be removed by filtration or centrifugation easily. The whole process was shown in Figure 1. Poly(divinylbenzene-80) (PDVB) microspheres as cores prepared by distillation-precipitation polymerization had a large average particle size (>1 μm), which could be purified easily, and poly(4-vinylpyrindin) (PVPy) was coated on the PDVB core when PDVB microspheres were as seeds, 4-vinylpyrindin (VPy) as monomer and divinylbenzene-80 (DVB) as crosslinker by seeds distillation-precipitation polymerization. The ssDNA modified nanoparticles (Au-DNA and QD-DNA) were completed on the surface of PDVB/PVPy core/shell microspheres by self-assembly respectively. Only simple filtration or ultracentrifugation could remove the free ssDNA and nanoparticles because of the heterogeneous characteristic of solid-phase organic synthesis. The double-stranded DNA (dsDNA) probe was obtained when Au-DNA and CdTe-DNA were cleaved from the solid-phase carriers and hybridized each other.

2. Experimental

2.1. Materials

Divinylbenzene-80 (DVB, 80% divinylbenzene isomers) was supplied by Aldrich Chemical Co. It was washed with 5% aqueous sodium hydroxide, water and then dried over anhydrous magnesium sulfate prior to use. 4-vinylpyrindin (VPy) was obtained from Aldrich Chemical Co. and purified by vacuum distillation before use. 2,2′-Azobisisobutyronitrile (AIBN) was analytical grade available from Tianjin Xida Rare Chemical Reagent Co. and was recrystallized from methanol. Acetonitrile (Tianjin Chemical Reagents II Co.) was dried over 4 Å molecular sieves and distilled prior to utilization. All Other reagents were of analytical grade and used as received without any further purification. The fluorescent DNA probe was designed to hybridize to a 24 base portion of the *Yersinia pestis* (sequence 3). DNA oligonucleotides were purchased from Shanghai Invitrogen Biotechnique Co. Ltd., and the base sequences were listed as follows:

DNA Sequence 1: 5′-AGT AAG CAA GAG AGA GCC GGG GGG-$(CH_2)_6$-3′-SH

DNA Sequence 2: NH_2-5′-$(CH_2)_6$-GGC TCT CTC TTG CTT ACT-3′

DNA Sequence 3: 5′-CCC CCC GGC TCT CTC TTG CTT ACT-3′

2.2. Preparation of PVPy coated PDVB core/shell microspheres

The core/shell microspheres (PDVB@PVPy) were prepared by seeds distillation-precipitation polymerization. In the first stage, poly(divinylbenzene) microspheres (PDVB) were prepared by distillation-precipitation polymerization when divinylbenzene-80 (DVB) (20 ml) as monomer and 2,2-azobisisobutyronitrile (AIBN) (0.4 g) as initiator in acetonitrile (800 ml) [16], then the solid-phase carriers were obtained when PDVB microspheres were as seeds (0.5 g), 4-vinylpyridine (VPy) (0.2 ml) as monomer, DVB (0.4 ml) as crosslinker and AIBN (0.02 g) as initiator in acetonitrile (80 ml) by seeds distillation-precipitation polymerization and the reaction was ended when 40 ml of acetonitrile was distilled from the reaction system within 1.5 h. The resultant polymer microspheres were separated and purified by vacuum filtration over a G5 sintered glass filter, and washed three times with tetrahydrofuran (THF), ethanol and acetone. The particles were dried at 40°C under vacuum overnight.

2.3. Preparation of HS-DNA conjugated Au nanoparticles (Au-DNA)

–SH modified microspheres (PDVB@PVPy-SH) were prepared by the self-assembly of thioglycollic acid (TGA, 700 μl) on the PDVB@PVPy microspheres (0.4 g) in ethanol-water solution (30 ml, 5:1 v/v) at 37°C for 24 h, the resultant PDVB@PVPy-SH microspheres were separated and purified by vacuum filtration over a G5 sintered glass filter and washed three times with ethanol-water solution (5:1 v/v), and the particles were dried at 40°C under vacuum overnight. Au nanoparticles (AuNPs) prepared by the citrate reduction of $HAuCl_4$ [17] with 16 nm in diameter, as energy acceptors, was purified by ultracentrifugation. Then AuNPs (110 μl, 0.2 mmol/l) were

self-assembled onto the surface of PDVB@PVPy-SH microspheres (0.02 g) in ethanol-water solution (20 ml, 1:1 v/v) at 37°C for 24 h to get PDVB@PVPy-Au. Then, the residual pyridyl group on PDVB@PVPy-Au particles was protected by acetic acid (100 μl) was added in solution at 37°C for 5 h under shake. The PDVB@PVPy-Au particles were purified by vacuum filtration and washed with ethanol-water solution (1:1 v/v) for three times, and dried at 40°C under vacuum overnight. HS-DNA (Sequence 1, 33 μg) was mixed with purified PDVB@PVPy-Au microspheres in 10 ml of water at 37°C for 16 h. Then, the mixture solution was added into 10 ml of phosphate buffer solution (PBS, pH = 7.0), and the HS-DNA were self-assembled on the solid-phase carriers (PDVB@PVPy-Au-DNA) at 37°C for 40 h under shake. The PDVB@PVPy-Au-DNA microspheres separated and purified by ultracentrifugation (7000 r/min for 30 min) and washed with PBS (pH = 7.0) for three times. Finally, the washed PDVB@PVPy-Au-DNA microspheres were resuspended in 5 ml of water, and the Au-DNA was cut off from the carriers when pH was adjusted to 10.0 for 48 h at 50°C under shake. The carriers were removed by ultracentrifugation (7000 r/min for 30 min), and the pH of supernatant (Au-DNA aqueous solution) was adjusted to 7.0.

2.4. Preparation of NH_2-DNA conjugated CdTe QDs (QD-DNA)

3 nm of CdTe QDs in diameters as energy donors were prepared according to the reference work in aqueous solution when (3-mercaptopropionic acid) MPA was as stabilizer [15]. Before the self-assembly of QDs on microspheres, the pH of QDs aqueous solution was adjusted to 7.0 and purified by ethanol precipitation and ultracentrifugation (12 000 r/min for 60 min). After that, the CdTe QDs (17 μl, 0.25 mM aqueous solution) were self-assembled on the PDVB@PVPy microspheres (0.02 g in 20 ml of ethanol-water solution (1:1 v/v)) for 24 h at 37°C under shake because of the hydrogen-bonding between carboxyl of MPA on CdTe QDs and pyridine ring. Then, the residual pyridyl group on PDVB@PVPy-QDs particles was protected by acetic acid (100 μl) was added in solution at 37°C for 5 h under shake. The PDVB@PVPy-QDs microspheres were purified by ultracentrifugation (7000 r/min for 30 min) and washed with ethanol-water solution (1:1 v/v) for three times, and resuspended in 1 ml Tris-HCl buffer (10 mM Tris-HCl, 20 mM NaCl, pH = 7.2). Then, NH_2-DNA (sequence 2, 33 μg) with 1 ml Tris-HCl buffer (10 mM Tris-HCl, 20 mM NaCl, pH = 7.2) and 1-ethyl-3-(3-dimethylaminopropyl) carbodi-imide hydrochloride (EDC, 22 μl, 0.01 M, 50-fold mole more than NH_2-DNA) were added into the PDVB@PVPy-QDs Tris-HCl buffer solution. The NH_2-DNA was conjugated with QDs on the solid carriers (PDVB@PVPy-QD-DNA) at 37°C for 40 h under shake. Finally, the QD-DNA was cleaved from the carriers when pH was adjusted to 10.0 for 48 h at 50°C under shake. The carriers were removed by ultracentrifugation (7000 r/min for 30 min), and the pH of supernatant (QD-DNA aqueous solution) was adjusted to 7.0.

2.5. Hybridization of QD-DNA and Au-DNA and detection of target DNA

The resultant solution prepared in 2.3 and in 2.4 were mixed together and the hybridization of QD-DNA and Au-DNA (the ratio of Au/QDs was about 10:1) was when a buffer solution of 20 mM Tris-HCl, 50 mM KCl, and 5 mM $MgCl_2$ (pH = 8.0) existed in system at 37°C, for 1 h under shake. The detection program was as follows: target DNA (sequence 3, 33 μg) was added into the CdTe/AuNPs conjugated probe system at 37°C, for 1 h under shake, and the changes of fluorescent spectra of detection system were measured.

2.6. Characterization

The morphology of the resultant polymeric microspheres was determined by transmission electron microscopy (TEM) using a Tecnao G2 20 S-TWIN on a copper grid coated with a carbon membrane. Samples for TEM were dispersed in PBS buffer and a drop of the suspension was spread onto the surface of a thin carbon film supported on copper grid, then dried in vacuum.

The laser scanning confocal microscope (LSCM) images were obtained using Olympus FV1000S system. Samples of LSCM were dropped onto 35 mm glass-bottom culture dishes (Mattek Corp.) and were viewed by the LSCM microscope with 390 nm excitation and 570 nm emission.

The fluorescence spectra of the probe system were measured with a WGY-10 Luminescence Spectrometer. According to Foster's theory, The FRET efficiency (quenching efficiency) could be measured experimentally and was commonly defined according to Equation (1) [18]:

$$E = 1 - \frac{F_{DA}}{F_D} \tag{1}$$

where F_{DA} is the integrated fluorescence intensity of the donor in the presence of the acceptor(s) and F_D is the integrated fluorescence intensity of the donor alone (no acceptors present).

The loading capacity of the pyridine group on the surface of polymer microspheres was measured by back-titration [19]: 0.3 g of PDVB@PVPy microspheres were suspended in 25 ml of 0.10 mol/l HCl solution with stirring for 5 h at room temperature. Then the resultant microspheres were separated by vacuum filtration over a G5 sintered glass filter and washed with distilled water for three times. The combined filtrate was re-titrated by 0.10 mol/l NaOH aqueous solution with phenolphtalein as indicator. The loading capacity of the pyridyl group on the surface layer of the microspheres was calculated according to Equation (2):

$$n_{py} = \frac{c_{HCl} \cdot V_{HCl} - c_{NaOH} \cdot V_{NaOH}}{m} \tag{2}$$

where n_{py} [mmol/g] is the accessible loading capacity of pyridyl group, c_{HCl} is the concentration of HCl solution [mol/l], V_{HCl} is the volume of HCl solution used for suspension [ml], c_{NaOH} is the concentration of NaOH for titration [mol/l], V_{NaOH} is the volume of NaOH for titration [ml], m is the weight of the microspheres determined [g], respectively.

3. Results and discussion

3.1. PVPy coated PDVB core/shell microspheres

Stöver *et al.* reported that highly crosslinked PDVB55 microspheres can be prepared with a diameter between 2 and 5 μm by precipitation polymerization [20]. This reaction was carried out in bottles attached to a slowly rotating umbrella-shaped rotor, and the residual double bonds located at the surface permit the further growth of the particles by radical capture of oligomers and monomers [21]. An important concern for core-shell polymerization is to retain the particle monodispersity. The distillation-precipitation polymerization was convenient to prepare PDVB80 microspheres in the absence of any stabilizer without stirring [16]. Moreover, Yang and coworkers found that monodispersity core/shell microspheres could be prepared by seeds distillation-precipitation polymerization easily with hydrophilic or hydrophobic monomer [22, 23]. In this case, PDVB microspheres as cores prepared by distillation-precipitation polymerization had a large particle size (>1 μm) which could be purified easily, and the residual double bonds on the surface of microspheres could be reacted with other vinyl monomer on the particle surfaces for future modification.

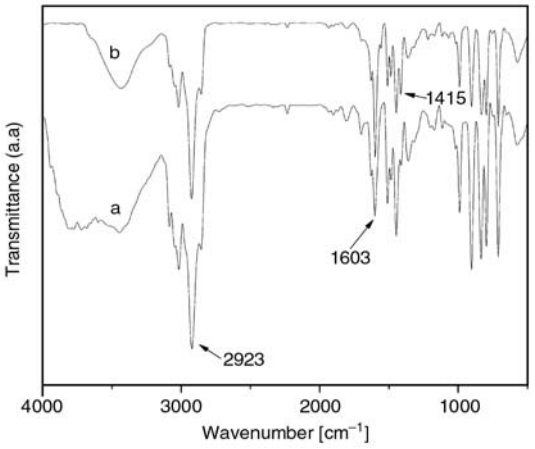

Figure 2. FT-IR spectra of polymer microspheres: a) PDVB microspheres; b) PDVB@P(VPy)

The FT-IR spectra of PDVB and poly(4-vinylpyridine) (PVPy) which had been coated PDVB core/shell microspheres (PDVB@PVPy) are shown in Figure 2. FT-IR spectra of PDVB microspheres (Figure 2 a) shows a peak at 2923 cm^{-1} attributed to the asymmetrical stretching of methylene groups while the band at 1603 cm^{-1} originated from the asymmetrical stretching of conjugated double bonds [21]. The increase of 1415 cm^{-1} absorptions was caused by the introduction of pyridine ring [24] (Figure 2b) of PDVB@PVPy microspheres, and the loading capacity of the pyridyl group on the polymer microspheres was 0.134 mmol/g.

3.2. Preparation of DNA conjugated nanoparticles by solid-phase carriers

CdTe QDs of about 3 nm diameter as energy donors were prepared in aqueous solution when

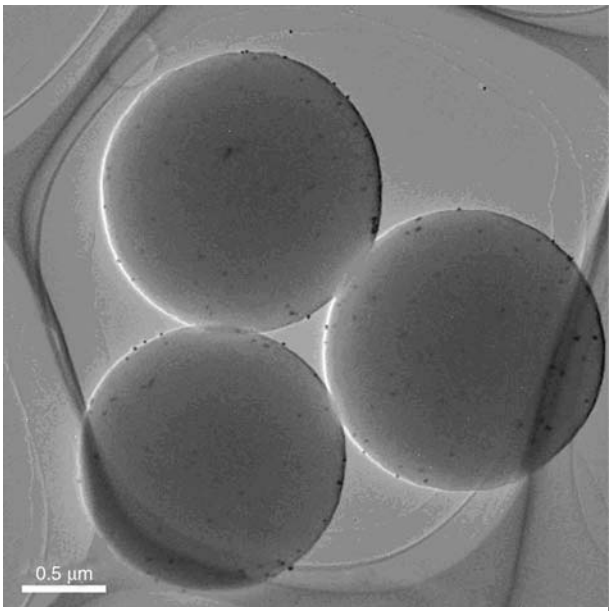

Figure 3. TEM graphs of Au-DNA on PDVB@PVPy microspheres

(3-mercaptopropionic acid) MPA was used as stabilizer [15] and because of the large particle size and functional groups of core/shell microspheres, the synthesis of mercapto group modified ssDNA (HS-DNA, sequence 1) conjugated Au nanoparticles (Au-DNA) was completed on the surface of microspheres. The TEM graphs of Au-DNA on PDVB@PVPy microspheres (PDVB@PVPy-Au-DNA) are shown in Figure 3.

AuNPs were prepared by the citrate reduction of $HAuCl_4$ [17] with 16 nm in diameter. The results indicated that the particle size of PDVB@PVPy microspheres was about 1.65 µm and the Au-DNA conjugates were self-assembled on the surface of microspheres successfully. The large size of carriers made it easily for PDVB@PVPy-Au-DNA microspheres to be separated and purified from the reaction system. Li *et al.* [19] prepared poly(ethyleneglycol dimethacrylate-*co*-4-vinylpyridine) (P(EGDMA-*co*-VPy)) microspheres by distillation-precipitation copolymerization, and only when the fraction of VPy was higher that 40% (v/v) in total monomer, the particle size of P(EGDMA-*co*-VPy) could be over 1 µm (1.72 µm) and the loading capacity of pyridyl group on microspheres was about 1.76 mmol/g. However, in this work, the loading capacity of pyridyl group on carriers should be controlled at a very low level because the amount of AuNPs and ssDNA were both trace amounts to avoid the interaction between excessive

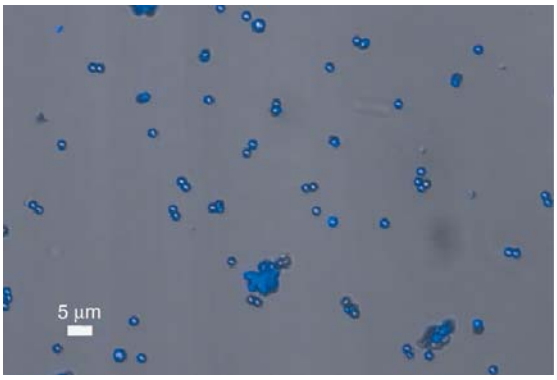

Figure 4. LSCM graphs of PDVB@PVPy-QD-DNA

pyridyl group on carriers and HS-DNA. Therefore, the structure of suitable carriers was PDVB/PVPy core/shell microspheres, when PDVB core provided a large size in diameters and PVPy shell had a low loading capacity of pyridyl group (about 0.134 mmol/g).

The laser scanning confocal microscope (LSCM) graphs of NH_2-DNA (sequence 2, complementary with sequence 1) conjugated CdTe QDs (QD-DNA) on PDVB@PVPy microspheres (PDVB@PVPy-QD-DNA) are shown in Figure 4, which indicated that the ssDNA conjugated QDs (QD-DNA) were self-assembled on the surface of microspheres.

In traditional way, the amount of nanoparticles (QDs or AuNPs) is in excess of DNA [11, 15] to reduce the influence of residual unreacted ssDNA, but which resulted in the residue of nanoparticles, especially when the particle size was too small, for example QDs was only about 2–3 nm in size [15]. The residual free QDs would increase the background fluorescence of probe based on inorganic nanoparticles, and the residual unreacted ssDNA would hybridize with the complementary ssDNA in the system.

In this work, the amount of QDs and ssDNA were nearly equal, and only simple filtration could remove the free ssDNA and nanoparticles because of the huge difference of particle sizes between solid-phase carriers and ssDNA rather than the slight difference of particle size or solubility between residual free nanoparticles and ssDNA conjugated nanoparticles in traditional ways [11–13, 15]. When the pH was about 10, the Au-DNA and QD-DNA were cut off from the carriers. After hybridization of Au-DNA and QD-DNA in a buffer solution (pH = 8), the double-stranded (dsDNA) fluorescent DNA probe was obtained.

3.3. Detection of DNA probe

According to the FRET process, when the distance between the donor and acceptor was 1–10 nm and the emission spectrum of the donors could overlap the absorption spectrum of the acceptors, the energy could be transferred from the energy donors to acceptors [1, 25]. CdTe QDs and AuNPs are a suitable donor-acceptor pair [13] because the emission spectrum of CdTe QDs and the absorption spectrum of AuNPs have a large overlap [15]. After hybridization between CdTe-DNA and Au-DNA, the CdTe and Au nanoparticles were close, therefore the fluorescence intensity of donors would decrease because of the energy transfer from the donors to acceptors and the formation of fluorescence probes with inorganic nanoparticles conjugated double-stranded DNA (QD-dsDNA-Au probe) [14, 15]. The fluorescence emission spectra of the QD-DNA, QD-dsDNA-Au probe, and QD-dsDNA-Au probe with single-stranded target DNA (sequence 3, completely complementary with sequence 1) are shown in Figure 5.

Compared with the fluorescence intensity of QD-DNA, the fluorescence intensity of QD-dsDNA-Au probe decreased tremendously, which indicated that the FRET process occurred in the QD-dsDNA-Au conjugated system after the hybridization program, and the quenching efficiency was about 73.7%. In our previous work, the quenching efficiency was 55–67% obtained when the QDs reacted with ssDNA with no purification [15]. In most cases, the background fluorescence of DNA probes with inorganic nanoparticles conjugated double-stranded DNA (QD-dsDNA-Au probe) was a common phenomenon [15, 26–27], because of the residual QDs and ratio of energy acceptors/donors, which resulted in a limit of FRET efficiency (quenching efficiency). Zhang *et al.* increased the number of energy acceptors (Cy5) which surrounded energy donors (QDs) to get a low level of background fluorescence [28]. AuNPs-DNA could be separated from reaction system by ultracentrifugation because of its larger particle size (>10 nm). However, the particle size of QDs was too small (2–3 nm) which caused the residue of unreacted QDs and ssDNA in the QD-DNA solution. The free QDs increased the background fluorescence, and when these free ssDNA (sequence 2) hybridized with ssDNA (sequence 1) on AuNPs, no FRET process could occur in that structure, which would decrease the quenching efficiency. Therefore when there was no purification process in preparation of QD-DNA, the quenching efficiency was lower (55–67%) by changing the ratio of acceptors/donors (Au-DNA/QD-DNA), and quenching efficiency reached the maximum (about 67%) when the Au-DNA/QD-DNA was 10:1 [15]. In this work, the separation and purification were easier because of the large size of solid carriers (about 1.6 μm in diameters), and the quenching efficiency was increased to 73.7% when the Au-DNA/QD-DNA was 10:1. But the background fluorescence phenomenon still existed, which indicated that the future work would be focused on the control of ratio of AuNPs/QDs.

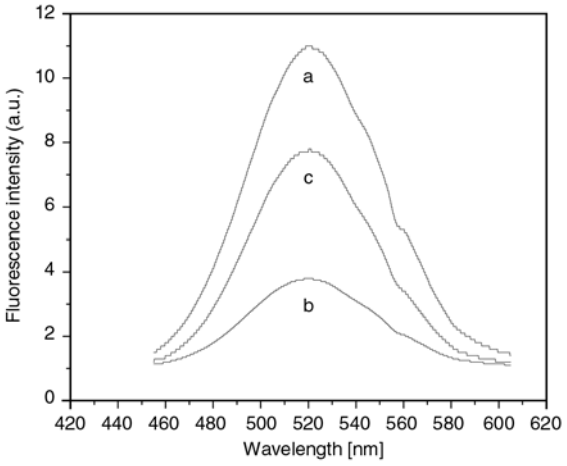

Figure 5. Fluorescence spectra of QD-DNA (a), QD-dsDNA-Au probe (b) and QD-dsDNA-Au probe with target DNA (c)

After target single-stranded DNA (sequence 3, complementary with sequence 1) was introduced into the probe system, the double-stranded DNA of the probe system opened and the distance between the CdTe QDs and Au nanoparticles increased. The target DNA could replace the DNA (sequence 2) on the QDs surface and hybridize with the DNA (sequence 1) on Au nanoparticles, because the target DNA had more complementary bases than the sequence 2 DNA, which resulted in a stronger hydrogen-bonding between the target DNA and the sequence 1 DNA, thus the fluorescent intensity of the system was recovered about 2.4 times than that of probe.

4. Conclusions

Fluorescent DNA probe which can be used as DNA biosensor was prepared by solid-phase organic synthesis on polymer functional core/shell microspheres in large diameters. PDVB microspheres as cores provided the large particles size in diameters and PVPy shell was coated on the PDVB cores were obtained by seeds distillation-precipitation polymerization. The preparation of Au-DNA and QD-DNA were on the PVPy functional shell respectively. After the hybridization program, the FRET occurred because the donors and acceptors were close enough and the quenching efficiency was about 73.7%. When complete complementary target DNA was added into this probe system, the fluorescence intensity of this system was recovered about 2.4 times than that of probe.

Acknowledgements

This work was supported by the National Natural Science Foundation of China (No. 20802051), Science and Technology Development Foundation of Tianjin Universities (No. 20070608) and Natural Science Foundation of Tianjin (No. 07JCYBJC15900).

References

[1] Wu P., Brand L.: Resonance energy transfer: Methods and applications. Analytical biochemistry, **218**, 1–13 (1994).
DOI: 10.1006/abio.1994.1134

[2] Willard D. M., Carillo L. L., Jung J., Orden A. V.: CdSe-ZnS quantum dots as resonance energy transfer donors in a model protein-protein binding assay. Nano Letters, **1**, 469–474 (2001).
DOI: 10.1021/nl015565n

[3] Dahan M., Laurence T., Pinaud F., Chemla D. S., Alivisatos A. P., Sauer M., Weiss S.: Time-gated biological imaging by use of colloidal quantum dots. Optics Letters, **26**, 825–827 (2001).
DOI: 10.1364/OL.26.000825

[4] Alivisatos A. P.: Semiconductor clusters, nanocrystals, and quantum dots. Science, **271**, 933–937 (1996).
DOI: 10.1126/science.271.5251.933

[5] Chan W. C. W., Nie S.: Quantum dot bioconjugates for ultrasensitive nonisotopic detection. Science, **281**, 2016–2018 (1998).
DOI: 10.1126/science.281.5385.2016

[6] Jaiswal J. K., Mattoussi H., Mauro J. M., Simon S. M.: Long-term multiple color imaging of live cells using quantum dot bioconjugates. Nature Biotechnology, **21**, 47–51 (2003).
DOI: 10.1038/nbt767

[7] Wu X., Liu H., Liu J., Haley K. N., Treadway J. A., Larson J. P., Ge N., Peale F., Bruchez M. P.: Immunofluorescent labeling of cancer marker Her2 and other cellular targets with semiconductor quantum dots. Nature Biotechnology, **21**, 41–46 (2003).
DOI: 10.1038/nbt764

[8] Sapsford K. E., Pons T., Medintz I. L., Mattoussi H.: Biosensing with luminescent semiconductor quantum dots. Sensors, **6**, 925–953 (2006).
DOI: 10.3390/s6080925

[9] Fu A. H., Micheel C. M., Cha J., Chang H., Yang H., Alivisatos A. P.: Discrete nanostructures of quantum dots/Au with DNA. Journal of the American Chemical Society, **126**, 10832–10833 (2004).
DOI: 10.1021/ja046747x

[10] Oh E., M. Hong M-Y., Lee D., Nam S-H., Yoon H. C., Kim H-S.: Inhibition assay of biomolecules based on fluorescence resonance energy transfer (FRET) between quantum dots and gold nanoparticles. Journal of the American Chemical Society, **127**, 3270–3271 (2005).
DOI: 10.1021/ja0433323

[11] Gueroui Z., Libchaber A.: Single-molecule measurements of gold-quenched quantum dots. Physical Review Letters, **93**, 166108/1–166108/4 (2004).
DOI: 10.1103/PhysRevLett.93.166108

[12] Kim J. H., Morikis D., Ozkan M.: Adaptation of inorganic quantum dots for stable molecular beacons. Sensors and Actuators B: Chemical, **102**, 315–319 (2004).
DOI: 10.1016/j.snb.2004.04.107

[13] Cady N. C., Strickland A. D., Batt C. A.: Optimized linkage and quenching strategies for quantum dot molecular beacons. Molecular and Cellular Probes, **21**, 116–124 (2007).
DOI: 10.1016/j.mcp.2006.09.001

[14] Dyadyusha L., Yin H., Jaiswal S., Brown T., Baumberg J. J., Booy F. P., Melvin T.: Quenching of CdSe quantum dot emission, a new approach for biosensing. Chemical Communications, **25**, 3201–3203 (2005).
DOI: 10.1039/b500664c

[15] Dai Z., Zhang J. M., Dong Q. X., Guo N., Xu S. C., Sun B., Bu Y. H.: Adaption of Au nanoparticles and CdTe quantum dots in DNA detection. Chinese Journal of Chemical Engineering, **15**, 791–794 (2007).
DOI: 10.1016/S1004-9541(08)60004-X

[16] Bai F., Yang X. L., Huang W. Q.: Synthesis of narrow or monodisperse poly(divinylbenzene) microspheres by distillation-precipitation polymerization. Macromolecules, **37**, 9746–9752 (2004).
DOI: 10.1021/ma048566l

[17] Fren G.: Preparation of gold dispersions of varying particle size: Controlled nucleation for the regulation of the particle size in monodisperse gold suspensions. Nature: Physical Science, **241**, 20–22 (1973).

[18] Pons T., Medintz I. L., Sapsford K. E., Higashiya S., Grimes A. F., English D. S., Mattoussi H.: On the quenching of semiconductor quantum dot photoluminescence by proximal gold nanoparticles. Nano Letters, **7**, 3157–3164 (2007).
DOI: 10.1021/nl071729+

[19] Li S-N., Yang X-L., Huang W-Q.: Preparation of polymer microspheres with pyridyl group and their stabilized gold metallic colloids. Chinese Journal of Polymer Science, **25**, 555–563 (2007).
DOI: 10.1142/S0256767907002461

[20] Li W-H., Stöver H. D. H.: Porous monodisperse poly(divinylbenzene) microspheres by precipitation polymerization. Journal of Polymer Science Part A: Polymer Chemistry, **36**, 1543–1551 (1998).
DOI: 10.1002/(SICI)1099-0518(19980730)36:10<1543::AID-POLA7>3.0.CO;2-R

[21] Downey J. S., Frank R. S., Li W-H., Stöver H. D. H.: Growth mechanism of poly (divinylbenzene) microspheres in precipitation polymerization. Macromolecules, **32**, 2838–2844 (1999).
DOI: 10.1021/ma9812027

[22] Bai F., Yang X., Zhao Y., Huang W.: Synthesis of core-shell microspheres with active hydroxyl groups by two-stage precipitation polymerization. Polymer International, **54**, 168–174 (2005).
DOI: 10.1002/pi.1670

[23] Qi D., Bai F., Yang X., Huang W.: Synthesis of core-shell polymer microspheres by two-stage distillation-precipitation polymerization. European Polymer Journal, **41**, 2320–2328 (2005).
DOI: 10.1016/j.eurpolymj.2005.04.034

[24] Luyten M. C., Alberda van Ekenstein G. O. R., Wildeman J., ten Brinke G., Ruokolainen J., Ikkala O., Torkkeli M., Serimaa R.: Ordering in supramolecular elastomer-amphiphile systems. 4. Vinylpyridine-divinylbenzene networks with alkylphenols. Macromolecules, **31**, 9160–9165 (1998).
DOI: 10.1021/ma9808833

[25] Clapp A. R., Medintz I. L., Mauro J. M., Fisher B. R., Bawendi M. G., Mattoussi H.: Fluorescence resonance energy transfer between quantum dot donors and dye-labeled protein acceptors. Journal of the American Chemical Society, **126**, 301–310 (2004).
DOI: 10.1021/ja037088b

[26] Wang T-H., Peng Y-H., Zhang C., Wong P. K., Ho C-M.: Single-molecule tracing on a fluidic microchip for quantitative detection of low-abundance nucleic acids. Journal of the American Chemical Society, **127**, 5354–5359 (2005).
DOI: 10.1021/ja042642i

[27] Zhang C. Y., Chao S. Y., Wang T. H.: Comparative quantification of nucleic acids using single-molecule detection and molecular beacons. Analyst, **130**, 483–488 (2005).
DOI: 10.1039/b415758c

[28] Zhang C-Y., Yeh H-C., Kuroki M-T., Wang T-H.: Single-quantum-dot-based DNA nanosensor. Nature Materials, **4**, 826–831 (2005).
DOI: 10.1038/nmat1508

eXPRESS Polymer Letters Vol.3, No.8 (2009) 492–500
Available online at www.expresspolymlett.com
DOI: 10.3144/expresspolymlett.2009.61

Radiation processed ethylene vinyl acetate-multiple walled carbon nanotube nano-composites: Effect of MWNT addition on the gel content and crosslinking density

K. A. Dubey, Y. K. Bhardwaj, C. V. Chaudhari, Virendra Kumar, N. K. Goel, S. Sabharwal*

Radiation Technology Development Section Bhabha Atomic Research Centre, Trombay Mumbai-400 085, India

Received 2 March 2009; accepted in revised form 24 May 2009

Abstract. Different compositions of ethylene vinyl acetate (EVA)/multiple walled carbon nanotube (MWNT) nano-composites were prepared by melt mixing and subjected to different doses of gamma radiation. The efficiency of radiation vulcanization was analyzed by sol-gel analysis, Charlesby-Pinner parameter estimation and crosslinking density measurements. Gamma radiation induced crosslinking was found to increase with MWNT fraction in EVA-MWNT nano-composites (p_0/q_0 in the range: 1.15–0.98). These results ruled out the possibility of a significant neutralization of single ionization spurs by MWNT addition. The incorporation of MWNT also resulted in increased hardness and higher density of the nano-composite matrix. The efficiency of multifunctional acrylates as crosslinking aid in the radiation-induced vulcanization of EVA-MWNT nano-composites was also investigated. The results established lower efficiency of methacrylates than of acrylates in the radiation vulcanization process.

Keywords: *nanocomposites, gamma-radiation, EVA, MWNT, crosslinking*

1. Introduction

Elastomeric materials are usually reinforced by carbon black, silica and other microscopic fillers for improving/enhancing/achieving the desired properties [1–3]. Composites filled with nanofillers such as metallic nanoparticles and carbon nanotubes have been envisaged to have superior physical and mechanical properties compared to the conventional fiber or particle reinforced composites [4, 5]. Multiwalled nanocarbon tubes (MWNTs) have been widely used with different kinds of polymers for the development of high performance composite materials [6, 7], however MWCNT/rubber nano-composites is still a evolving field and very little work has been documented on the subject.

Ethylene vinyl acetate (EVA) is widely used as an insulating and sheath material for high voltage cables and also in the footwear and toy industries due to its high flexibility and chemical inertness [8, 9]. High-energy ionizing radiation has recently received a great deal of attention, primarily because of its ability to produce crosslinked networks with a wide range of polymers. The low operation cost, additive-free technique and room temperature operations are among the added advantages of radiation vulcanization over the existing vulcanizing techniques [10–14]. The modification and processing of particulate filled EVA using high energy radiation has been widely practiced, however not significant work has been reported on radiation induced effects on EVA reinforced with nanomaterials [15–17]. The nano-composites of EVA with MWNT are of special interest because incorporation of suitable amount of MWNT in EVA matrix is expected to

*Corresponding author, e-mail: ykbhard@barc.gov.in

significantly enhance its thermal and mechanical properties. However, high absorbed dose requirement for desired extent of crosslinking leads to cost enhancement as well as deterioration of mechanical properties of EVA at higher doses. Use of multifunctional acrylates (MFAs) and allylic reactive molecules during radiation processing have been proposed to overcome these drawbacks of radiation processing [18–21].

Radiation crosslinking i.e. gelation characteristic of filler reinforced polymer has been a subject of debate for various workers in the field [22, 23]. The objective of the present work was to analyze the effect of MWNT addition on the radiation induced crosslinking behavior of EVA-MWNT nano-composites. In addition to it, an attempt has also been made to look for suitable multifunctional acrylates for efficient radiation cross-linking of these nano-composite blends.

2. Materials and methods

2.1. Materials

EVA in granular form was supplied by a local supplier (M/s Polystar Chemicals, Mumbai), MWNT powder from M/s Nanocyl, Belgium was used without further purification. Toluene and xylene used for studies were of AnalaR grade (Purity 99.9%). The multifunctional acrylates were procured from Aldrich chemicals, USA and used as such without further purification.

2.2. Sample preparation and characterization

A series of nano-composites of EVA and MWNT was prepared by initially mixing the two components homogeneously on a Brabender Plasticorder from M/s Brabender, Germany at 130°C for 15 min. The nano-composites compositions and sample designations have been represented in Table 1. The homogeneous mix was cut to small pieces and compressed into sheets of size 12× 12 cm of different thicknesses in range 1–4 mm using compression-molding machine at 1500 N/m^2 pressure for 2 minutes at 130°C.

Irradiation was carried out under aerated condition in a gamma chamber 5000 (GC-5000) having Co-60 gamma source supplied by M/s BRIT India. The dose rate of gamma chamber was ascertained to be 3.5 kGy/hr by using Fricke dosimetry prior to irradiation of samples.

For the sorption studies, radiation crosslinked blends were Soxhlet extracted at elevated temperature for 12 hours to extract any sol content using xylene as solvent. The insoluble gel part was then dried initially under room conditions and later in a dissector. The dried blend so obtained was cut into uniform square pieces (1 cm×1 cm) using a sharp edged die and used for swelling studies. Pre-weighed samples were placed in a 200-mesh stainless steel compartment and immersed in excess xylene. The swelled samples were periodically removed, blotted free of surface xylene using laboratory tissue paper, weighed on AND analytical balance (accuracy 0.00001 g) in stopper bottles and returned to the swelling medium. Measurements were taken until the samples reached constant weight.

Hardness was measured in accordance with ASTM D2240 using durometer (M/s Asha-testers, Blue-steel Eng. (P) Ltd, India). The units of hardness were expressed in shore A. The density (in g·cm^{-3}) was determined by using density balance from M/s AND (accuracy 0.00001 g) using suitable liquids.

The gel content was determined by refluxing the samples with xylene for 12 hrs. The insoluble portion obtained was rinsed with methanol and dried in vacuum oven at 60°C to a constant weight. Gel content was evaluated using following relationship (Equation 1):

$$Gel\ content = \left(\frac{W_g}{W_i}\right) \tag{1}$$

where W_g and W_i are the weight of insoluble fraction and initial weight respectively.

3. Results and discussion

3.1. Scanning electron microscopy

The scanning electron micrographs of fractured surfaces have been shown in Figure 1. It is clear that for all compositions EVA-MWNT were well mixed as no agglomeration of nanotubes was observed in the composition range studied.

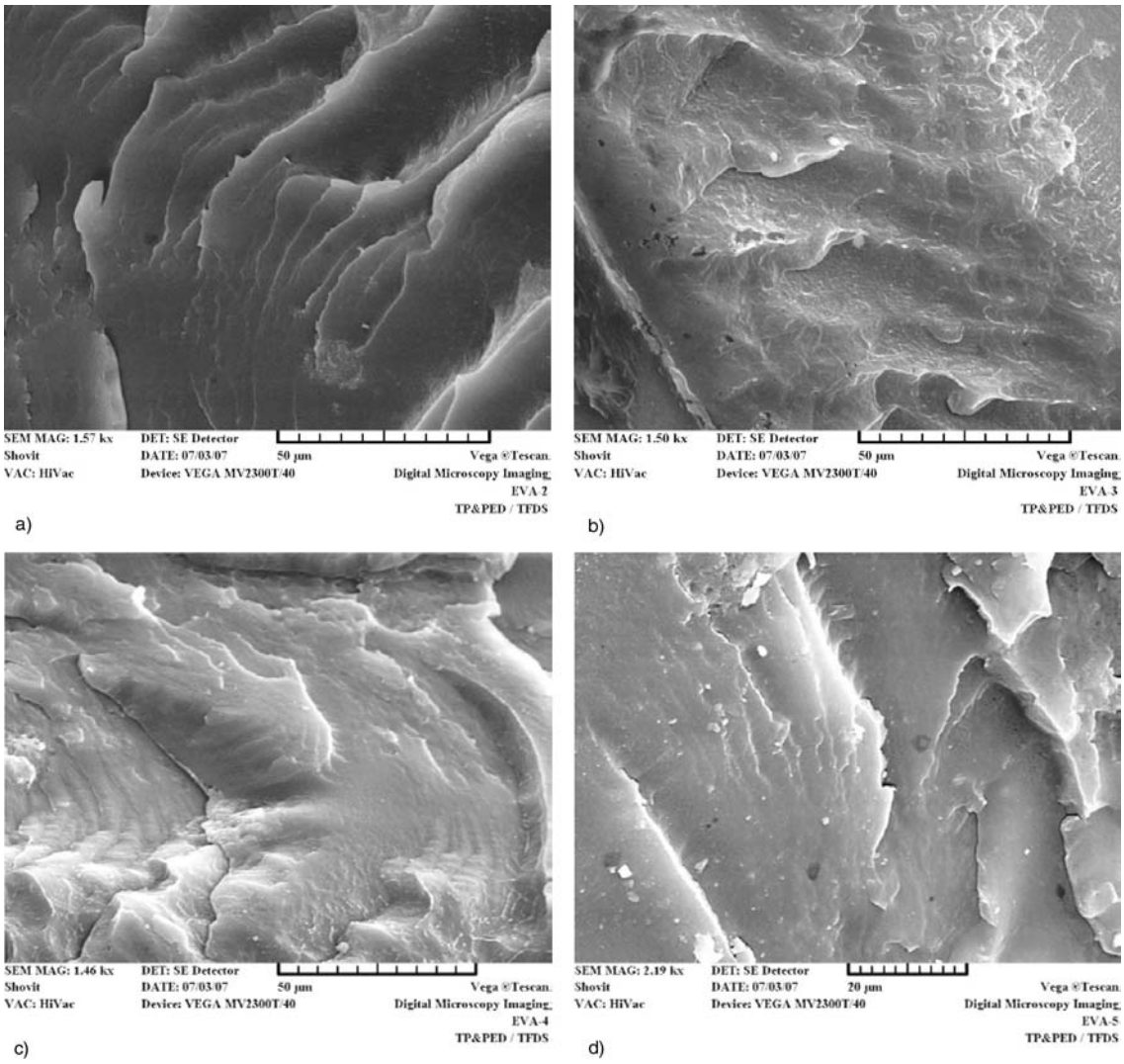

Figure 1. Scanning electron micrographs of EVA-MWNT nano-composites a) 2% MWNT, b) 3% WNT, c) 4% MWNT, d) 5% MWNT

3.2. Effect of gamma radiation on nano-composites

Figure 2 shows the change in the gel content of EVA-MWNTs nano-composites on irradiation. Un-irradiated samples were easily soluble in hot xylene, however nano-composites irradiated to a dose > 50 kGy were partly soluble due to the formation of a three-dimensional network.

In order to quantitatively evaluate crosslinking and chain scission yields of irradiated EVA-MWNT nano-composites, plots of $S + S^{1/2}$ vs. 1/absorbed dose from the Charlesby-Pinner equation (Equation 2) for the different blend compositions were drawn (Figure 3) [24–25]:

$$S + \sqrt{S} = \frac{p_0}{q_0} + \frac{1}{\alpha P_n D} \tag{2}$$

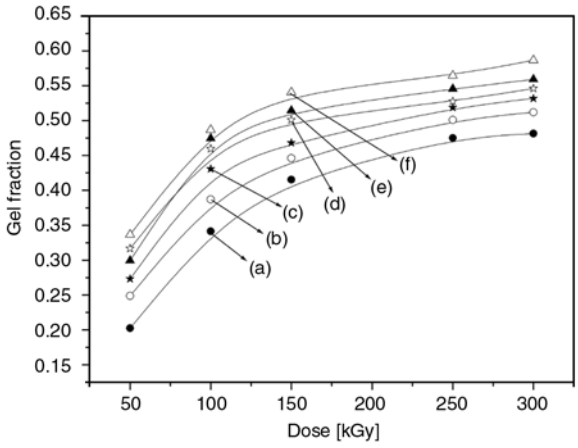

Figure 2. Gel fraction of EVA-MWNT nano-composites on irradiation at a dose rate of 5 kGy·h^{-1}
a) EV_{NT00}, b) EV_{NT05}, c) EV_{NT1}, d) EV_{NT2}, e) EV_{NT3}, f) EV_{NT5}

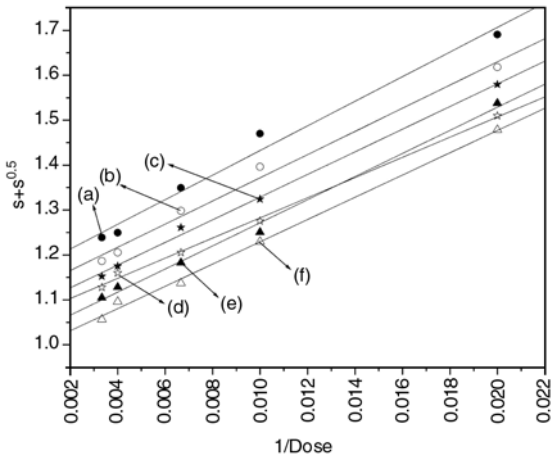

Figure 3. Charlesby-Pinner plot for EVA-MWNT nano-composites a) EV_{NT00}, b) EV_{NT05}, c) EV_{NT1}, d) EVNT2, e) EV_{NT3}, f) EV_{NT5}

Table 1. Compositional characteristics, designation and p_0/q_0 for nano-composite blends

MWNT [%]	Sample designation	p_0/q_0
00	EV_{NT00}	1.16
0.5	EV_{NT05}	1.11
1.0	EV_{NT1}	1.08
2.0	EV_{NT2}	1.06
3.0	EV_{NT3}	1.01
5.0	EV_{NT5}	0.98

where S is the sol fraction, P_n the number averaged degree of polymerization, D radiation dose, p_0 and q_0 are fraction of ruptured and crosslinked main-chain units per unit dose (proportional to the radiation chemical yields of degradation and crosslinking).

From Table 1 and Figure 3 it is clear that EV_{NT5} is most efficiently crosslinked on irradiation and the crosslinking extent increases almost linearly with MWNT content in the nano-composite. Lower values of p_0/q_0 for higher MWNT content are suggestive of relatively improved radical-radical interactions in polymer nano-composites probably due to decrease in free-volume as reported by other workers for similar systems [22, 23, 26].

3.3. Crosslinking density of radiation processed nano-composites

In order to gain further insight into radiation crosslinking of the EVA-MWNT nano-composites, crosslinking density measurements were carried out. The key parameters determining the amount of solvent absorbed at equilibrium swelling by a crosslinked network are the crosslink density and the extent of polymer-solvent interaction which is reported as the value of Flory-Huggins parameter χ [27, 28]. The diffusion into solid samples depends on the availability of appropriate molecular size holes in the network, however the kinetic response which includes solvent sorption rate, the rate of approach to equilibrium and the transport mechanism controlling the solvent sorption may also depend upon additional factors like history of the samples and their composition [28, 29]. The molecular weight between cross-links (M_c) was estimated using the following relation, based on the theory initially proposed by Flory and Rehner (Equation 3) [30]:

$$\overline{M}_c = -V_1 \rho_p \frac{\phi_p^{1/3} - \phi_p^{1/2}}{\ln(1-\phi_p) + \phi_p + \chi\phi_p^2} \tag{3}$$

where, V1 is the molar volume of the solvent, ρ_p is the polymer density, ϕ_p is the volume fraction of the polymer in the swollen matrix and χ is the Flory–Huggins interaction parameter between solvent and polymer which can be calculated using Equation (4):

$$\chi = \beta + \frac{V_1}{RT}(\delta_s - \delta_p)^2 \tag{4}$$

where δ_s and δ_p are the solubility parameters of the solvent and the polymer, β is the lattice constant whose value is taken as 0.34, R is the universal gas constant and T is absolute temperature. The variation in crosslinking density with absorbed dose for nano-composites is plotted in Figure 4. It is clear from the figure that though at lower doses there is not much difference among the crosslink densities of different nano-composites but the difference is significant at higher absorbed doses. This observation reflects the higher radiation sensitivity of nano-composites with higher MWNT fraction. The inferences from the p_0/q_0 values, from sol-gel analysis give an idea of the predominant process (crosslinking/degradation) which the polymer undergoes in the dose range of study. The crosslinking density measurements on the other hand indicate that even if all samples predominantly undergo same process (crosslinking in this study) which among them is more prone to crosslinking at a given dose.

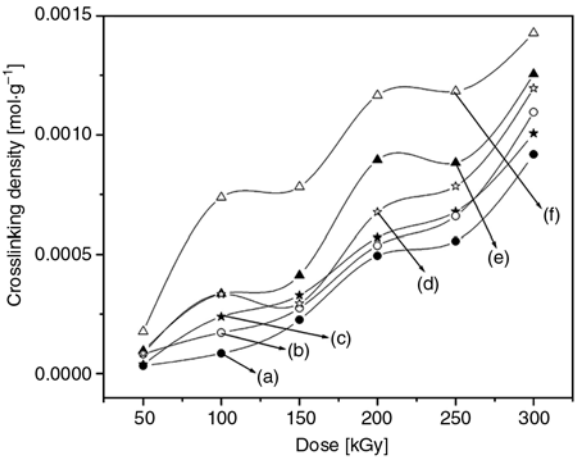

Figure 4. Crosslinking density of EVA-MWNT nano-composites on irradiation at a dose rate of 5 kGy·h^{-1} a) EV_{NT00}, b) EV_{NT05}, c) EV_{NT1}, d) EV_{NT2}, e) EV_{NT3}, f) EV_{NT5}

It is thus not improbable that the gel content attains a plateau value whereas, crosslinking density keeps increasing due to further increase in intermolecular radical-radical combinations and other rearrangements. Nevertheless, crosslinking density values followed the order EV_{NT5}>EV_{NT3}>EV_{NT2}>EV_{NT1}>EV_{NT05}>EV_{NT00}, in the complete dose range studied indicating predominantly crosslinking behavior of nano-composites on irradiation and enhancement in the crosslinking density with the incorporation of MWNT.

In general, additives are expected to induce a diminishing effect of radiation, as part of energy deposited during irradiation is expected to be absorbed by additives in addition to the bulk matrix. Furthermore, fillers may scavenge the radicals generated on the polymer matrix this may hinder the radical-radical interactions and hence reduce overall crosslinking density and gel fraction. Studies have shown that rate of radiation induced polymerization decreases in presence of inorganic fillers though the kinetics remains unchanged [22, 23, 26].

Nanoparticulate fillers like carbon nanotubes, if distributed uniformly, are expected to sit in the available free volume of the matrix, also the concentration of MWNTs in the study is too small to directly contribute to significant absorption of energy. Thus, the enhancement in the crosslinking yield after the MWNT incorporation indicates the formation of multi ionization spurs yielding Y-crosslinking and also increased possibility of spur overlap due to reduced free volume. It can therefore be safely said that neutralization of single ionization spurs, with increase in MWNT, is not significant in the present system as reported earlier [31, 32].

3.4. Density of the nano-composites

The density of nano-composites is expected to change after irradiation because of the change in free-volume associated with radiation induced crosslinking or degradation. Densities of the EVA-MWNT nano-composite were found to increase marginally with the radiations dose and with MWNT fraction except that with highest content of MWNT as shown in Figure 5. This behavior can be explained on the basis of free volume theory; the increase in crosslinking with increase in absorbed dose for the samples with higher content of MWNT decreases the free volume due to strong interfacial interaction between EVA and nanotube surfaces, and thus increases the density, on the other hand, irradiation of EVA with lower MWNT content leads to increase in density but not to that extent as it still has free volume due to lower concentration of MWNT [33]. The samples did not show any significant increase in density after certain absorbed doses clearly, indicating that increase in crosslink density of samples does not contribute to decrease in free volume after certain extent of crosslinking.

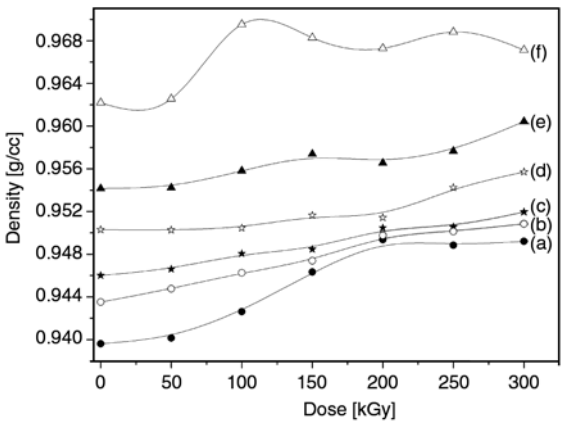

Figure 5. Density of EVA-MWNT nano-composites on irradiation at a dose rate of 5 kGy·h^{-1} a) EV_{NT00}, b) EV_{NT05}, c) EV_{NT1}, d) EV_{NT2}, e) EV_{NT3}, f) EV_{NT5}

3.5. Hardness

Figure 6 shows the compositional dependence of hardness of the samples with increase in radiation dose. It was found that initially the hardness of the

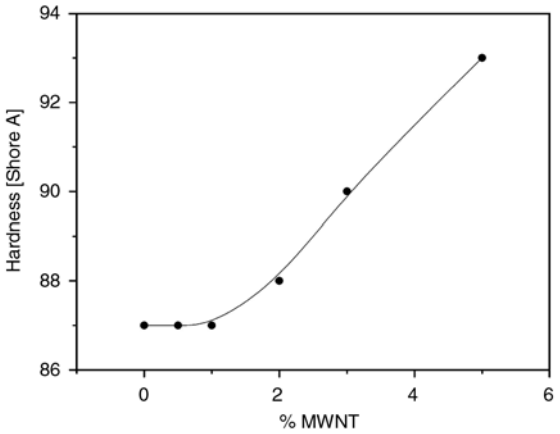

Figure 6. Variation of shore A hardness of EVA-MWNT nano-composites

EVA-MWNT nano-composites increases sharply for >1% MWNT loading. By definition, hardness is generally referred to the resistance of material to the local deformation, and the results proved that the EVA-MWNT nano-composites, with higher nanotube content, are more resistant towards local deformations. Though radiation-induced crosslinking in polymeric systems is expected to increase the hardness of the samples linearly on irradiation, the hardness values of irradiated EVA-MWNT nano-composites did show this trend only after a threshold amount of MWNT was incorporated in the nano-composites indicating MWNT content and not the absorbed dose was predominant reason for increase in hardness for these nanocomposites.

3.6. Radiation sensitivity of EVA-MWNT nano-composites in presence of MFAs

The studies in earlier sections indicated that gel content of the nano-composites varied in the range 0.25–0.55 depending on the radiation dose. Multi-functional acrylates (MFAs) are generally used for lowering the absorbed dose requirement [18–20]. The Table 2 provides the details of acrylates used for the study and Figure 7 and 8 depicts the variation in gel content on incorporation of two TMPTA and TMPTMA in EVA-MWNT composites.

It is evident from the figures that the nano-composites are more efficiently crosslinked after incorporation of MFAs. The improvement in the radiation sensitivity of the nano-composite after MFA addition was further established by crosslinking density measurements of nano-composites crosslinked using MFAs as shown in Figure 9 and 10.

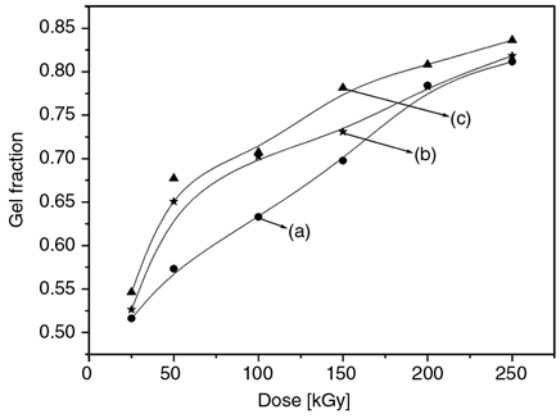

Figure 7. Gel fractions of EVA-MWNT nano-composites containing TMPTA (3%) on irradiation at a dose rate of 5 kGy·h^{-1} a) $EV_{NT00}{}^{TM}$, b) $EV_{NT1}{}^{TM}$, c) $EV_{NT3}{}^{TM}$

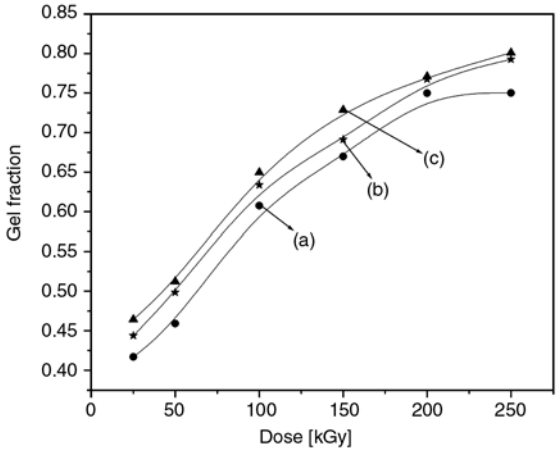

Figure 8. Gel fraction of EVA-MWNT nano-composites containing TMPTMA (3%), on irradiation at a dose rate of 5 kGy·h^{-1} (a $EV_{NT00}{}^{TMM}$, b) $EV_{NT1}{}^{TMM}$, c) $EV_{NT3}{}^{TMM}$

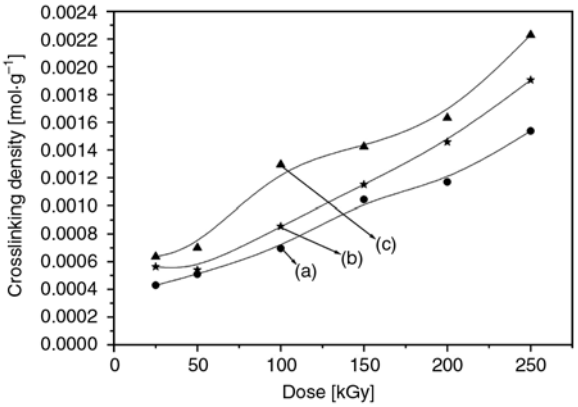

Figure 9. Crosslinking density of EVA-MWNT nano-composites containing TMPTA (3%), on irradiation at a dose rate of 5 kGy·h^{-1} a) $EV_{NT00}{}^{TM}$, b) $EV_{NT1}{}^{TM}$, c) $EV_{NT3}{}^{TM}$

Increase in the gel content on introduction of MFAs in the pure nano-composites was obviously due to

Table 2. Properties of multifunctional acrylates used in the study

Multi functional acrylate (MFA)	Structure	Functionality	M.W.	Designation
Blank	–	Nil	–	EV
Trimethylolpropane triacrylate (TMPTA)	$(H_2C=CHCO_2CH_2)_3CC_2H_5$	3	296.32	EV^{TM}
Trimethylolpropane trimethacrylate (TMPTMA)	$[H_2C=C(CH_3)CO_2CH_2]_3CC_2H_5$	3	338.40	EV^{TMM}

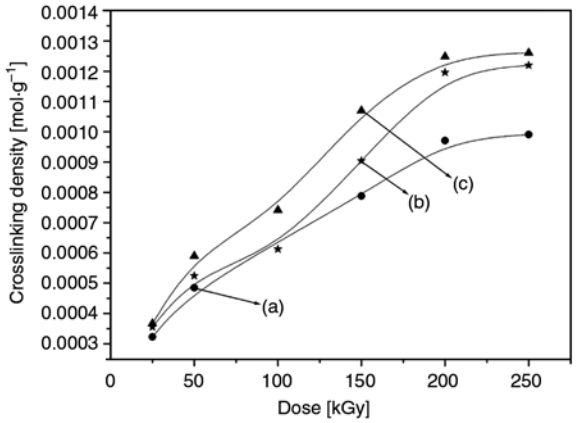

Figure 10. Crosslinking density of EVA-MWNT nano-composites containing TMPTMA (3%), on irradiation at a dose rate of 5 kGy·h^{-1}
a) EV_{NT00}^{TMM}, b) EV_{NT1}^{TMM}, c) EV_{NT3}^{TMM}

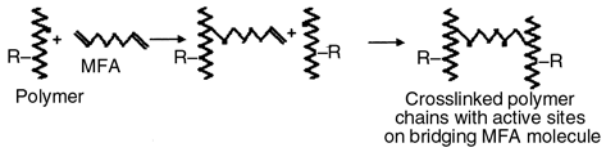

Figure 11. Scheme of the effect of multifunctional acrylates (MFA) on the corsslinking process

multifunctional acrylates employed in this study, as they are known to efficiently form bridges between the radicals generated on two different polymer chains causing inter molecular crosslinking thereby contributing to increased gel fraction as shown in Figure 11 [10–13].

In accordance with Figure 11 the crosslinking efficiency of a MFA is expected to be a function of its extent of unsaturation (functionality) and its compatibility with the polymer matrix. Since, the acrylates employed in the study were of same functionality, it was interesting to observe that radiation sensitivity of acrylate was much higher than methacrylate. This may due to better compatibility of acrylate in comparison to methacrylate with that of matrix being crosslinked using these MFAs. The compatibility of MFA with a polymer blend can be adequately judged by its swelling behavior in that MFA. The MFA uptake per 100 g of rubber blend has been represented in Figure 12, higher swelling

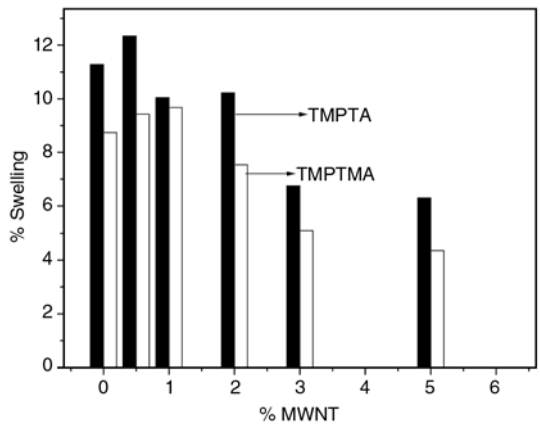

Figure 12. Multifunctional acrylate uptake by EVA-MWNT nano-composites

indicating similarity in cohesive energy densities of the two and better interaction between TMPTA molecules and nano-composite.

However, penetration of MFA molecules was found to decrease with increase in MWNT loading. Furthermore, the higher efficiency of the TMPTA over TMPTMA, in addition to above mentioned better interaction of TMPTA with nano-composite matrix, can be explained on the basis of the polymerization kinetics of acrylate and methacrylate monomers. Rate constants for propagation reported in the literature for methacrylates are almost two orders of magnitude lower than those of acrylates. A comparison between rate constant for propagation values and average termination rate constant values for some acrylates and methacrylates is given in Table 3. Due to low kp values of methacrylates as compared to the acrylates the crosslinking reaction with methacrylates (radical recombination) is expected to be less efficient.

4. Conclusions

Gel fraction, crosslinking density measurements and Charleby-Pinner parameter for the different compositions of EVA-MWNT nano-composites indicated higher radiation sensitivity of the nano-composite matrix with higher MWNT concentration. This was attributed to the enhanced probabil-

Table 3. Literature value for the rate parameters

Monomer	k_p [mol^{-1}·dm^3·s^{-1}]	Solvent	T [°C]	Reference	$<2k_t>$ [mol^{-1}·dm^3·s^{-1}]	Solvent	T [°C]	Reference
BA	1800	Bulk	30	[31]Van Herk (2000)	$(1.2–6)\cdot10^8$	Bulk	30	[33]Beuerman et al. 1996
BMA	370	Bulk	25	[31]Van Herk (2000)	$(0.1–3)\cdot10^8$	CH	22	[34]Takacs et al. 2002
MA	13300	Bulk	25	[31]Van Herk (2000)	$(0.5–18)\cdot10^8$	CH	22	[34]Takacs et al. 2002
MMA	323	Bulk	25	[31]Van Herk (2000)	$6\cdot10^7$	Bulk	22	[33]Beuerman et al. 1996
CHA	2722	Benzene	30	[32]Brandrup et al. (1999)	$(0.1–4)\cdot10^8$	CH	22	[34]Takacs et al. 2002
CHMA	601	Bulk	25	[31]Van Herk (2000)	$(4.30–7.1)\cdot10^8$	CH	22	[34]Takacs et al. 2002

k_p-rate constant for propagation, $<2k_t>$-average termination rate constant; BA-Butyl acrylate; BMA-Butyl methacrylate; MA-Methylacrylate; MMA-Methyl methacrylate; CHA-Cyclohexyl acrylate; CHMA-cyclohexyl methacrylate; CH-Cyclo hexane

ity of spur overlap, due to the reduction in the free volume of the nano-composite matrix with higher MWNT content. The incorporation of MWNT also results in the increased hardness and higher density of the nano-composite matrix. A significant reduction in the dose requirement was achieved with incorporation of multifunctional acrylates and the results established lower efficiency of trimethylolpropane trimethacrylate than trimethylolpropane triacrylate in radiation induced crosslinking process.

References

[1] Beaucage G., Rane S., Schaefer D. W., Lonf G., Fisher D.: Morphology of polyethylene-carbon black composites. Journal of Polymer Science Part B: Polymer Physics, **37**, 1105–1119 (1999).
DOI: 10.1002/(SICI)1099-0488(19990601)37:11<1105::AID-POLB6>3.0.CO;2-5

[2] Li Z. H., Zhang J., Chen S. J.: Effects of carbon blacks with various structures on vulcanization and reinforcement of filled ethylene-propylene-diene rubber. Express Polymer Letters, **2**, 695–704 (2008).
DOI: 10.3144/expresspolymlett.2008.83

[3] Qian D., Dickey E. C., Andrews R., Rantell T.: Load transfer and deformation mechanisms in carbon nanotube-polystyrene composites. Applied Physics Letters, **76**, 2868–2870 (2000).
DOI: 10.1063/1.126500

[4] Oya A.: Polypropylene clay nanocomposites. in 'Polymer nano-composites' (eds.: Pinnavaia T. J., Beall G. W.) Wiley, London, 151–172. (2000).

[5] Giannelis E. P., Krishnamoorti R., Manias E.: Polymer-silicate nanocomposites: Model systems for confined polymers and polymer brushes. Advances in Polymer Science, **138**, 107–148 (1998).
DOI: 10.1007/3-540-69711-X_3

[6] Romhány G., Szebényi, G.: Interlaminar crack propagation in MWCNT/fiber reinforced hybrid composites. Express Polymer Letters, **3**, 145–151 (2009).
DOI: 10.3144/expresspolymlett.2009.19

[7] Ajayan P. M., Stephan O., Colliex C., Trauth D.: Aligned carbon nanotube arrays formed by cutting a polymer resin-nanotube composite. Science, **265**, 1212–1214 (1994).
DOI: 10.1126/science.265.5176.1212

[8] Schadler L. S., Giannaris S. C., Ajayan P. M.: Load transfer in carbon nanotube epoxy composites. Applied Physics Letters, **73**, 3842–3847 (1998).
DOI: 10.1063/1.122911

[9] Placek V., Bartonicek B., Hnát V., Otáhal B.: Dose rate effects in radiation degradation of polymer-based cable materials. Nuclear Instruments and Methods in Physics Research Section B: Beam Interactions with Materials and Atoms, **208**, 448–453 (2003).
DOI: 10.1016/S0168-583X(03)00626-8

[10] Aoshuang Y., Zhengtao G., Li L., Ying Z., Peng Z.: Mechanical properties of radiation vulcanized NR/BR blending system. Radiation Physics and Chemistry, **63**, 497–500 (2002).
DOI: 10.1016/S0969-806X(01)00634-X

[11] Dubey K. A., Pujari P. K., Ramnani S. P., Kadam R. M., Sabharwal S.: Microstructural studies of electron-beam irradiated celluose pulp. Radiation Physics and Chemistry, **69**, 395–400 (2004).
DOI: 10.1016/j.radphyschem.2003.07.005

[12] Dubey K. A., Bhardwaj Y. K., Chaudhari C. V., Kumar V., Goel N. K., Sabharwal S.: Radiation processed polychloroprene-co-ethylene-propene diene terpolymer blends: Effect of radiation vulcanization on solvent transport kinetics. Nuclear Instruments and Methods in Physics Research Section B: Beam Interactions with Materials and Atoms, **276**, 795–801 (2009).
DOI: 10.1016/j.nimb.2008.12.008

[13] Chaudhari C. V., Bhardwaj Y. K., Patil N. D., Dubey K. A., Kumar V., Sabharwal S.: Radiation induced vulcanization of natural rubber latex in presence of styrene-butadiene rubber latex addition. Radiation Physics and Chemistry, **72**, 613–618 (2005).
DOI: 10.1016/j.radphyschem.2004.03.012

[14] Dubey K. A., Bhardwaj Y. K., Chaudhari C. V., Sabharwal S.: Radiation processed styrene-butadiene-*co*-ethylene-propylene diene rubber blends: Compatibility and swelling studies. Journal of Applied Polymer Science, **99**, 3638–3649 (2006).
DOI: 10.1002/app.22765

[15] Zanetti M., Camino G., Thomann R., Müllhaupt R.: Synthesis and thermal behaviour of layered silicate-EVA nanocomposites. Polymer, **42**, 4501–4507 (2001).
DOI: 10.1016/S0032-3861(00)00775-8

[16] Lawandy S. N., Halim S. M., Darwish N. A.: Structure aggregation of carbon black in ethylene-propylene diene polymer. Express Polymer Letters, **3**, 152–158 (2009).
DOI: 10.3144/expresspolymlett.2009.20

[17] Zhang W., Chen D., Zhao Q., Fang Y.: Effects of different kinds of clay and different vinyl acetate content on the morphology and properties of EVA/clay nanocomposites. Polymer, **44**, 7953–7961 (2003).
DOI: 10.1016/j.polymer.2003.10.046

[18] Dubey K. A., Bhardwaj Y. K., Chaudhari C. V., Sabharwal S., Mohan H.: Structure-reactivity studies on crosslinking of tri(propylene glycol diacrylate) in aqueous solutions. Reactive and Functional Polymers, **67**, 282–293 (2007).
DOI: 10.1016/j.reactfunctpolym.2007.01.001

[19] Dubey K. A., Bhardwaj Y. K., Chaudhari C. V., Bhattacharya S., Gupta S. K., Sabharwal S.: Radiation effects on SBR-EPDM blends: A correlation with blend morphology. Journal of Polymer Science Part B: Polymer Physics, **44**, 1676–1689 (2006).
DOI: 10.1002/polb.20822

[20] Banik I., Dutta S. K., Chaki T. K., Bhowmick A. K.: Electron beam induced structural modification of a fluorocarbon elastomer in the presence of polyfunctional monomers. Polymer, **40**, 447–458 (1999).
DOI: 10.1016/S0032-3861(98)00244-4

[21] Jayasuriya M. M., Makuuchi K., Yoshi F.: Radiation vulcanization of natural rubber latex using TMPTMA and PEA. European Polymer Journal, **37**, 93–98 (2001).
DOI: 10.1016/S0014-3057(00)00091-4

[22] Chiou B-S., Raghavan S. R., Khan S. A.: Effect of colloidal fillers on the cross-linking of a UV-curable polymer: Gel point rheology and the Winter-Chambon criterion. Macromolecules, **34**, 4526–4533 (2001).
DOI: 10.1021/ma010281a

[23] Sharifa J., Yunus W. M. Z. W., Dahlan K. Z. H. M., Ahmad M. H.: Preparation and properties of radiation crosslinked natural rubber/clay nanocomposites. Polymer Testing, **24**, 211–217 (2005).
DOI: 10.1016/j.polymertesting.2004.08.008

[24] Chapiro A.: Radiation chemistry of polymeric systems. Wiley, New York (1962).

[25] Charlesby A.: Atomic radiation and polymers. Pergamon Press, Oxford (1960).

[26] Zagórski Z. P.: EB-crosslinking of elastomers, how does it compare withb radiation crosslinking of other polymers? Radiation Physics and Chemistry, **71**, 261–265 (2004).
DOI: 10.1016/j.radphyschem.2004.03.083

[27] Hildenbrand J. H., Scott R. L.: The solubility of nonelectrolytes. Reinhold, New York (1949).

[28] Flory P. J.: Principles of polymer chemistry. Cornell University Press, Ithaca (1953).

[29] Stern S. A., Frisch H. L.: The selective permeation of gases through polymers. Annual Review of Material Science, **11**, 523–550 (1981).
DOI: 10.1146/annurev.ms.11.080181.002515

[30] Flory P. J., Rehner R. J.: Statistical mechanics of cross-linked polymer networks. II: Swelling. Journal of Chemical Physics, **11**, 521–526 (1943).
DOI: 10.1063/1.1723792

[31] Zagórski Z. P.: Modification, degradation and stabilization of polymers in view of the classification of radiation spurs. Radiation Physics and Chemistry, **63**, 9–19 (2002).
DOI: 10.1016/S0969-806X(01)00475-3

[32] Ghassemi Mahidasht G. R., Gal O., Shafi N., Sang M., Vaklllnejad O. F., Cashmi R.: Effect of trace fillers on radiation crosslinking of polyethylene. Radiation Physics and Chemistry, **25**, 349–357 (1985).
DOI: 10.1016/0146-5724(85)90282-1

[33] Beuerman S., Paquet Jr. D. A., McMinn J. H., Hutchinson R. A.: Determination of free-radical propagation rate coefficients of butyl, 2-ethylhexyl, and dodecyl acrylates by pulsed-laser polymerization. Macromolecules, **29**, 4206–4215 (1996).
DOI: 10.1021/ma960081c

[34] Takács E., Emmi S. S., Wojnárovits L.: Study of polymerization kinetics of acrylic and methacrylic acid esters at low conversions. Radiation Physics and Chemistry, **55**, 621–624 (1999).
DOI: 10.1016/S0969-806X(99)00258-3

eXPRESS Polymer Letters Vol.3, No.8 (2009) 501–509
Available online at www.expresspolymlett.com
DOI: 10.3144/expresspolymlett.2009.62

Curing behavior and thermal properties of trifunctional epoxy resin cured by 4, 4'-diaminodiphenyl sulfone

J. Cheng, J. Li, J. Y. Zhang*

College of Materials Science and Engineering, Beijing University of Chemical Technology, Beijing 100029, China

Received 5 April 2009; accepted in revised form 24 May 2009

Abstract. A novel trifunctional epoxy resin 4-(3, 3-dihydro-7-hydroxy-2, 4, 4-trimethyl-2H-1-benzopyran-2-yl)-1, 3-benzenediol glycidyl (shorted as TMBPBTH-EPOXY) was synthesized in our lab to improve thermal performance. Its curing behavior and performance were studied by using 4, 4′-diaminodiphenyl sulfone (DDS) as hardener with the mass ratio of 100:41 of TMBPBTH-EPOXY and DDS. The curing activation energy was investigated by differential scanning calorimetry (DSC) to be 64.0 kJ/mol estimated by Kissinger's method and 68.7 kJ/mol estimated by Flynn-Wall-Ozawa method respectively. Thermogravimetric analyzer (TGA) was used to investigate the thermal decomposition of cured compounds. It was found that when curing temperature was lower than 180°C, the thermal decomposition temperature increased with the rise of curing temperature and curing time. On the other hand, when the curing temperature was higher than 180°C, the thermal decomposition temperature went down instead with the increase of curing time that might be the over-crosslinking of TMBPBTH-EPOXY and DDS hardener. The glass transition temperature (T_g) of cured TMBPBTH-EPOXY/DDS compound determined by dynamic mechanical thermal analysis (DMTA) is 290.1°C.

Keywords: *thermosetting resins, trifunctional epoxy resin, curing behavior, glass transition temperature, thermal decomposition temperature*

1. Introduction

Epoxy resins have been known to possess good mechanical properties and excellent adhesive properties, and thus have been widely used in industry, such as adhesive, coating, laminating, electronic encapsulating materials, and composite applications [1–7]. However, the conventional epoxy resins are inefficient to satisfy the required properties of advanced materials, such as, high thermal resistance [8–10]. It is known that several ways can be taken to enhance the thermal property of epoxy compound. Firstly, the aromatic ring was introduced into epoxy backbone during synthesis, for example, naphthalene ring and biphenyl group were often used to improve the heat resistance of epoxy resin [11–15]. Secondly, multifunctional epoxy resin is a way to enhance heat-resistant property because of higher curing density [16–18]. Recently, multifunctional epoxy resins attracted extensive interest of researchers and producers, and some multifunctional epoxy resins have been reported and even used in industrial application [19, 20], for example [21–23], novolac epoxy resin, cycloalphatic epoxy resin, tetraglycidyl diamine diphenol methane (TGDDM), triglycidyl ether p-aminophenol (AGF-90) and resorcinol-formaldehyde type epoxy resin (F-76). Some typical structures of multifunctional epoxy resin were showed in Figure 1, which are mainly employed as matrix for high performance fiber-reinforced composites in the aerospace industry and as encapsulant for electronic components.

Thirdly, the properties and performance of cured compounds of epoxy resins are also dependent on

*Corresponding author, e-mail: chengjue@mail.buct.edu.cn

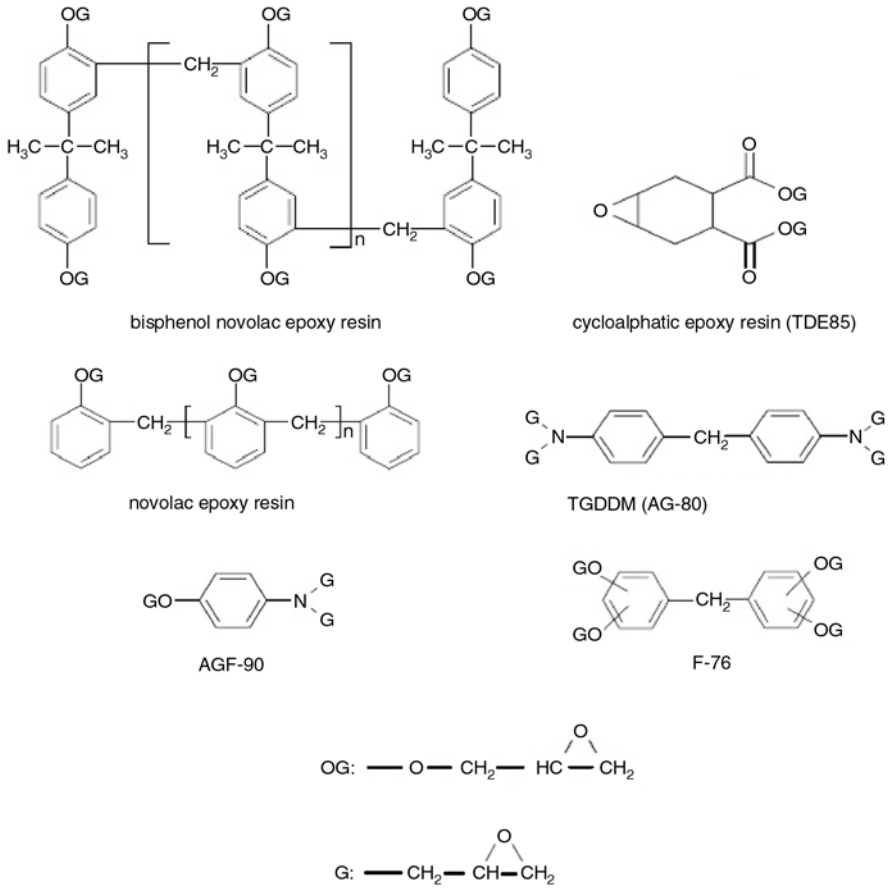

Figure 1. The structures of some typical multifunctional epoxy resins

the type of curing agent, and curing conditions [24]. Among the long list of curing agents, the aromatic primary amines are known to impart high glass transition temperature (T_g) to cured resins, for example, 4, 4′-diaminodiphenyl sulfone (DDS) and 4, 4′-diaminodiphenylmethane (DDM). The T_g of cured resin with DDS as hardener is higher than DDM because of its sulfone structure.

In this paper, the resin is a new kind of trifunctional resin synthesized in our lab [25] with the structure shown in Figure 2 (structure 2), and DDS is chosen as hardener. The aim of our work is to investigate the curing behavior and thermal stability of the novel TMBPBTH-EPOXY/DDS system by Fourier Transform Infrared Spectroscopy (FTIR), differential scanning calorimetry (DSC), dynamic mechan-

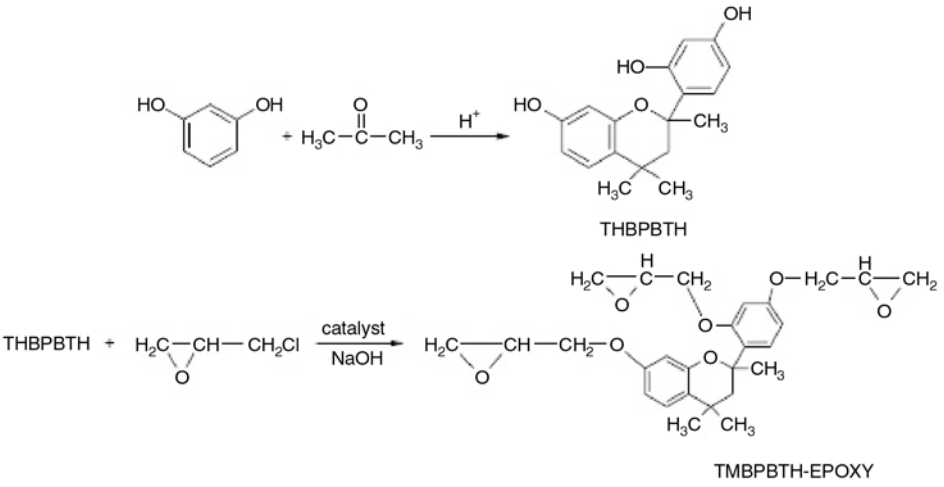

Figure 2. Reaction mechanisms of THBPBTH and TMBPBTH-EPOXY

ical thermal analysis (DMTA), and thermo-gravimetric analysis (TGA). The FTIR was used to monitor the residual epoxide functional groups during the curing process with the curing temperatures changing from 140 to 220°C, and curing time lasting from 1 to 6 hours. DSC was used to investigate the curing kinetics of TMBPBTH-EPOXY/DDS system. DMTA and TGA were used to characterize the glass transition temperature and decomposition temperature of cured compounds as a function of cure temperature, respectively.

2. Materials and methods

2.1. Materials

Epichlorohydrin was supplied by Beijing Chemical Plant. Quaternary ammonium salt was from Tianjin Jinke fine Chemical institute used as phase transition catalyst. NaOH was analytical reagent supplied by Beijing Chemical Plant. DDS was supplied by Shanghai SSS Reagent Co., Ltd. used as curing agent. 4-(3, 3-dihydro-7-hydroxy-2, 4, 4-trimethyl-2H-1-benzopyran-2-yl)-1, 3-benzenediol (THBPBTH) was a trifunctional phenol synthesized by the reaction of resorcinol and acetone [25] and the reaction mechanism was showed in Figure 2.

2.2. Synthesis of trifunctional epoxy resin

TMBPBTH-EPOXY was synthesized by the reaction of described THBPBTH and epichlorohydrin through well-known two-step process with quaternary ammonium salt as catalyst. The THBPBTH and epichlorohydrin react in the four-neck flask equipped with thermometer, vacuum unit, nitrogen tank and peristaltic pump for 1 hour at 100°C under nitrogen atmosphere. Then, NaOH aqueous (50 wt%) is added gradually for another 1.5 hour at 65°C. After reaction the product is dissolved in toluene and washed by deionized water three times. The epoxy resin was obtained after drying under the vacuum. The epoxide equivalent weight (EEW) of TMBPBTH-EPOXY is 161–164 analyzed by hydrocholoride-acetone method. Accordingly, based on the determined EEW value, TMBPBTH-EPOXY mixed with DDS at the weight ratio of 100:41.

2.3. DSC measurements for curing kinetics

A PerkinElmer Pyrisl differential scanning calorimeter was used to investigate the curing behavior of TMBPBTH-EPOXY/DDS in nitrogen atmosphere. TMBPBTH-EPOXY/DDS mixtures (about 4.0 mg each) were subjected to DSC scans at heating rates of 5, 10, 15, and 20 $K \cdot min^{-1}$, respectively, the test specification is from room temperature to 350°C.

The curing reaction kinetic parameters can be evaluated with a multiple-heating-rate method by determining the exothermic peak temperatures at several heating rates. In practice, two convenient multiple-heating-rate methods are generally used. One is the maximum reaction rate method proposed by Kissinger, which is based on the fact that the exothermic peak temperature (T_p) varied with the heating rates. The other is the iso-conversion method proposed by Flynn, Wall, and Ozawa, which is based on the fact that iso-conversion can be reached at different temperatures with various heating rates [26].

Kissinger's approach assumed that the maximum reaction rate occurred at peak temperatures, where $d^2\alpha/dt^2$, it can be expressed by Equation (1):

$$\ln\left(\frac{\beta}{T_p^2}\right) = \ln\left(\frac{AR}{E_a}\right) - \frac{E_a}{RT_p} \tag{1}$$

where α is the state of cure, β is the linear heating rate [$K \cdot min^{-1}$], T_p is he peak temperature [K], A is the pre-exponential factor, E_a is the activation energy, and R is the universal gas constant (R = 8.314 kJ/mol·K). Therefore, a plot of $\ln(\beta/T_p^2)$ versus $1/T_p$ gives the values of E_a and A.

Flynn-Wall-Ozawa method assumes that the degree of conversation at peak temperatures for different heating rates is constant. It can be expressed by Equation (2):

$$\log\beta = -\frac{0.4567E_a}{RT} + C \tag{2}$$

where C is a constant, T is the iso-conversion temperature, and other parameters are the same as described earlier. Plotting $\log\beta$ versus $1/T$ the activation energy can be obtained from the slope.

2.4. FTIR measurements for curing reaction

A Nicolet Nexus 670 spectrometer was used to monitor the variation of epoxide functional groups

of TMBPBTH-EPOXY/DDS system as the function of curing temperature and curing time during curing process. The sample was made into powder, and mixed with potassium bromide, and then it was made as a thin film at room temperature and the resolution was 4 cm^{-1}. The potassium bromide was used as the background.

2.5. TGA measurements for thermal decomposition temperature

A TG209C thermo-gravimetric analyzer produced by Netzsch Company was used to determine the thermal decomposition temperatures of cured materials in nitrogen atmosphere at heating rate of 20 $K \cdot min^{-1}$. The onsets are at about 5% weight loss, the test specification is from room temperature to 600°C.

2.6. T_g analyzed by DMTA

An American Rheometric Scientific DMTA V dynamic mechanical thermal analysis was used to determine the T_g of cured TMBPBTH-EPOXY sample. The bending method was used with a frequency of 1 Hz and a strain level of 0.04% in the temperature range from 20 to 350°C. The heating rate was 5 $K \cdot min^{-1}$. The testing was performed by using rectangular bars of approximate 50×8×2 mm^3. The exact dimensions of each specimen were measured before the scanning.

It can determine continuously in wide temperature or frequency range, and get the relationship of rigidity and damping with temperature, frequency or time in a short time. At the aspect of determining material's glass transition and secondary transition, it has better sensitivity than DTA and DSC.

3. Results and discussion

3.1. Curing kinetics

In Figure 3, the heat flow is plotted as a function of the temperature for four different heating rates. It is seen that the exothermic reaction proceed in a wide temperature range, and the maximum rate temperatures of the curing reaction increased with increasing heating rate. The values of activation energy E_a and A of TMBPBTH-EPOXY/DDS systems can be calculated from the slopes of the linear lines in Figure 4, and all the exothermic peak temperatures

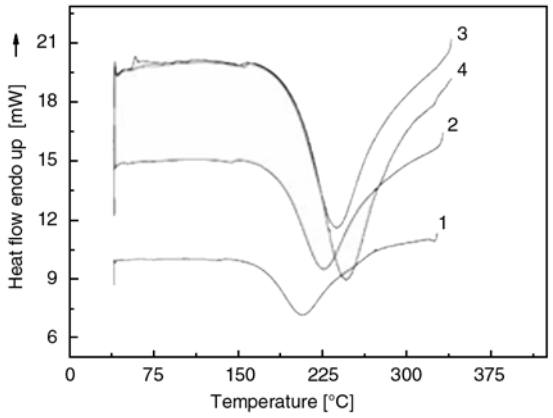

Figure 3. DSC curves of TMBPBTH-EPOXY/DDS. Heating rate: 1 – 5 $K \cdot min^{-1}$; 2 – 10 $K \cdot min^{-1}$; 3 – 15 $K \cdot min^{-1}$; 4 – 20 $K \cdot min^{-1}$.

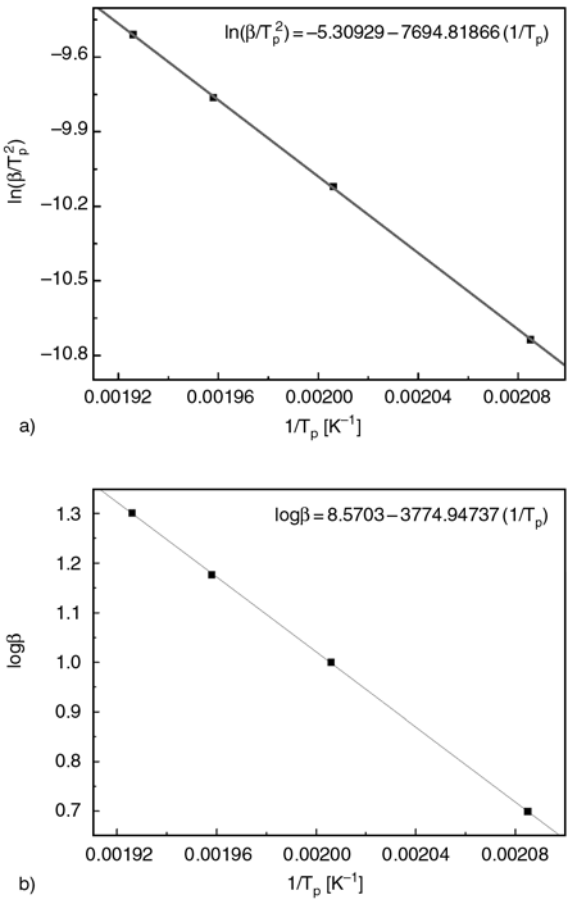

Figure 4. Kinetics analysis of TMBPBTH-EPOXY/DDS curing system TMBPBTH-EPOXY/DDS: a) $\ln(\beta/T_p^2)$–$1/T_p$, b) $\log\beta$–$1/T_p$

(T_p) of the DSC curves at different heating rates are listed in Table 1, and the curing kinetic parameters determined by the Kissinger and Flynn-Wall-Ozawa methods are also summarized in Table 1.

According to the Equation (1), it was calculated that E_a of TMBPBTH-EPOXY/DDS curing system

Table 1. Kinetics data of TMBPBTH-EPOXY/DDS

	β [K·min^{-1}]			
	5	**10**	**15**	**20**
T_p [K]	479.532	498.526	510.674	519.118
$1/T_p$ [×10^{-3}/K]	2.085	2.006	1.958	1.926
lnβ	1.609	2.303	2.708	2.996
logβ	0.699	1.000	1.176	1.301
$\ln(\beta/T_p^2)$	–10.736	–10.121	–9.763	–9.509

is 64.0 kJ/mol, and A is 38.05 s^{-1}. According to Equation (2), it was calculated that E_a of TMBPBTH-EPOXY/DDS curing system is 68.7 kJ/mol.

Because of thermal hysteresis, curing temperatures were different according to different heating rates. However, materials are often cured at constant temperature or stepped heating state actually, because at that time the heating rate is 0 K/min. Therefore, method of extrapolation of T–β is used to get the isothermal curing temperature of curing system, and then determine the best curing process. The data is showed in Table 2, and Figure 5 is T–β analysis, whereas, T_i, T_p and T_0 means onset temperature, peak temperature and end temperature respectively.

When the T–β analysis in Figure 5 are extrapolated until β equals to 0, T_i, T_p and T_0 of isothermal curing would be gained. T_i, T_p and T_0 of TMBPBTH-EPOXY/DDS system is 136.7, 196.1 and 241.1°C

Table 2. DSC data of TMBPBTH-EPOXY/DDS curing system

	β [K·min^{-1}]			
	5	**10**	**15**	**20**
T_i [K]	415.900	425.520	432.515	437.551
T_p [K]	479.532	498.526	510.674	519.118
T_0 [K]	534.391	578.552	603.912	618.820

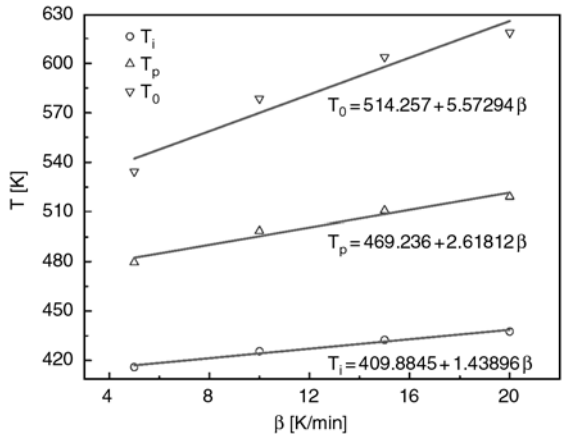

Figure 5. T–β analysis of TMBPBTH-EPOXY/DDS curing system

Table 3. Curing processes of TMBPBTH-EPOXY/DDS curing system

Curing system	Curing process [°C/h]
TMBPBTH-EPOXY/DDS	140/2+200/2+220/4

respectively. The curing system was heated from 136.7 to 196.1°C gradually, and then cured at 196.1°C isothermally for 2 hours; at last, it was heated to 241.1°C and remained for a certain time. Because all of these, the best curing process was determined, which is shown in Table 3.

3.2. FTIR study of curing reaction

The epoxide functional group is the characteristic group in the epoxy resin, and epoxide rings will open under the attack of amine molecule during the curing reaction of epoxy resins by amine curing agent, which will decrease the content of epoxide groups drastically. The curing mechanism of TMBPBTH-EPOXY and DDS is shown in Figure 6. Thus, FTIR is effective method to investigate the curing behavior of epoxy resin by determining the change of functional groups before and after curing reactions of epoxy resin. The experimental results were shown in Figure 7 and Table 4.

Figure 7 presents the FTIR spectra of the cured compound of TMBPBTH-EPOXY/DDS system. The assignments of the absorption features are as follows: about 1595, 1503 cm^{-1} to phenyl group, 1257 cm^{-1} to phenylate, 1104, 1032 cm^{-1} to fatty ether, 910 cm^{-1} to epoxide group and 827 cm^{-1} to the out-of-plane deformation of the aromatic CH.

It can be seen from Figure 7 that after cured at 140°C for 1 hour, the relative absorption intensity of epoxide group still remained obviously, and even if the curing time was increased up to 6 hours the absorption peak at 910 cm^{-1} decreased a little (see Figure 7a and 7b). When the curing temperature was up to 160°C, the absorption intensity at 910 cm^{-1} weakened compared to that cured at 140°C, and 6 hours curing time had a little influence on the opening reaction of epoxide ring compared with 1 hour cured (see Figure 7c and 7d). When the curing temperature was up to 180°C, the absorption peak at 910 cm^{-1} became not clear, especially for the curing time of 6 hours (see Figure 7e and 7f). Furthermore, when the curing temperature rose to 220°C, after cured for 2 hours, the

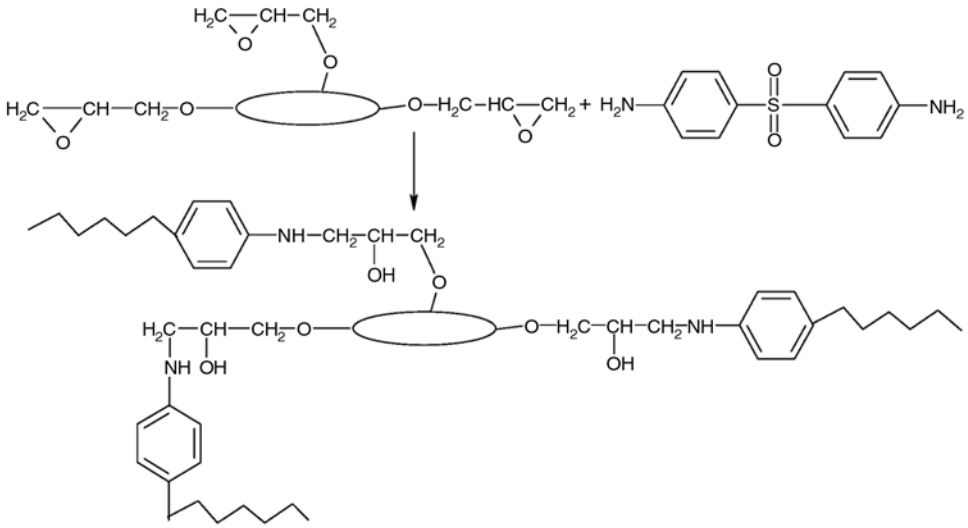

Figure 6. the curing reaction mechanism of THTMBPB-EPOXY with DDS

Table 4. The epoxide groups index of TMBPBTH-EPOXY/DDS system

Curing time [h]	T [°C]			
	140	160	180	220
1	0.0370±0.0008	0.0199±0.0005	0.0144±0.0006	0.0083±0.0004
6	0.0191±0.0006	0.0163±0.0011	0.0142±0.0009	0.0078±0.0009

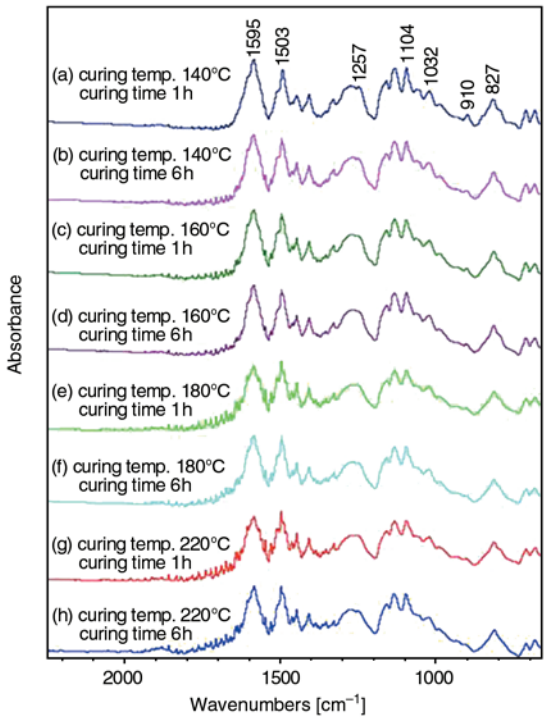

Figure 7. FTIR spectra of the TMBPBTH-EPOXY/DDS system cured at different temperature

absorption intensity of residual epoxide groups at 910 cm^{-1} was tiny, when the curing time reached 6 hours, the absorption peak at 910 cm^{-1} disappeared (see Figure 7g and 7h).

The FTIR analysis results elucidated that curing temperature impacted on the curing reaction more obvious than curing time. In order to show the changes of residual epoxide group with the curing temperature and curing time, the epoxide group index was calculated by using absorption intensity of phenyl groups as internal standard and the calculation equation as follows:

$$\text{Epoxide group index} = \frac{\text{epoxide group's peak area}}{\text{phenyl group's peak area}} = \frac{A_{923-887}}{A_{1680-1548}}$$

The area of epoxide group in FTIR spectra is from 887 to 923 cm^{-1}, the area of phenyl group in FTIR spectra is from 1548 to 1680 cm^{-1}.
The calculated results were shown in Table 4.

3.3. Thermal decomposition temperature of TMBPBTH-EPOXY/DDS system

The thermal decomposition temperatures of cured compounds are different depending on the curing conditions of different curing temperature and curing time. TGA was used to determine thermal decomposition temperatures of TMBPBTH-EPOXY/DDS curing system at curing temperatures of 140, 160,180 and 220°C for curing time of 1, 2,

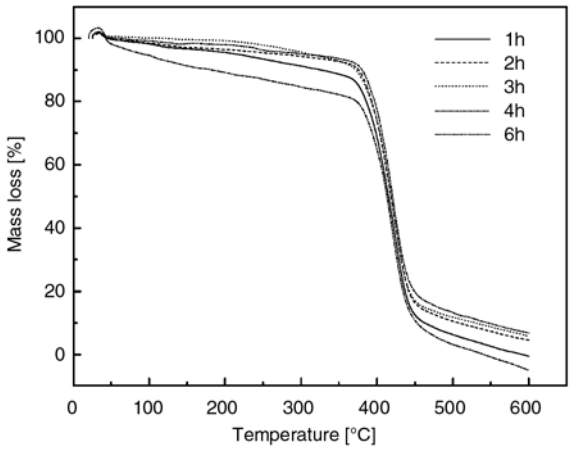

Figure 8. TGA curves of TMBPBTH-EPOXY/DDS curing system cured at 140°C. Curing time: 1, 2, 3, 4, 6 h.

3, 4 and 6 h respectively. The measurement results of sample cured at 140°C were plotted in Figure 8 and all samples results with T_0, T_i and T_e data were listed in Table 5, whereas, T_0, T_i and T_e are onset temperature, middle temperature and offset temperature of thermal decomposition.

It indicated in Table 5 that thermal decomposition temperature increased slightly with the increasing of curing time from 1 to 6 hours at the same curing temperature of 140 and 160°C. This change was attributed to the increase of density of cross linking caused by curing for longer time, which resulted in more perfectly crosslinked network.

Table 5. Thermal decomposition temperatures of TMBPBTH-EPOXY/DDS

Curing temperature [°C]	Curing time [h]	T_0 [°C]	T_i [°C]	T_e [°C]
140	1	389.0	424.6	443.4
	2	389.3	424.2	443.2
	3	391.5	422.3	441.0
	4	393.0	420.3	440.9
	6	394.0	421.2	441.9
160	1	391.1	424.8	443.7
	2	392.1	424.6	443.3
	3	394.9	426.3	443.9
	4	394.6	425.5	443.8
	6	395.3	426.1	442.7
180	1	394.2	425.5	443.1
	2	389.1	424.0	441.7
	3	387.3	422.3	441.6
	4	388.8	423.4	442.6
	6	386.3	420.8	440.7
220	1	396.4	426.6	442.9
	2	392.3	425.4	444.4
	3	390.8	424.3	441.4
	4	390.7	424.3	443.5
	6	390.6	424.5	443.1

However, thermal decomposition temperatures decreased slightly with the increasing of curing time from 1 to 6 hours at 180 and 220°C. This change can be explained to excess cross linking of epoxy resin and hardener, or overcured which gave inner stress and then deficiency appeared. These deficiencies made the thermal decomposition temperature declined. With the increase of curing time the deficiencies became more serious and decomposition temperature decreased gradually.

However, thermal decomposition temperatures cured at 180 and 220°C are higher than cured at 140 and 160°C, it means high curing temperature is more helpful for curing reaction, and the increasing of curing time has advantageous effect on curing reaction when the curing temperature is lower than 160°C. This is coincident with the analysis of FTIR.

3.4. Glass transition temperature of epoxy resin network

T_g of an epoxy resin network is the reflection of the structure for different epoxy resins when the curing reaction is complete.

DMTA is used to determine dynamic mechanical property of materials in a certain temperature range. Here, TMBPBTH-EPOXY/DDS curing system was studied by DMTA at fixed frequency. At fixed frequency, the value of tanδ reaches maximum at glass transition temperature, so the value of T_g can determined by the curve of tanδ.

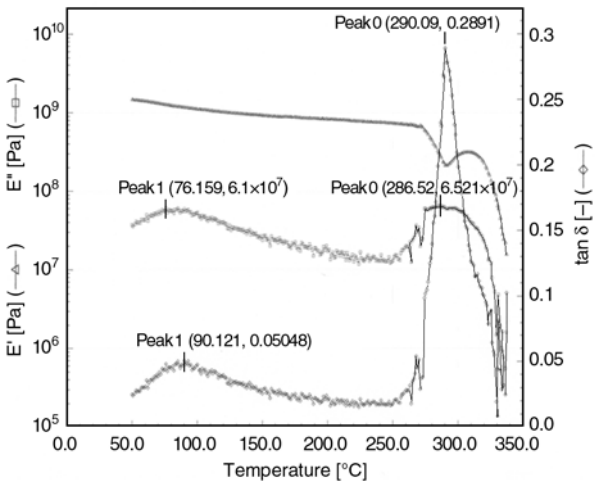

Figure 9. DMTA curve of TMBPBTH-EPOXY/DDS curing system

Figure 9 is DMTA spectra of TMBPBTH-EPOXY/DDS. T_g of TMBPBTH-EPOXY/DDS curing system is about 290.1°C.

4. Conclusions

DSC studies show that the curing activation energies of TMBPBTH-EPOXY/DDS systems are 64.0 kJ/mol estimated by Kissinger's approach and 68.7 kJ/mol estimated by Flynn-Wall-Ozawa method respectively. FTIR studies indicates that state of cure of TMBPBTH-EPOXY/DDS curing system is mainly dependent on curing temperature and it is increased with increasing temperature, however, it changed a little with increasing curing time at the same curing temperature. TGA studies presents that thermal decomposition temperature increased with increasing curing temperature and time, but it is declined at 180 and 220°C for more than 1 h curing time because of overcuring. The DMTA studies elucidated that T_g of TMBPBTH-EPOXY/DDS is 290.1°C.

References

[1] Gu J., Narang S. C., Pearce E. M.: Curing of epoxy resins with diphenyliodonium salts as thermal initiators. Journal of Applied Polymer Science, **30**, 2997–3007 (1985).
DOI: 10.1002/app.1985.070300722

[2] Kaji M., Nakahara K., Endo T.: Synthesis of a bifunctional epoxy monomer containing biphenyl moiety and properties of its cured polymer with phenol novolac. Journal of Applied Polymer Science, **74**, 690–698 (1999).
DOI: 10.1002/(SICI)1097-4628(19991017)74:3<690::AID-APP23>3.0.CO;2-X

[3] Morgan R. J., Mones E. T., Steele W. J.: Tensile deformation and failure processes of amine-cured epoxies. Polymer, **23**, 295–305 (1982).
DOI: 10.1016/0032-3861(82)90320-2

[4] Lee J-Y., Shim M-J., Kim S-W.: Autocatalytic cure kinetics of natural zeolite filled epoxy composites. Materials Chemistry and Physics, **48**, 36–40 (1997).
DOI: 10.1016/S0254-0584(97)80073-9

[5] Lee J. Y., Shim M. J., Kim S. W.: Thermal decomposition kinetics of an epoxy resin with rubber-modified curing agent. Journal of Applied Polymer Science, **81**, 479–485 (2001).
DOI: 10.1002/app.1460

[6] Lee H., Neville K.: Handbook of epoxy resins. McGraw-Hill, New York (1967).

[7] May C. A., Tanaka Y.: Epoxy resins chemistry and technology. Marcel Decker, New York (1973).

[8] Shieh J-Y., Wang C-S.: Synthesis and properties of novel phosphorus-containing hardener for epoxy resins. Journal of Applied Polymer Science, **78**, 1636–1644 (2000).
DOI: 10.1002/1097-4628(20001128)78:9<1636::AID-APP90>3.0.CO;2-G

[9] Iji M., Kiuchi Y.: Flame-retardant epoxy resin compounds containing novolac derivatives with aromatic compounds. Polymers for Advanced Technologies, **12**, 393–406 (2001).
DOI: 10.1002/pat.66

[10] Wang C. S., Lin C. H.: Synthesis and properties of phosphorus containing advanced epoxy resins. Journal of Applied Polymer Science, **75**, 429–436 (2000).
DOI: 10.1002/(SICI)1097-4628(20000118)75:3<429::AID-APP13>3.0.CO;2-U

[11] Wang C-S., Lee M-C.: Synthesis and modification of a naphthalene-containing trifunctional epoxy resin for electronic applications. Journal of Applied Polymer Science, **70**, 1907–1921 (1998).
DOI: 10.1002/(SICI)1097-4628(19981205)70:10<1907::AID-APP5>3.0.CO;2-Y

[12] Wang C-S., Lee M-C.: Synthesis, characterization, and properties of multifunctional naphthalene-containing epoxy resins cured with cyanate ester. Journal of Applied Polymer Science, **73**, 1611–1622 (1999).
DOI: 10.1002/(SICI)1097-4628(19990829)73:9<1611::AID-APP2>3.0.CO;2-8

[13] Kaji M., Endo T.: Synthesis of a novel epoxy resin containing naphthalene moiety and properties of its cured polymer with phenol novolac. Journal of Polymer Science Part A: Polymer Chemistry, **37**, 3063–3069(1999).
DOI: 10.1002/(SICI)1099-0518(19990815)37:16<3063::AID-POLA3>3.0.CO;2-H

[14] Cai Z-Q., Sun J., Zhou Q., Xu J.: Synthesis and characterization of a novel liquid-crystalline epoxy resin combining biphenyl and aromatic ester-type mesogenic units. Journal of Polymer Science Part A: Polymer Chemistry, **45**, 727–735(2007).
DOI: 10.1002/pola.21821

[15] Han S., Yoon H. G., Suh K. S., Kim W. G., Moon T. J.: Cure kinetics of biphenyl epoxy-phenol novolac resin system using triphenylphosphine as catalyst. Journal of Polymer Science Part A: Polymer Chemistry, **37**, 713–720 (1999).
DOI: 10.1002/(SICI)1099-0518(19990315)37:6<713::AID-POLA6>3.0.CO;2-I

[16] Carrasco F., Pagès P., Lacorte T., Briceño K.: Fourier transform IR and differential scanning calorimetry study of curing of trifunctional amino-epoxy resin. Journal of Applied Polymer Science, **98**, 1524–1535 (2005).
DOI: 10.1002/app.21978

[17] Mustat'a F., Bicu I.: Multifunctional epoxy resins: Synthesis and characterization. Journal of Applied Polymer Science, **77**, 2430–2436 (2000).
DOI: 10.1002/1097-4628(20000912)77:11<2430::AID- APP11>3.0.CO;2-P

[18] Becker O., Cheng Y-B., Rusell J. V., Simon G. P.: Layered silicate nanocomposites based on various high-functionality epoxy resins: The influence of cure temperature on morphology. Mechanical properties, and free volume. Macromolecules, **36**, 1616–1625 (2003).
DOI: 10.1021/ma0213448

[19] Ochi M., Shimizu Y., Nakanishi Y., Murata Y.: Effect of the network structure on thermal and mechanical properties of mesogenic epoxy resin cured with aromatic amine. Journal of Polymer Science Part B: Polymer Physics, **35**, 397–405 (1997).
DOI: 10.1002/(SICI)1099-0488(19970130)35:2<397::AID-POLB15>3.0.CO;2-D

[20] Wang C-S., Lee M-C.: Synthesis and properties of epoxy resins containing 2-(6-oxid-*6H*-dibenz(c,e) (1,2) oxaphosphorin-6-yl) 1,4-benzenediol (II). Polymer, **41**, 3631–3638 (2000).
DOI: 10.1016/S0032-3861(99)00541-8

[21] Atta A. M., Shaker N. O., Nasser N. E.: Synthesis of bisphenol A novolac epoxy resins for coating applications. Journal of Applied Polymer Science, **107**, 347–354 (2008)
DOI: 10.1002/app.26981

[22] Qian Z., Chen X., Xu J., Guo B.: Chain extension of PA1010 by reactive extrusion by diepoxide 711 and diepoxide TDE85 as chain extenders. Journal of Applied Polymer Science, **94**, 2347–2355 (2004).
DOI: 10.1002/app.21043

[23] Park S-J., Jin F-L., Lee J-R.: Thermal and mechanical properties of tetrafunctional epoxy resin toughened with epoxidized soybean oil. Materials Science and Engineering: A, **374**, 109–114 (2004)
DOI: 10.1016/j.msea.2004.01.002

[24] Jain R., Kukreja P., Narula A. K., Chaudhary V.: Studies of the curing kinetics and thermal stability of epoxy resins using a mixture of amines and anhydrides. Journal of Applied Polymer Science, **100**, 3919–3925 (2006).
DOI: 10.1002/app.22769

[25] Jue C., Jing C., Junying Z., Wantai Y.: Preparation process of polyalkyl hydroxyl benzodihydro pyran derivative. Chinese Patent, 200610113693, China (2008).

[26] Liu Y., Du Z., Zhang C., Li C., Li H.: Curing behavior and thermal properties of multifunctional epoxy resin with methylhexahydrophthalic anhydride. Journal of Applied Polymer Science, **103**, 2041–2048 (2007).
DOI: 10.1002/app.25291

eXPRESS Polymer Letters Vol.3, No.8 (2009) 510–517
Available online at www.expresspolymlett.com
DOI: 10.3144/expresspolymlett.2009.63

Synthesis and properties of new amphoteric poly(amidoamine) dendrimers

X. C. Peng[1*], *X. H. Peng*[2], *S. M. Liu*[2], *J. Q. Zhao*[2]

[1]Department of Chemistry and Chemical Engineering, Jishou University, Hunan 416000, China
[2]College of Materials Science and Engineering, South China University of Technology, Guangzhou 510640, China

Received 30 March 2009; accepted in revised form 26 May 2009

Abstract. A series of new amphoteric dendrimers have been synthesized by attaching dimethylbenzylaminoethyl acrylate chloride (Bz80), sodium acrylic acid (SAA) and modified polyoxyethylene (MPEO) units to a third-generation poly(amidoamine) (PAMAM) dendrimer core via Michael addition reaction. The structure of the dendrimers was confirmed by Fourier transform infrared (FTIR), proton nuclear magnetic resonance (^{1}H NMR), carbon 13 nuclear magnetic resonance (^{13}C NMR) spectroscopy and by elemental analysis. Thermal stability and intrinsic viscosity were investigated. The applicable experiment exhibited the amphoteric dendrimers have high flocculation efficiency, which could be significantly improved by combining amphoteric dendrimers with polyacrylamide (PAM). The suitable mass ratio of the dendrimers and PAM was 2:3. The study would promote the use of amphoteric dendrimers as a flocculant in treating wastewater and as a new paper retention aid in papermaking.

Keywords: *nanocomposites, poly(amidoamine) (PAMAM), polyoxyethylene, amphoteric dendrimers, flocculation efficiency*

1. Introduction

Dendrimers are highly branched macromolecules possessing a large surface area to volume ratio with well-defined interior and exterior regions. A large number of terminal groups on the dendrimers, in which each round of synthesis (or 'generation') geometrically increases the number of units added, are available for further functionalization. These terminal groups influence the solubility and adhesive properties of dendrimers. These characteristics of dendrimers confer unique chemical and physical properties, which provide the impetus for further studies of this class of macromolecules [1–5].

Currently, most of PAMAM dendrimers surface-modified by cationic [6, 7], anionic [8, 9] and PEG chain [10–12] have been used as drug delivery carrier. Allen and Polverari [13] investigated poly (propylene imine) (PPI) dendrimers as new retention aids in the production of newsprint, mechanical printing grades, and boards. These dendrimers were found to be very effective retention aids for fines, dispersed extractives, and ash in papermaking. They claimed that a retention system of dendrimers could increase not only the retention rate of pulp fines and fillers but also the paper machine dehydration velocity and could effectively remove resin and plastic ropy materials. PAMAM dendrimers can also serve as flocculants for the dyeing wastewater treatment [14] and silica scale growth inhibitors that relates to industrial water treatment [15–17]. In general, these modified dendrimers are cationic or nonionic polymers. There has been little work reported on amphoteric dendrimers modification. Our previous study on the surface-modified cationic PAMAM dendrimers indicated that they had excellent performances in flocculating and

*Corresponding author, e-mail: pnfxz@126.com

wastewater treatment [18]. In this paper a series of new-type amphoteric dendrimers with rigid branched structure were designed. The branching molecules were prepared by attaching dimethylbenzylaminoethyl acrylate chloride, sodium acrylic acid or modified polyoxyethylene units to a third-generation poly(amidoamine) dendrimer core via Michael addition reaction. MPEO was employed as a major component in the modified dendrimers because of not only its long chain which can control dendrimer molecule size with various molecule weights but also the structure which benefits for increasing flocculation bridge. A series of MPEO were prepared by the reaction of various molecule weight PEG with acrylchloride. Intrinsic viscosity, thermal stability and flocculation efficiency of the dendrimers were presented.

2. Experimental

2.1. Materials

Poly(amidoamine) (PAMAM, G3.0) dendrimer was prepared by a divergent synthesis method starting from ethylenediamine by consecutive Michael addition and ester amidation reaction. It was based on an ethylenediamine core, and branched units were composed of both methyl acrylate and ethylenediamine [18]. Modified polyoxyethylenes (MPEO, Mr = 454, 654, 1054) were prepared according to the reported procedure [19]. Dimethylbenzylaminoethyl acrylate chloride (Bz80), sodium acrylic acid (SAA) and polyacrylamide (PAM, VN728) were commercial products and used as received. Other organic reagents employed in the investigation were analytical reagents. They were used without further purification. Poly(tetrafluoroethylene) membrane (D34mm, 3500) was obtained from Tianjing Lianxin Biotechnology Co., Ltd.

2.2. Instruments

^{1}H NMR and ^{13}C NMR spectra were recorded with a Bruker DRX-400 NMR spectrometer. FTIR measurements were carried out by a Nicolet MAGNA-IR 760 spectrophotometer via the KBr pellet method. Elemental analysis was run in an Elementer Vario EL instrument. Paper Forming Model 255 instrument (MESSMER INSTRUMENTS), Standards Paper Squeezer PNP Model (MESSMER INSTRUMENTS). TGA data were recorded with a TGA 2050, V5.4A instruments (USA). Absorbance was performed using a 721 spectrophotometer.

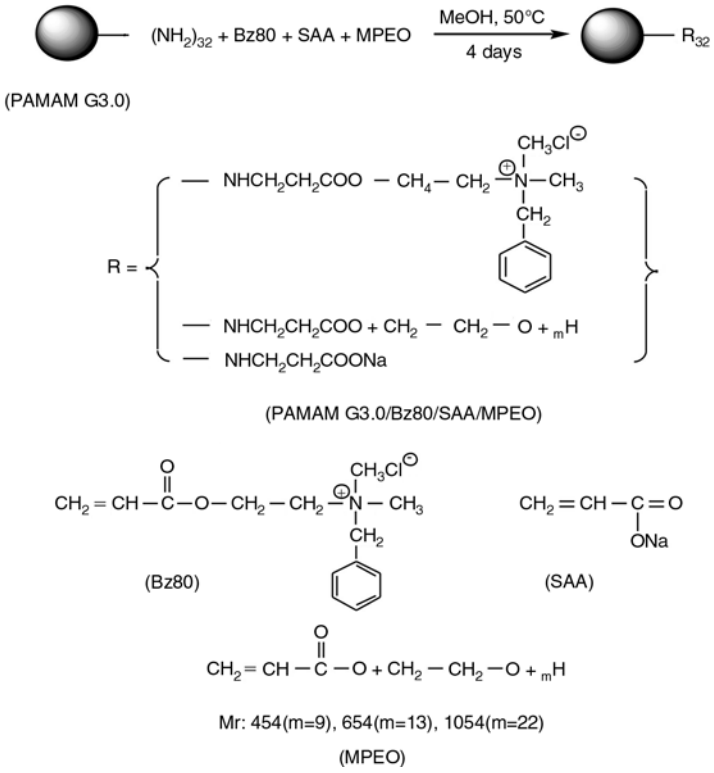

Figure 1. Surface modification of PAMAM G3.0 with Bz80, SAA and MPEO

2.3. Synthesis of the amphoteric PAMAM dendrimers

PAMAM G3.0/Bz80/SAA/MPEO dendrimers were prepared according to Figure 1.

Michael addition reaction was carried out in a water bath of 50°C with a 500 ml, three-necked, round-bottom flask fitted with a condenser and a magnetic stirrer under nitrogen. PAMAM G3.0 dendrimer was dissolved in methanol to an appropriate concentration, and then required amounts of Bz80, SAA and MPEO were introduced to the reaction flask. After 4 day reaction insoluble materials was filtered to be removed and the residue soluble in methanol was heated under reflux in 50 ml diethyl ether for 30 min. The residue was filtered through a poly(tetrafluoroethylene) membrane. The product was dried in a vacuum oven at 40°C for 48 h. The purified product was obtained as golden transparent ropy material. Three kinds of amphoteric PAMAM dendrimers (P_1, P_2, P_3) were prepared by using three different molecular weight MPEO (Mr = 454, 654, 1054) and the yield was 72.4–78.2%.

Elemental analysis was performed for P_1, P_2 and P_3. Found (%) of P_1: C 53.20, H 8.06, N 11.16; Calcd (%) according to nominal molecular formula $C_{724}H_{1318}O_{232}N_{132}Cl_{10}Na_{10}$: C 53.77, H 8.21, N 11.43. Found (%) of P_2: C 53.15, H 8.30, N 9.78. Calcd (%) for $C_{820}H_{1510}O_{280}N_{132}Cl_{10}Na_{10}$: C 53.86, H 8.32, N 10.11; Found (%) of P_3: C 53.87, H 8.32, N 7.94. Calcd (%) for $C_{1036}H_{1942}O_{388}N_{132}Cl_{10}Na_{10}$: C 54.0, H 8.49, N 8.02. Found and calculated results are quite consistent for the three dendrimers.

2.4. Property measurement

Intrinsic viscosity of the amphoteric PAMAM dendrimers was detemined by Ubbelchde viscosity measurement at 25°C in methanol solution. Thermal decomposition properties were conducted with a TGA 2050 in N_2 atmosphere.

Flocculation efficiency of the amphoteric PAMAM dendrimers was measured as follows. A 80 ml printing and dyeing wastewater was add in the 250 ml beaker, and then an appropriate concentration of amphoteric PAMAM dendrimers was introduced to the container. After the mixture was magnetic stirrer at room temperature for 10 min, the residue was filtrated. The required amounts of filter liquor (such as 1, 2, 4, 6 and 8 ml) was put into 50 ml volumetric flask and diluted to scale with distilled water, then the concentration ratio was 0.02, 0.04, 0.08, 0.12 and 0.16, respectively. Using 721-type spectrophotometer at λ = 454 nm measured absorbance of different concentrations to compare the effect of their flocculation.

The retention efficiency of the amphoteric PAMAM dendrimers was measured as follows. The test was operated according to a manual papermaking process with a 12.2 g broadleaf pulp. After pulp was put into the papermaking machinery, 0.1% retention aid was added to the pulp. Then, a manual papermaking test was carried out. The retention rate (r_{pu}) was calculated from Equation (1):

$$r_{pu} = \frac{m_{pa}}{m_{pu}} \cdot 100\% \quad (1)$$

where m_{pa} is the dry mass of the paper and m_{pu} is the absolute dry mass of the pulp.

3. Results and discussion

3.1. Characterization of the amphoteric PAMAM dendrimers

The obtained amphoteric PAMAM dendrimers P_1, P_2 and P_3 have almost similar characteristic architectures. The results of FTIR, ^{1}H NMR, ^{13}C NMR of P_3 are shown as the follows.

P_3(PAMAM G3.0/Bz80/SAA/MPEO$_{Mr=1054}$) FTIR peaks: (KBr) cm^{-1}, 2918(s), 2874(s), 1641(s) (amide I), 1559(s) (amide II), 1457(m),1103, 950(s), 3413(s), 1724(m), 1350, 1241(m), 772, 715(s), 600(m); ^{1}H (D_2O, 400 MHz) δ(ppm) 7.40, 7.56, 8.15, 4.68, 3.61, 3.27–3.53, 3.20, 2.58, 2.72, 2.32, 2.62–2.66, 2.52; ^{13}C($CDCl_3$,100 MHz): δ(ppm) 174.73, 174.24, 172.85, 164.35, 160.23, 133.28, 132.45, 131.79, 129.56, 68.80, 65.59, 54.02, 55.65, 49.61, 49.77, 47.45, 38.76, 35.54, 32.98.

In FTIR spectrum two peaks, one at 1641 cm^{-1} (amide I) and the other at 1559 cm^{-1} (amide II), are assigned to the asymmetric stretching vibration (C=O) and the bending vibration (N–H) of HN–C=O (PAMAM dendrimers). The characteristic peaks of ether group (C–O–C) are found at 1103 and 950 cm^{-1}, respectively, which come from PEO. The peak at 3413 cm^{-1} due to –OH stretching vibration is evident. The characteristic peaks of methyl (–N–CH_3), phenyl (–C_6H_5) and chlorine

groups (–CH_3Cl^-) are found at 1350, 1241, 772, 715 and 600 cm^{-1}. The results indicate that Bz80 and PEO chain are successfully attached to PAMAM dendrimer. In addition, the peak at 1724 cm^{-1} due to stretching vibration(C=O) of carboxyl groups suggests that a chain of SAA is successfully attached to the terminal groups of PAMAM G3.0 dendrimer.

^1H NMR and ^{13}C NMR also provide the same evidence. The single peak at δ 4.68 ppm is associated with ether bond methylene protons (CH_2CH_2–O–) in ^1H NMR spectrum. Similarly, a series of strong peaks due to methyl groups protons appear in the region of δ 3.27–3.53 ppm (–CH_3Cl^-) and the characteristic peaks of phenyl (–C_6H_5) appear in δ 7.40, 7.56, 8.15 ppm, which come from Bz80 monomer. Furthermore, the results of ^{13}C NMR spectral data are also depicted. The signals at δ 68.80, 65.59 ppm (–CH_2CH_2–O–) evidence the formation of the dendrimers. The characteristic peaks of the amphoteric PAMAM dendrimer appear at δ 133.28, 132.45, 131.79, 129.56 ppm and δ 49.61 ppm, which represent the –C_6H_5 and –N–CH_3 groups that come from Bz80 monomer. The peak values at δ 164.35, 160.23 ppm represent –COO– group. The results show the amphoteric PAMAM dendrimer is synthesized.

3.2. Intrinsic viscosity of the amphoteric PAMAM dendrimers

In general, intrinsic viscosity of polymer was used to investigate intermolecule or intramolecule interaction beween polymer and solvent. Yamakawa [20] and Long *et al.* [21] investigated the hydrodynamic radius (R_η) of dendrimers according to an intrinsic viscosity measurement. The molecular volume of dendrimers can be calculated from Equation (2):

$$[\eta] = 10\pi R_\eta^3 N_A \tag{2}$$

Then the hydrodynamic radius (R_η) would be (Equation (3)):

$$R_\eta = \left\{\frac{3M[\eta]}{10\pi N_a}\right\}^{\frac{1}{3}} \tag{3}$$

where M is the molecular weight and N_A is the Avgadro constant. Therefore, for each amphoteric PAMAM dendrimer, hydrodynamic radius can be calculated using measured intrinsic viscosity. The date presented in Table 1 illustrates the intrinsic viscosity [η] and hydrodynamic radius R_η of amphoteric PAMAM dendrimer.

Table 1. Intrinsic viscosity [η] and hydrodynamic radius R_η of amphoteric PAMAM dendrimers at 25°C

Dendrimers	Molecular weight Mr [cal. val.]	Intrinsic viscosity [η] [d1·g^{-1}]	Hydrodynamic radius R_η [nm]
PAMAM G3.0	$6.91\cdot10^3$	$5.50\cdot10^{-2}$	1.82
P_1	$1.65\cdot10^4$	$5.64\cdot10^{-2}$	2.44
P_2	$1.86\cdot10^4$	$5.82\cdot10^{-2}$	2.57
P_3	$2.30\cdot10^4$	$4.13\cdot10^{-2}$	2.46

It is clear from Table 1 that P_2 has a maximum intrinsic viscosity value ($5.8\cdot10^{-2}$ d1·g^{-1}), and the hydrodynamic radius R_η was 2.57 nm. P_3, however, has smaller intrinsic viscosity value ($4.1\cdot10^{-2}$ d1·g^{-1}) than PAMAM G3.0 dendrimer, but has larger hydrodynamic radius R_η. On the one hand, this may be due to the effect of some charge repulsive force interaction of the amphoteric PAMAM dendrimers. On the other hand, the length of PEO chain results in an increased twist onto the dendrimer surface. Therefore, the exterior terminal groups are main cause to affect intrinsic viscosity of dendrimers.

The amphoteric PAMAM dendrimers are water-soluble dendrimers. They are insoluble in diethyl ether, petroleum ether, but are highly soluble in carbon tetrachloride, trichloromethane.

3.3. Thermal decomposition of the amphoteric PAMAM dendrimers

Figure 2 shows the TGA and DTG traces of PAMAM G3.0 dendrimer, P_1, P_2 and P_3 in N_2. It is apparent that the thermal stepwise decomposition of the dendrimers contains signals originating from both PAMAM G3.0 dendrimer and the amphoteric PAMAM dendrimers. There is 26.7% mass loss from room temperature to 160°C in the TGA curve of PAMAM G3.0, mainly attributed to the decomposition of the amine-terminal groups of the peripheral dendrimer. A mass loss of 55.7% occurs in the range of 220–350°C and the maximal peak rate temperature (T_{max}) appears at 289°C, assigned to decomposition of the PAMAM G3.0 dendrimer inner layer. Compared to the two-step mass loss of PAMAM G3.0, three-step mass loss trend of the amphoteric PAMAM dendrimers become more and

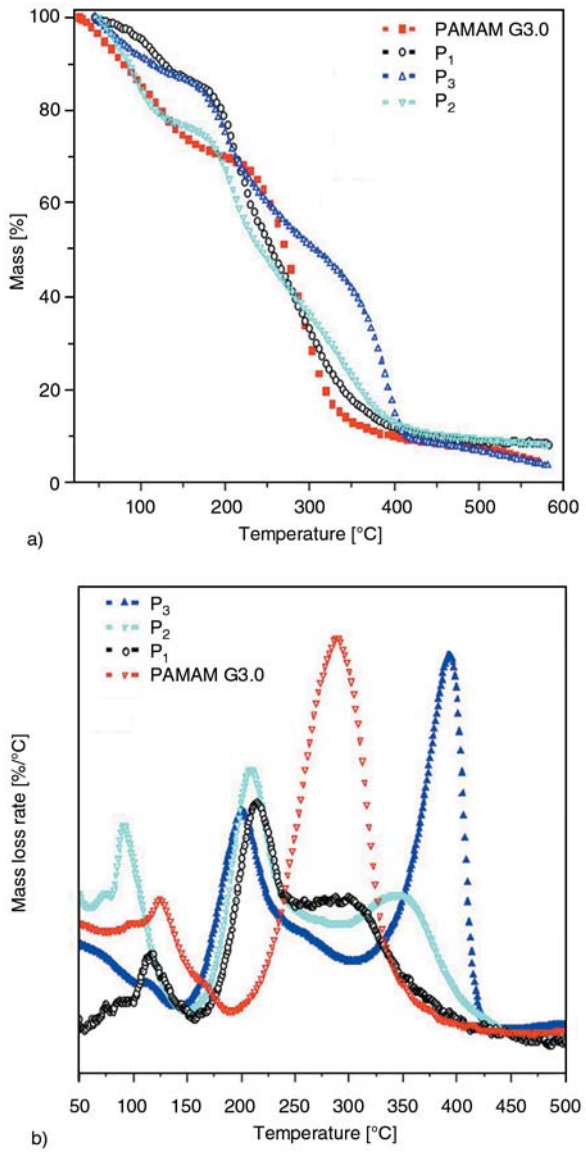

Figure 2. TGA (a) and DTG (b) curves of PAMAM G3.0, P_1, P_2 and P_3

more evident with increasing molecular weight of used PEO. Three-step decomposition of P_3 is apparently observed in DTG curve. The initial mass loss from room temperature to 120°C is 11.3%, mainly attributed to the decomposition of the Bz80 and SAA chains bond of the peripheral dendrimer. The second stage from 175 to 275°C results in a mass loss of 28.5% due to the PAMAM G3.0 dendrimer thermal decomposition and PEO chain breakage, and the maximal mass loss temperature at 200°C. In the third stage of mass loss, P_3 shows a rapid weight loss of 40.5% from 300 to 410°C, corresponding to a spot of rudimental nucleus of the PAMAM dendrimer and PEO and the peak temperature at 392°C. The results of P_1 and P_2 are almost

Table 2. TGA and DTG analysis of amphoteric PAMAM dendrimers

Samples	Temperature range [°C]	Mass loss [%]	T_{max} [°C]
PAMAM G3.0	25–160	26.7	289
	220–350	55.7	
P_1	25–120	10.0	213
	175–275	42.4	
	300–410	21.8	
P_2	25–120	20.8	208
	175–275	33.5	
	300–410	24.7	
P_3	25–120	11.3	392
	175–275	28.5	
	300–410	40.5	

the same as P_3. The data are presented in Table 2. The thermal stability of P_3 is more excellent than that of P_1 and P_2. It can be concluded from the experimental results that the chain length of PEO affects the thermal decomposition behavior of the amphoteric PAMAM dendrimers, and the longer chain length of PEO has a better thermal stability in nitrogen. This may be because the amphoteric PAMAM dendrimers peripheral terminated groups and linear PEO chains could form the dendritic sphericity architecture. On the one hand, efficiency of the charge adsorption produces aggregation intermolecular; on the other hand, the longer chain length of PEO is the easier twist among the peripheral dendrimers. Therefore the thermal stability is enhanced.

3.4. Flocculation efficiency of the amphoteric PAMAM dendrimers

Decolorizing rate (d_r) of printing and dyeing wastewater disposed by the amphoteric PAMAM dendrimers are used to estimate their flocculating performances. The results for P_1, P_2 and P_3 (λ = 454 nm) are shown in Figure 3.

It can be seen from Figure 3a that an effective flocculation occurred when the flocculation system of amphoteric PAMAM dendrimers was used. The flocculation efficiency of P_3 was superior to P_1 and P_2. One possible reason is that its molecule architecture is beneficial to bridge and charge neutralization coagulation. It has already been found that the combined use of the amphoteric PAMAM dendrimers and PAM can significantly enhance the flocculation efficiency. The flocculation results

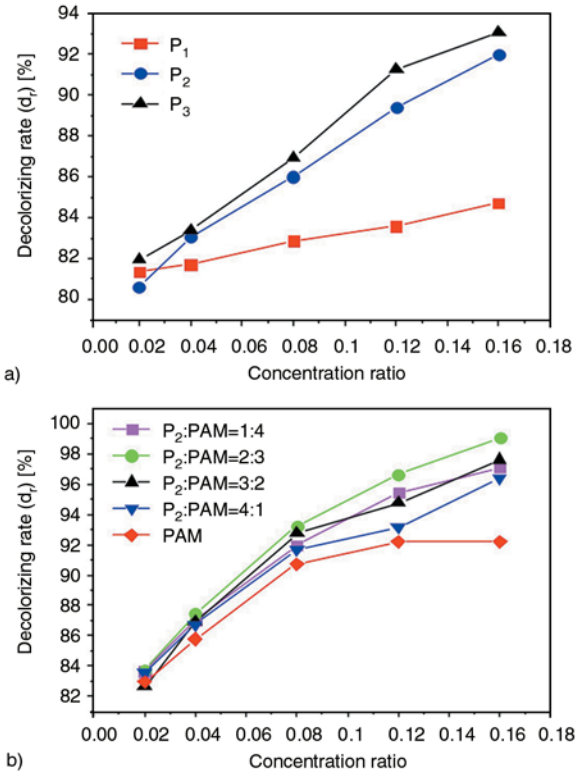

Figure 3. Decolorizing rate of flocculated wastewater disposed by a) P_1, P_2 and P_3; b) a combination of P_3 and PAM in different ratios; decolorizing rate: $d_r=(1–A_1/A_2)\cdot100\%$, where A_1 is the absorbance of the flocculated wastewater and A_2 is the absorbance of the wastewater

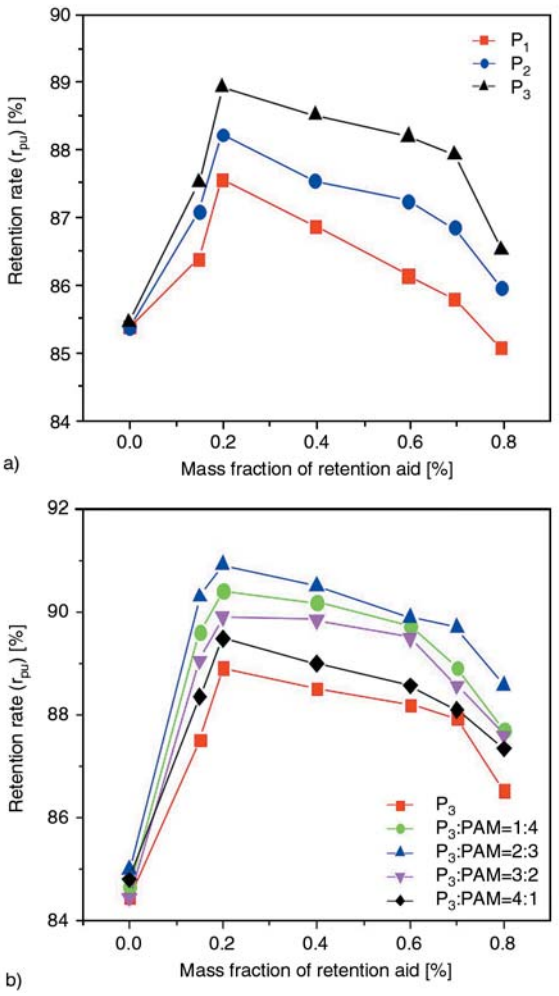

Figure 4. Effect of retention rate for various mass fraction of retention aid

obtained by the combination of P_3 and PAM are shown in Figure 3b. It can be seen that higher flocculation efficiency is produced when the mass ratio of P_3 and PAM is 2:3. The suggested flocculation mechanism may be that the amphoteric PAMAM dendrimers first create effective patches on the solid suspension of wastewater surface, and then PAM with high affinity to the particle surface makes bridges through those charged patches.

The other investigation is to determine the retention efficiency of the dendrimers as a retention aid in manual papermaking. The experiments were performed in a conventional manual papermaking procedure. The effects of retention rate for various mass fraction of retention aid are given in Figure 4. As can be seen in Figure 4a and 4b an evident initial increase in retention rate (r_{pu}) happens with increasing mass fraction of retention aid until the maximum value. Thereafter a decrease in retention rate occurs with increasing retention aid. A suitable mass fraction of retention aid is about 0.2%. P_3 shows the highest retention performance whose retention rate achieves 89.4%. P_2 and P_1 are about 88.2 and 87.5%, respectively. The results clearly indicate that the longer chain length of PEO can induce the better retention efficiency. The retention rate can be significantly improved if the amphoteric PAMAM dendrimers are used in combination with PAM. The suitable mass ratio of P_3 and PAM is 2:3, and the maximum value of retention rate reaches 90.9%. All these effects can be explained by assuming that the amphoteric PAMAM dendrimers have particular molecule architecture, which has not only highly branched core-shell structure of dendrimers but also many long linear arms. The possible mechanism for this flocculation system is mainly through microparticle bridging in which fines or fillers can be captured and is subsequently swept up by the fibers. As a result, both the linear PAM and P_3 which has a long chain of PEO into liquid to from more effective bridge, and thus give better retention efficiency.

4. Conclusions

The amphoteric PAMAM dendrimers were synthesized based on Michael addition reaction of PAMAM G3.0 dendrimer with dimethylbenzylaminoethyl acrylate chloride (Bz80), sodium acrylic acid (SAA) and modified polyoxyethylene (MPEO) groups. FTIR, ^{1}H NMR, ^{13}C NMR and elemental analysis characterized the new dendrimers. These results demonstrated that the prepared dendrimers were composed of chain units of PAMAM G3.0, Bz80, SAA and MPEO. The exterior terminal groups of amphoteric PAMAM dendrimers were main cause to affect intrinsic viscosity, thermal stability and flocculation efficiency of the dendrimers. The flocculation efficiency of the amphoteric PAMAM dendrimers can be significantly improved by the combination of PAM. The dendrimers will have a potential application as a flocculant in wastewater treatment and as a new paper retention aid in papermaking.

Acknowledgements

The authors thank the project supported by Hunan Provincial Natural Science Foundation of China (project No.06JJ2067).

References

[1] Hecht S.: Functionalizing the interior of dendrimers: Synthetic challenges and applications. Journal of Polymer Science Part A: Polymer Chemistry, **41**, 1047–1058 (2003).
DOI: 10.1002/pola.10643

[2] Tomalia D. A.: Birth of a new macromolecular architecture: Dendrimers as quantized building blocks for nanoscale synthetic polymer chemistry. Progress in Polymer Science, **30**, 294–324 (2005).
DOI: 10.1016/j.progpolymsci.2005.01.007

[3] Vögt1e F., Gestermann R., Hesse H., Schwierz H., Windisch B.: Functional dendrimers. Progress in Polymer Science, **25**, 987–1041 (2000).
DOI: 10.1016/S0079-6700(00)00017-4

[4] Blaak R., Lehmann S., Likos C. N.: Charge-induced conformational changes of dendrimers. Macromolecules, **41**, 4452–4458 (2008).
DOI: 10.1021/ma800283z

[5] Hendricks T. R., Dams E. E., Wensing S. T., Lee I.: Effects of catalyst introduction methods using PAMAM dendrimers on selective electroless nickel deposition on polyelectrolyte multilayers. Langmuir, **23**, 7404–7410 (2007).
DOI: 10.1021/la7007232

[6] Takahashi T., Kono K., Itoh T., Emi N., Takagishi T.: Synthesis of novel cationic lipids having polyamidoamine dendrons and their transfection activity. Bioconjugate Chemistry, **14**, 764–773 (2003).
DOI: 10.1021/bc025663f

[7] Wang S., Hong J. W., Bazan G. C.: Synthesis of cationic water-soluble light-harvesting dendrimers. Organic Letters, **7**, 1907–1910 (2005).
DOI: 10.1021/ol047674p

[8] Mckee M. L.: Density functional theory study of anionic and neutral per-substituted 12-vertex boron cage systems, $B_{12}X_{12}^{n-}$ (n: 2, 1, 0). Inorganic Chemistry, **42**, 1299–1305 (2002).
DOI: 10.1021/ic011021c

[9] Fochi F., Jacopozzi P., Wegelius E., Rissanen K., Cozzini P., Marastoni E., Fisicaro E., Manini P., Fokkens R., Dalcanale E.: Self-sssembly and anion encapsulation properties of cavitand-based coordination cages. Journal of the American Chemical Society, **123**, 7539–7552 (2001).
DOI: 10.1021/ja0103492

[10] Kojima C., Kono K., Maruyama K., Takagishi T.: Synthesis of polyamidoamine dendrimers having poly(ethylene-glycol) grafts and their ability to encapsulate anticancer drugs. Bioconjugate Chemistry, **11**, 910–917 (2000).
DOI: 10.1021/bc0000583

[11] Kim T., Seo H. J., Choi J. S., Jang H. S., Baek J. U, Kim K., Park J. S.: PAMAM-PEG-PAMAM: Novel triblock copolymer as a biocompatible and efficient gene delivery carrier. Biomacromolecules, **5**, 2487–2492 (2004).
DOI: 10.1021/bm049563j

[12] Wang F., Bronich T. K., Kabanov A. V., Rauh R. D., Roovers J.: Synthesis and evaluation of a star amphiphilic block copolymer from poly(ε-caprolactone) and poly(ethylene glycol) as a potential drug delivery darrier. Bioconjugate Chemistry, **16**, 397–405 (2005).
DOI: 10.1021/bc049784m

[13] Allen L., Polverari M.: Dendrimers: A new retention aid for newsprint, mechanical printing grades, and board. Nordic Pulp and Paper Research Journal, **15**, 407–416 (2000).
DOI: 10.3183/NPPRJ-2000-15-05-p407-415

[14] Zhou G. Z., Tan H. M., Luo Y. J., Zhang X., Liao S. Q.: New method of TNT red-water treatment. Industrial Water Treatment, **6**, 14–16 (2002).

[15] Mavredaki E., Neofotistou E., Demadis K. D.: Inhibition and dissolution as dual mitigation approaches for colloidal silica fouling and deposition in process water systems: Functional synergies. Industrial and Engineering Chemistry Research, **44**, 7019–7026 (2005).
DOI: 10.1021/ie0501982

[16] Demadis K. D., Neofotistou E.: Synergistic effects of combinations of cationic polyaminoamide dendrimers/anionic polyelectrolytes on amorphous silica formation: A bioinspired approach. Chemistry of Materials, **19**, 581–587 (2007).
DOI: 10.1021/cm062370d

[17] Demadis K. D., Neofotistou E., Mavredaki E., Tsiknakis M., Sarigiannidou E-M., Katarachia S. D.: Inorganic foulants in membrane systems: chemical control strategies and the contribution of 'green chemistry'. Desalination, **179**, 281–295 (2005).
DOI: 10.1016/j.desal.2004.11.074

[18] Peng X. C., Peng X. H., Zhao J. Q., Lin Y. W., Wang Q. T.: Preparation and characterization of novel PAMAM 4.0G-DMC cationic dendrimer and its flocculating and dewatering performances. Petrochemical Technology, **34**, 986–989 (2005).

[19] Peng X. C., Peng X. H., Zhao J. Q.: Preparation and characterization of a polyoxyethlene-macromonomer modified polyamidoamine dendrimers. Nanoscience, **1**, 146–149 (2005).

[20] Yamakawa H.: Modern theory of polymer solution. Harper and Row, New York (1971).

[21] Long F., Fan Y., Ding H. J., Jia X. R., Li M. Q.: The intrinsic viscosity of polyamidoamine dendrimer. Chemical Journal of Chinese Universities, **20**, 1628–1632 (1999).

eXPRESS Polymer Letters Vol.3, No.8 (2009) 518–524
Available online at www.expresspolymlett.com
DOI: 10.3144/expresspolymlett.2009.64

Effect of sepiolite on the physical properties and swelling behavior of rifampicin-loaded nanocomposite hydrogels

A. L. Viçosa[1,2], *A. C. O. Gomes*[1], *B. G. Soares*[1], *C. M. Paranhos*[3*]

[1]Instituto de Macromoléculas, Universidade Federal do Rio de Janeiro, Centro de Tecnologia, Av. Horacio Macedo 2030, Bloco J, Ilha do Fundão, 21945-598, Rio de Janeiro – RJ, Brazil
[2]Laboratório de Tecnologia Farmacêutica, Complexo Tecnológico de Medicamentos, Fundação Oswaldo Cruz, Av. Comandante Guaranys 447, Jacarepagua, 21041-250, Rio de Janeiro – RJ, Brazil
[3]Laboratório de Permeação e Sorção, Departamento de Engenharia de Materiais, Universidade Federal de São Carlos, Rod. Washington Luiz, km 235, 13565-905, São Carlos – SP, Brazil

Received 28 March 2009; accepted in revised form 25 May 2009

Abstract. Nanocomposite hydrogels based on poly(vinyl alcohol) – PVA and sepiolite have been prepared and their potential for drug delivery systems has been assessed by taking rifampicin as model drug. The nanocomposite hydrogels were characterized by WAXS and DSC and the swelling behavior and structural stability were evaluated. The effect of the presence of rifampicin, sepiolite and simultaneous rifampicin-sepiolite on the structure and swelling of the hydrogels was investigated. The swelling data were analyzed in order to evaluate the diffusion mechanisms of water. The results indicate that both rifampicin and sepiolite cause important modifications on microstructure of the PVA matrix, leading to changes on swelling and diffusional behavior.

Keywords: *polymer gels, poly(vinyl alcohol), hydrogel, nanocomposite, rifampicin*

1. Introduction

Recent epidemiologic data report a strong growing up of tuberculosis in several countries. World Health Organization (WHO) indicates that about one third of world population is infected by *Mycobacterium tuberculosis* [1]. Among several reasons, the blowing up of AIDS cases, low nutritional and immunologic level of several parts of world, bacterial resistance caused by partial treatment and the inadequate bioavailability of the current pharmaceutical forms play an important role on this neglected epidemic [2].

In order to minimize the bacterial resistance and enhance the adhesion to the treatment by the patients, the Center of Disease Control (CDC), the International Union Against Tuberculosis and Lung Disease (IUATLD) and WHO have recommended the use of fixed dose combination (FDC). Tuberculosis treatment preconized by WHO involves the use of rifampicin, isoniazid, pirazinamide and ethambutol for a period of 6 months. However, FDC's are effective in tuberculosis treatment if correctly dosed in blood plasma [3]. Rifampicin is a class II drug (low solubility and high permeability) of biopharmaceutics classification system (BCS) and is well known for its poor solubility in water and bioavailability problems [4]. Figure 1 shows the chemical structure of rifampicin.

In order to enhance the solubility and bioavailability of poorly water-soluble hydrophobic drugs as rifampicin, several methods have been employed: decreasing of particle size and the crystallinity of

*Corresponding author, e-mail: caiomp.dema@gmail.com

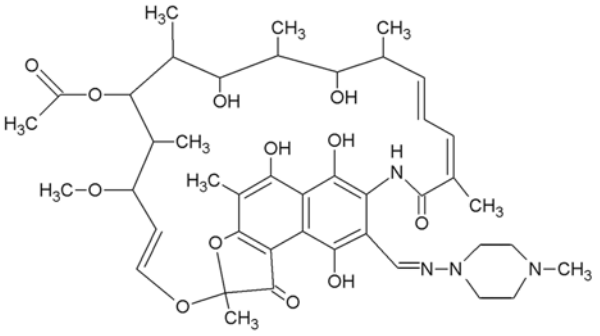

Figure 1. Chemical structure of rifampicin

the drug and/or using a carrier with high specific surface area. The adsorption of the drug onto a high surface area carrier is an interesting technique to modify the dissolution profile of rifampicin. It is well known that inorganic species can be used in order to improve the dissolution rate of drugs. Monkhouse and Lach (1972) were the first to report the use of silica in order to improve the dissolution rate of several drugs, including chloramphenicol, aspirin and indomethacin [5, 6]. It was observed that smectite increases the dissolution rate of non-ionic drugs due the hydrophilic nature of the clay [7, 8]. Recently, Aguzzi and co-authors published a comprehensive review of the use of clay minerals as drug delivery systems [9].

We have utilized natural sepiolite in order to improve the dissolution rate of rifampicin. Sepiolite is a fibrous clay mineral with fine microporous channels of dimensions 0.37×1.06 nm running parallel to the length of fibers. Typically, sepiolite shows an average size of 800×25×4 nm, resulting in a material with an external surface area of the same order of magnitude as the area of macroporous. The structure of sepiolite, in some aspects, is similar to zeolites [10]. The presence of structural tunnels and blocks together with the fine particle size and the fibrous nature explain the high specific surface area present in sepiolite. Nevertheless, the use of sepiolite in order to improve the dissolution rate of poorly water-soluble drugs is still indaquately studied. However, changes on the microstructure of the polymeric matrix due the simultaneous presence of the clay and the drug must be predicted in order to avoid misinterpretation of the obtained results.

In the present investigation hydrogels based on poly(vinyl alcohol) (PVA) and sepiolite were prepared and loaded with rifampicin. The effect of the presence of sepiolite and rifampicin on the physical properties and swelling behavior of the hydrogels was studied.

2. Materials and methods

2.1. Materials

Poly(vinyl alcohol), degree of hydrolysis 99%, M_w = 120 000, was purchased by Sigma. Natural sepiolite was purchased by Fluka. Rifampicin was kindly supplied by Najiecun Pharmaceutical, China. All materials were used without further purification.

2.2. Preparation of hydrogels

An appropriate amount of clay was stirred in distilled water at room temperature for 1 h, followed by mechanical stirring during 30 min. To the resulting suspension, 5 g of PVA and 0.025 g of sodium benzoate (a multi-purpose preservative) were added and the suspension was heated under reflux at 95°C for 4 h under stirring. Rifampicin was previously dispersed in polysorbate (Tween 80 – Vetec). Recently, Mehta and collaborators reported the use of Tween 80 in order to increase the solubility of rifampicin in water [11]. After the reflux time, PVA solution was cooled until 40°C. Then, rifampicin was added and the final suspension was stirred with an Ultra Turrax homogenizer (IKA) during 10 min at 6500 rpm. Table 1 shows the sample designation of the obtained hydrogels. The suspension was poured in Petri dishes and maintained in a refrigerator at 8–10°C for 24 h in order to form stable hydrogels.

Table 1. Composition and designation of nanocomposite hydrogels

Sample designation	PVA [wt%]	Sepiolite [wt%]	Rifampicin
PVA	100	–	–
PVAR	100	–	150 mg
PVAS1	99	1	–
PVAS5	95	5	–
PVAS1R	99	1	150 mg
PVAS5R	95	5	150 mg

2.3. Swelling behavior

The hydrogels matrices were allowed to swell in pH 7.4 phosphate saline buffer solution (PBS) at 30°C for 24 h. At predetermined time intervals, the

weight of the hydrogels was checked in an electronic balance after wiping the hydrogel surface with a filter paper. The swelling ratio, *S*, was then calculated from Equation (1):

$$S = \frac{W_s - W_d}{W_d} \quad (1)$$

where W_s and W_d are the swollen and the dry weight of the hydrogel, respectively. The average standard deviation was set in 10%.

2.4. Samples characterization

Wide-angle X-ray scattering (WAXS) was performed in a Rigaku Miniflex in a 2θ range of 2–40° at room temperature, operating under a CuK_α radiation (λ = 1.5405 Å). Thermal analyses were assessed by a Perkin-Elmer DSC-7. All measurements were made at a scan rate of 10°C/min, in the temperature range of 40 to 250°C, under continuous nitrogen gas flow. The structural stability of the samples was evaluated spectrometrically. The amount of PVA released from the hydrogels samples was determined by immersing small pieces of the hydrogels in distilled/deionized water. Then, after pre-established times (1, 2, 8 and 24 h) an aliquot of 10 ml of the releasing solution was removed and replaced with the same amount of fresh distilled water. The aliquot was then treated with a 0.65 M boric acid solution and a 0.05 M I_2/0.15 M KI solution. It is well known that PVA and boric acid/iodine complexes, resulting in a green complex [12]. The absorbance of visible light at 670 nm was then measured in a Cary 100 (Varian) UV-Visible spectrophotometer.

3. Results and discussion

The WAXS patterns of the hydrogels are shown in Figure 2. The strong diffraction peak observed at 2θ = 7.5° for sepiolite is related to the (110) crystallographic plane. This plane corresponds to the zeolitic pore inside the sepiolite needles that cannot be modified by chemical modifications or preparation from solution [13]. Unfortunately, it is not possible to calculate the degree of crystallinity of the samples containing sepiolite, since the 2θ = 19.75° and 20.65° (060 and 131 reflections, respectively [14]) of sepiolite overlaps the 101 and $10\bar{1}$ reflections of PVA (2θ = 19.5 and 20.1°, respectively). Therefore, WAXS results will be used to evaluate possible changes on the crystalline structure of PVA.

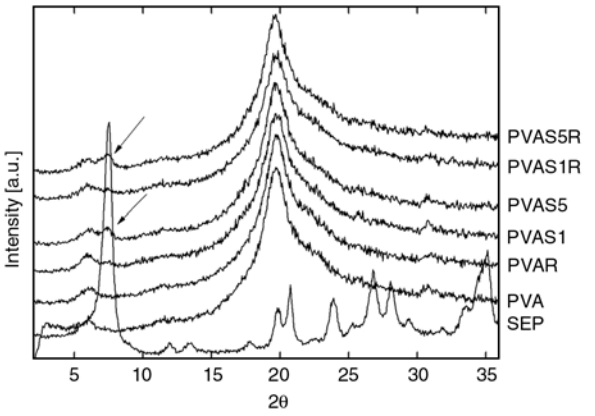

Figure 2. WAXS patterns of nanocomposite hydrogels. The curves are vertically offset for clarity.

At first glance, the presence of rifampicin and sepiolite do not cause significant change on the monoclinic crystal of PVA. The strong reflection at 2θ = 19.6° (plane 101 of PVA) does not show significant shifts with the presence of both sepiolite and rifampicin, indicating that no preferential crystalline orientation or constriction was detected. Despite the several reflections peaks observed in pure rifampicin (not shown), WAXS results of the PVAR sample do not show any evidence of crystalline reflections associated to rifampicin. Thus, the content of rifampicin added in the PVA matrix was not able to cause significant changes on the monoclinic crystal of PVA. It is known that the presence of lamella-type phyllosilicates, as montmorillonite, causes significant changes on the crystalline structure of several polymers [15, 16]. This fact is mainly caused by the confining crystallization environment provided by the clay platelets, On the other hand, the high aspect ratio of sepiolite fibers leads to a less confinement effect, resulting in a stable PVA crystallite. This behavior is consistent with observed to the samples PVAS1 and PVAS1R. However, for the samples containing 5% of sepiolite (PVAS5 and PVAS5R) it is possible to observe a relative small reflection corresponding to the 110 plane of sepiolite. These features indicate that higher content of sepiolite leads to the agglomeration of the sepiolite fibers. Similar behavior was reported by Chen and co-authors to sepiolite/polyurethane nanocomposites [17].

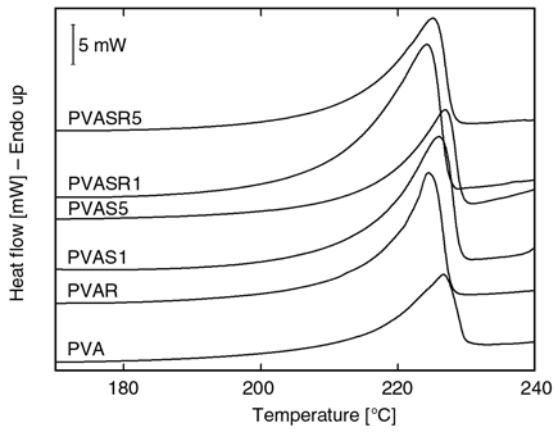

Figure 3. DSC curves of nanocomposite hydrogels. The curves are vertically offset for clarity.

In order to evaluate the crystalline nature of the hydrogels, the influence of sepiolite and rifampicin on the crystallinity of PVA matrix was also evaluated by DSC. Figure 3 presents the DSC heating curves and the Table 2 summarizes the crystalline melting parameters for the PVA-based samples. Pure PVA exhibits an endothermic peak at 227°C, corresponding to the crystalline melting point (T_m) of PVA. The presence of rifampicin causes a slight shifting of the melting peak of PVA to lower temperatures. This effect is attributed to the interactions between PVA and rifampicin and its large molecular size (M_w = 823). PVA hydroxyl groups can interact via hydrogen bonding with rifampicin. As can be seen in Figure 1 rifampicin has a lot of functional groups that can create hydrogen bonding [18]. These interactions together the large molecular size cause some disruption of the lamellar arrangement of the crystalline domains of PVA, consequently leading to lower T_m [19]. Table 2 shows that ΔT and fwhm (full-width half-maximum) decrease by the addition of rifampicin on PVA matrix, indicating simultaneous increases in the rate of melting and the average crystalline size. Rifampicin shows its melting followed by recrystallization and decomposition in the range of 180–223°C and 247–266°C, respectively [20]. Unfortunately, the melting temperature of PVA is located at the same range. Nevertheless, no evidence of both processes of rifampicin was observed in DSC curves. It seems that rifampicin undergoes an amorphization process during the preparation of the hydrogels. Schierholz has reported a similar effect in shunts based on poly(dimethylsiloxane) loaded with 0.5–10% (w/w) of rifampicin [21]. Therefore, rifampicin acts as nucleating agent for PVA, resulting in less ordered crystalline domains and higher degree of crystallinity when compared to the pure PVA. The same behavior is observed to PVAS1R and PVAS5R, confirming the strong interaction between rifampicin and PVA. However, the monoclinic crystal of PVA does not undergo significant changes as can be seen in WAXS patterns. As a fact, the microstructure of PVA hydrogels is formed by a bicontinuous structure with a PVA-rich phase (crystalline domains) and a PVA-poor phase (amorphous domains) [22]. Thus, the DSC results reflect the changes on the crystalline domains which correspond to the PVA-rich phase. In concordance with the WAXS results, the presence of sepiolite does not cause changes in T_m of the samples PVAS1 and PVAS5.

Table 2. Thermal parameters of nanocomposite hydrogels obtained by DSC*

Sample	T_m [°C]	T_{onset} [°C]	ΔT[a]	fwhm[b]	X_c [%][c]
PVA	226.6	215.0	11.6	7.8	37.3
PVAR	224.2	218.1	6.1	6.7	43.4
PVAS1	226.0	215.0	11.0	8.0	36.3
PVAS5	226.8	217.4	9.4	7.2	51.4
PVAS1R	224.2	210.8	13.4	9.3	44.6
PVAS5R	224.8	213.5	11.3	8.6	42.2

*The experimental errors associated with the thermal analysis experiments are ± 0.8°C and ±1.5% for T_m and X_c, respectively.
[a]$\Delta T = T_m - T_{onset}$
[b]fwhm = full width at half maximum
[c]X_c is calculated by the ratio of $\Delta H/\Delta H_m^\circ$, where ΔH_m° is the melting enthalpy of 100% crystalline PVA, i.e. 150 J/g [20].

The dispersion state of sepiolite can be evaluated by changes on degree of crystallinity (X_c) of the samples PVAS1 and PVAS5. The highly dispersed state of sepiolite fibers in PVAS1 can be confirmed, since no changes occur in the crystalline parameters listed in Table 2 when compared with pure PVA. However, the presence of 5% of sepiolite has a nucleating effect on the PVA matrix. Similar results were recently reported by Ma and collaborators for polypropylene/sepiolite nanocomposites [23]. The thermal parameters of PVAS1R and PVAS5R samples reveal a clear evidence that rifampicin plays a key role in the formation of the crystalline domains of PVA. Even with increasing amounts of sepiolite, the crystalline parameters of the samples tend to follow the behavior showed to PVAR sample. It is important to note that the addition of rifampicin was realized after the incorporation of the clay, as can be seen in Section 2.2.

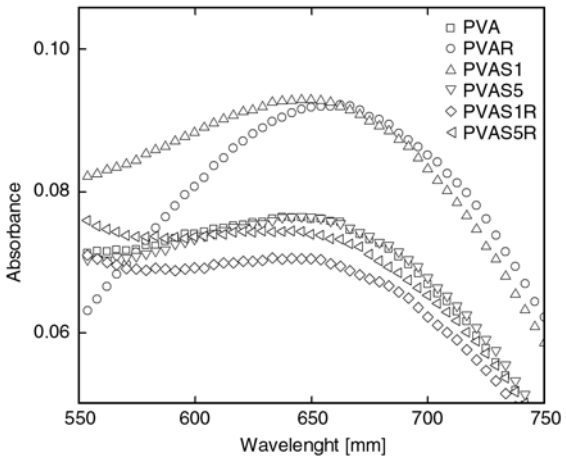

Figure 4. UV-Vis spectra of nanocomposite hydrogels after 24 h immersed in PBS

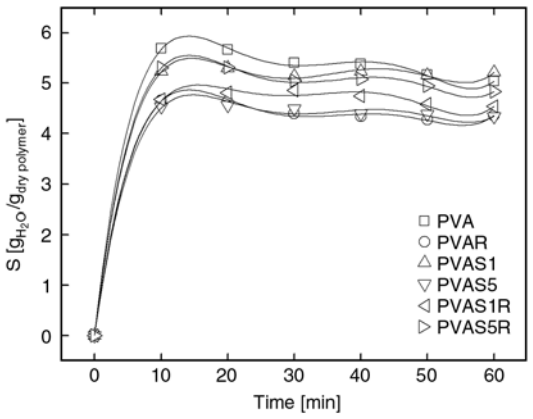

Figure 5. Swelling ratio of nanocomposite hydrogels in pH 7.4 at 30°C

Therefore, the presence of rifampicin affects directly the final crystalline domains of PVA.

The results of the structural stability of the PVA matrix after 24 h immersed in PBS were evaluated spectrometrically, as can be seen in Figure 4. It is possible to note that all formulations containing sepiolite contribute to stabilize the residual PVA chains, except for PVAS1 sample. The presence of rifampicin results in an increasing number of PVA chains that does not contribute to form new crystallites, resulting in less ordered crystallites. This is consistent with the DSC results. It seems that the presence of sepiolite tends to prevent the diffusion of the residual PVA chains through the hydrogel. Since the presence of sepiolite does not impede the crystalline disorder caused by rifampicin, it is reasonable to expect that residual PVA chains are readily linked with sepiolite fibers. The case of PVAS1 sample is quite different, presenting the same amount of residual PVA chains observed to PVAR. This trend is consistent with a highly dispersed state of sepiolite. Since the average distance between clay fibers is considerable, it is expected that the intensity of the interactions between PVA and sepiolite is diminished; therefore the presence of small amounts of sepiolite do not contribute to retain the residual PVA chains.

Swelling behavior is an important parameter to characterize the hydrogels because it has a significant influence on the process of controlled release of drugs [24]. The swelling ratios as a function of the time for the hydrogels in PBS are shown in Figure 5. It is possible to note that the presence of sepiolite causes a decrease in the swelling capacities of the hydrogels when compared to pure PVA. The highly dispersed clay causes a decrease in available free volume of the PVA matrix, leading to lower swelling ratio. In the case of PVAS5, increase on X_c also contributes to diminish the available free volume for water diffusion. PVAR shows similar low degree of swelling when compared to PVAS5. However, PVAR has lowest X_c observed between the samples. This fact indicates that the presence of amorphized rifampicin leads to an obstruction effect, therefore reducing the number of pores available for water diffusion into the matrix. This effect is simultaneous with the increase of X_c in PVAR samples.

The dynamics of water sorption process was studied by monitoring the water imbibed by the hydrogels using Equation (2) [25]:

$$\frac{W_t}{W_\infty} = Kt^n \tag{2}$$

where W_t and W_∞ is the weight of swollen hydrogel at time t and at infinitely equilibrium swollen state, respectively, K is a characteristic constant and n is a characteristic exponent of the mode transport of the water. According to the classification of the diffusion mechanism, $n = 0.5$ indicates a quasi-Fickian diffusion; for $1/2 < n < 1$ anomalous, non-Fickian diffusion model operates and for $n = 1$ occurs a non-Fickian case II mechanism [25]. Table 3 summarizes the diffusion parameters of the PVA-based hydrogels. The obtained data indicate that the swelling transport mechanism is consistent with a quasi-Fickian process. This feature reveals a simultaneous contribution of the random mobility of water molecules into the PVA matrix and the solva-

Table 3. Transport properties of nanocomposite hydrogels

Sample	Diffusion exponent (n)	Kinetic constant (K)	Correlation coefficient (r^2)	Diffusion coefficient [cm^2/s]·10^8
PVA	0.52	0.040	0.996	1.48
PVAR	0.47	0.052	0.994	1.75
PVAS1	0.51	0.330	0.996	1.25
PVAS5	0.46	0.420	0.993	4.79
PVAS1R	0.51	0.340	0.994	2.03
PVAS5R	0.48	2.920	0.996	2.34

tion of the high hydrophilic groups of PVA chains. The following model (Equation (3)) was used to calculate the diffusion coefficient, D, for $W_t/W_\infty \leq 0.8$ [25]:

$$\frac{W_t}{W_\infty} = 4\left(\frac{Dt}{\pi l}\right)^{0.5} \quad (3)$$

where l is the initial thickness of the hydrogel. The calculated diffusion coefficients are shown in Table 3. Since the degree of crystallinity of PVAR is higher than pure PVA, increase of diffusion coefficient of PVAR can be evaluated in terms of the interactions between rifampicin and PVA. The hydrophobic nature of rifampicin contributes to impede the complete solvation of the hydrophilic groups of PVA by water molecules. Besides this fact, hydrogen bonding between rifampicin and PVA leads to a hindered effect to the water molecules; therefore, the migration of water is more pronounced in the polymeric matrix, resulting in higher diffusion coefficient.

The effect of the dispersion state of sepiolite on the PVA matrix could be confirmed in PVAS1 sample. The obstruction effect caused by the highly dispersed clay fibers contribute to a slow-mode migration of the water molecules, leading to a decrease of diffusion coefficient. As a fact, PVAS1 shows lower diffusion coefficient and the same X_c of pure PVA. An interesting result is observed to PVAS5. Decreasing diffusion coefficient is expected with both higher clay content and X_c. Nevertheless, 5% of sepiolite leads to highest diffusion coefficient between the samples. Increasing content of sepiolite leads to aggregation of the clay fibers, as observed in WAXS patterns. However, the aggregation state contributes to form preferential water channels by the zeolite-like porous of sepiolite, resulting in an increasing diffusion coefficient when compared to PVA. Zhang and collaborators have found a similar behavior in poly(acrylic acid-*co*-acrylamide)/sepiolite nanocomposite hydrogels [26]. In the case of PVAS1R and PVAS5R samples, it seems that the amorphized rifampicin tends to block the access of water molecules to sepiolite pores, leading to a decrease of diffusion coefficient. In order to evaluate the use of the nanocomposite hydrogels for drug release systems, it is necessary a complete understanding of how the presence of both rifampicin and sepiolite changes the swelling capacities and crystallinity of the hydrogels.

4. Conclusions

Nanocomposite hydrogels based on poly(vinyl alcohol) and sepiolite with loaded-rifampicin was successfully prepared. High amounts of sepiolite lead to an increasing degree of crystallinity and to a decrease in swelling capacities. However, the aggregation state of the clay fibers favors the formation of water channels, resulting in higher diffusion coefficient of water. High degree of dispersion was achieved with 1% (w/w) of sepiolite. This fact contributes to diminish the swelling capacity and the water migration into the PVA matrix. The presence of amorphized rifampicin contributes to decrease diffusion coefficient of water and changes the nature of the crystalline domains of PVA. The overall changes on swelling behavior and crystallinity of the nanocomposite hydrogels must be understood in order to evaluate the drug release profile of rifampicin under *in vitro* and *in vivo* conditions.

References

[1] World Health Organization: Global tubercolosis control: Epidemiology, strategy, financing. WHO, Geneva (2009).

[2] Sen H., Jindal K. C., Deo K. D., Gandhi K. T.: An improved process for preparation of four-drug antitubercular fixed dose combination. WO 200287547 A1, India (2002).

[3] International Union Against Tuberculosis and Lung Disease: Quality assurance: Protocol for assessing the rifampicin bioavailability of combined formulations in healthy volunteers. The International Journal of Tuberculosis and Lung Disease, **3**, s284–s285 (1999).

[4] Panchagnula R., Agrawal S.: Biopharmaceutic and pharmacokinetic aspects of variable bioavailability of rifampicin. International Journal of Pharmaceutics, **271**, 1–4 (2004).
DOI: 10.1016/j.ijpharm.2003.11.031

[5] Monkhouse D. C., Lach J. L.: Use of adsorbents in enhancement of drug dissolution I. Journal of Pharmaceutical Sciences, **61**, 1430–1435 (1972).
DOI: 10.1002/jps.2600610917

[6] Monkhouse D. C., Lach J. L.: Use of adsorbents in enhancement of drug dissolution II. Journal of Pharmaceutical Sciences, **61**, 1435–1441 (1972).
DOI: 10.1002/jps.2600610918

[7] Takahashi T., Yamaguchi M.: Host-guest interaction between swelling clay minerals and poorly water-soluble drugs. 1: Complex formation between a swelling clay mineral and griseofulvin. Journal of Inclusion Phenomena and Macrocyclic Chemistry, **10**, 283–297 (1991).
DOI: 10.1007/BF01066211

[8] Takahashi T., Yamaguchi M.: Host-guest interactions between swelling clay minerals and poorly water-soluble drugs: II. Solubilization of griseofulvin by complex formation with a swelling clay mineral. Journal of Colloid and Interface Science, **146**, 556–564 (1991).
DOI: 10.1016/0021-9797(91)90219-X

[9] Aguzzi C., Cerezo P., Viseras C., Caramella C.: Use of clays as drug delivery systems: Possibilities and limitations. Applied Clay Science, **36**, 22–36 (2007).
DOI: 10.1016/j.clay.2006.06.015

[10] Santos P. S.: Clay Technology, vol 1. (in Portuguese). Edgard Blücher, São Paulo (1975).

[11] Mehta S. K., Kaur G., Bhasin K. K.: Analysis of Tween based microemulsion in the presence of TB drug rifampicin. Colloids and Surfaces B: Biointerfaces, **60**, 95–104 (2007).
DOI: 10.1016/j.colsurfb.2007.06.012

[12] Joshi D. P., Lan-Chun-Fung Y. L., Pritchard J. G.: Determination of poly(vinyl alcohol) via its complex with boric acid and iodine. Analytica Chimica Acta, **104**, 153–160 (1979).
DOI: 10.1016/S0003-2670(01)83825-3

[13] Tartaglione G., Tabuani D., Camino G.: Thermal and morphological characterisation of organically modified sepiolite. Microporous and Mesoporous Materials, **107**, 161–168 (2008).
DOI: 10.1016/j.micromeso.2007.04.020

[14] Brindley G. W.: X-ray and electron diffraction data for sepiolite. The American Mineralogist, **44**, 495–500 (1959).

[15] Sharma S. K., Nayak S. K.: Surface modified clay/polypropylene (PP) nanocomposite: Effect on physico-mechanical, thermal and morphological properties. Polymer Degradation and Stability, **94**, 132–138 (2009).
DOI: 10.1016/j.polymdegradstab.2008.09.004

[16] Yebra-Rodríguez A., Alvarez-Lhoret P., Cardell C., Rodríguez-Navarro A. B.: Crystalline properties of injection molded polyamide-6 and polyamide-6/montmorillonite nanocomposites. Applied Clay Science, **43**, 91–97 (2009).
DOI: 10.1016/j.clay.2008.07.010

[17] Chen H., Zheng M., Sun H., Jia Q.: Characterization and properties of sepiolite/polyurethane nanocomposites. Materials Science and Engineering: A, **445–446**, 725–730 (2007).
DOI: 10.1016/j.msea.2006.10.008

[18] Adachi T., Isobe E.: Fundamental characteristics of synthetic adsorbents intended for industrial chromatographic separations. Journal of Chromatography A, **1036**, 33–44 (2004).
DOI: 10.1016/j.chroma.2003.09.018

[19] Ricciardi R., Auriemma F., De Rosa C.: Structure and properties of poly(vinyl alcohol) hydrogels obtained by freeze/thaw techniques. Macromolecular Symposia, **222**, 49–64 (2005).
DOI: 10.1002/masy.200550405

[20] Agrawal S., Ashokraj Y., Bharatam P. V., Pillai O., Panchagnula R.: Solid-state characterization of rifampicin samples and its biopharmaceutic relevance. European Journal of Pharmaceutical Sciences, **22**, 127–144 (2004).
DOI: 10.1016/j.ejps.2004.02.011

[21] Schierholz J. M.: Physico-chemical properties of a rifampicin-releasing polydimethyl-siloxane shunt. Biomaterials, **18**, 635–641 (1997).
DOI: 10.1016/S0142-9612(96)00071-3

[22] Ricciardi R., Mangiapia G., Lo Celso F., Paduano L., Triolo R., Auriemma F., De Rosa C., Lauprêtre F.: Structural organization of poly(vinyl alcohol) hydrogels obtained by freezing and thawing techniques: A SANS study. Chemistry of Materials, **17**, 1183–1189 (2005).
DOI: 10.1021/cm048632y

[23] Ma J., Bilotti E., Peijs T., Darr J. A.: Preparation of polypropylene/sepiolite nanocomposites using supercritical CO_2 assisted mixing. European Polymer Journal, **43**, 4931–4939 (2007).
DOI: 10.1016/j.eurpolymj.2007.09.010

[24] Hoffman A. S.: Hydrogels for biomedical applications. Advanced Drug Delivery Reviews, **54**, 3–12 (2002).
DOI: 10.1016/S0169-409X(01)00239-3

[25] Crank J.: Mathematics of diffusion. Oxford University Press, Oxford (1975).

[26] Zhang F., Guo Z., Gao H., Li Y., Ren L., Shi L., Wang L.: Synthesis and properties of sepiolite/poly(acrylic acid-co-acrylamide) nanocomposites. Polymer Bulletin, **55**, 419–428 (2005).
DOI: 10.1007/s00289-005-0458-2

eXPRESS Polymer Letters Vol.3, No.8 (2009) 525–532
Available online at www.expresspolymlett.com
DOI: 10.3144/expresspolymlett.2009.65

Polyamide 6 single polymer composites

D. Bhattacharyya[*], *P. Maitrot, S. Fakirov*

Centre for Advanced Composite Materials, Department of Mechanical Engineering, The University of Auckland, Private Bag 92019, Auckland, New Zealand

Received 8 January 2009; accepted in revised form 4 June 2009

Abstract. Combining the two basic techniques used for the preparation of single polymer composites (SPCs), hot compaction and film stacking, a polyamide 6 (PA 6) single polymer composite was manufactured. The starting materials were PA 6 high tenacity yarn (reinforcement) and PA 6 film prepared via melt quenching (matrix), both expected to be the two principal polymorphic modifications of PA 6 and thus differing in their melting temperatures. The prepared single polymer composite is characterized by a layered structure and shows superior mechanical properties due to the good wetting – tensile modulus is improved by 200% and the ultimate tensile strength – by 300–400% as compared to the isotropic matrix film. Improvement of the interfacial adhesion via transreactions promoted by Sb_2O_3 as a catalyst was also undertaken.

Keywords: *polymer composites, single polymer composites, polyamide 6, mechanical properties*

1. Introduction

The environmental impact of the steadily increasing use of plastic materials requires the development of new combinations of materials, possibly with improved properties but with reduced environmental harm. The creation of single polymer composites (SPCs) seems to be an alternative in this respect because they do not contain mineral fillers and are characterized by improved adhesion quality between the matrix and the reinforcement.

Formulated for the first time by Capiati and Porter [1], this type of material was further developed by Ward and his group [2–8] including patenting and commercialization of the 'hot compaction' technique [2]. This method used an assembly of highly oriented polymer fibers or tapes subjected to heating to a critical temperature, while being held together under pressure such that a thin volume of material on the surface of each oriented element is 'selectively melted' creating a matrix [9]. The uniqueness of the hot compaction technique is the use of one constituent only.

In contrast to the foregoing approach, the most frequently used technique is film stacking where the film is generally chosen to have a lower melting temperature (T_m) compared to the orientated fibers [10–16]. A characteristic feature of this technique [10–19] is that the two constituents of the same polymer are used as starting materials for manufacturing of SPCs. Recently, the authors have explored both of these approaches for preparation of SPCs based on poly(ethylene terephthalate) (PET) using a new type of reinforcement, namely, PET nanofibrils, by means of techniques developed earlier [20, 21] for nanofibrillar composites (NFCs). In the case of two-constituent SPCs, layers of PET nanofibrils with diameters between 50 and 150 nm were sandwiched between PET film with lower T_m and thereafter compression moulded [22]. The improvements in both, the tensile modulus (E) and the

*Corresponding author, e-mail: d.bhattacharyya@auckland.ac.nz

ultimate tensile strength (σ_{uts}) were around 65% and for some specimens up to 100%, thus approaching the improvement values of the PET SPCs prepared by Hine and Ward [6] by means of the hot compaction method.

The same nanofibrils were used for the preparation of nanofibrillar SPCs applying the one-constituent approach and the improvements of E, σ_{uts} and yield strength were all around 300% [23]. One specimen even showed the maximum modulus value of 10.6 GPa, which was very close to that of PET/glass fibre (60/40 wt%) composites reaching a modulus of around 11 GPa [6].

In addition to these studies with nanofibrils, the two-constituent approach was applied to polyamide 66 (PA 66) for the manufacture of SPCs using it as the matrix and as the reinforcement with rather different melting temperatures. They were thought to be the two well known polymorphic modifications of PA 66 [24]. In the present paper, the same study is extended to polyamide 6 (PA 6), where again an attempt was made to use the extremely high ability of formation of polymorphic crystalline modifications [25]. For example, PA 6 quenched from its melt, crystallizes in the γ-modification, while at higher temperatures and/or during drawing it undergoes crystallization in the α-modification with the higher-melting temperature. This polymorphic transition takes place in such a smooth way that the existence of the γ-modification cannot be detected during the heating in the differential scanning calorimeter. Only after applying a chemical cross-linking in the amorphous areas before scanning Fakirov and Avramova [26] succeeded to prevent the recrystallization process and thus determined the equilibrium melting temperature (T_m^0) of the γ-modification of PA 6 amounting to T_m^0 = 208°C (against T_m^0 = 278°C of the α-modification) [26].

An additional reason for performing this study is the fact that, to the best of the authors' knowledge, there has been no report on single polymer composites based on PA 6.

2. Experimental details

2.1. Materials and sample preparation

PA 6 commercial type 2650 from Hoechst, Germany, in the form of pellets was used as the matrix. Commercial UV stabilized high tenacity PA 6 yarn of the code 222 and, according to Firestone, Nashville, Tennessee, USA, of 1848 dtex and 136 filaments played the role of reinforcement. In order to get reinforcement with a higher T_m, the yarn was subjected to annealing in vacuum for 3 h at 150°C.

The matrix was prepared in the form of a thin film (thickness of 150 μm) by means of compression moulding at 260°C for 5 min and at a pressure of about 35 MPa followed by quenching in ice water together with the covering of Teflon films. Another film was prepared using slow cooling to room temperature. The reinforcing yarn of continuous filaments was wound onto a metal plate using a lathe. Each of the two yarn layers was sandwiched between two matrix films and subjected to compression molding at 200°C for 5 min under a pressure of ~15 MPa. The pressure was maintained during cooling to room temperature. In this way composite films with an average thickness of ~500 μm were prepared. All the materials used were dried in a vacuum oven at 80°C for 24 h before being subjected to any thermal treatment.

Sb_2O_3 as a catalyst for transreactions was supplied by Sigma Aldrich and used in its 'as supplied' form. For this purpose filaments were coated with the powder-like material amounting to 1–2 wt% of the composite.

2.2. Methods of characterisation

The melting temperature values and the melting intervals, which were of particular importance in this study, along with the degree of crystallinity (w_c(DSC)) were determined using a differential scanning calorimeter (DSC) of type DSC Q 1000 of TA Instruments. Typically 6 to 8 mg of material was subjected to scanning at a heating rate of 10°C/min. The w_c(DSC) was calculated by the Equation (1):

$$w_c(\mathrm{DSC}) = \frac{\Delta H_{\mathrm{exp}}}{\Delta H^0} \tag{1}$$

where ΔH_{exp} and ΔH^0 are the experimentally measured and the ideal (for 100% crystalline sample) values of the heat of fusion, respectively. For ΔH^0 the value of 204.0 J /g [27] was used. Scanning electron microscope (SEM) observations were performed on a Philips XL30S instrument with an

acceleration voltage of 5 kV. Images were taken from the fracture surfaces of the composite samples following the mechanical testing.

The mechanical performance of the starting isotropic films of PA 6 (matrix) and the prepared SPC was evaluated in tensile mode using an Instron 5567 machine equipped with a load cell interface, model SN-1000N, gauge length of 50 mm and cross-head speed of 5 mm/min at a temperature of 20°C and 50% humidity. The testing was performed after room conditioning of the samples for two weeks since the absorbed moisture (2.2% as an equilibrium amount) had a dramatic effect on the mechanical properties as demonstrated by Hine and Ward for PA 66 [3]. The testing was performed according to ASTM D882 on 15 mm wide strips, punched by means of a die from the compression moulded films. The results of five specimens were averaged for each sample.

It is important to note that the calculation of the cross-sectional area of the reinforcing filaments via their textile characteristics seemed to be less reliable than the use of microscopes for the same purpose. In addition, because of the unusual thermal behaviour of the samples, the DSC measurements were repeated with newly prepared samples, which were also mechanically tested immediately. In this way, a second series of samples was prepared using as a matrix PA 6 film subjected to slow cooling after compression molding and thus hoping to get a more realistic idea about the reinforcing effect. Since this series of sample was tested mechanically on the same day, it was denoted as '1 day' in contrast to the first series denoted as '14 days'. In both cases the annealed PA 6 yarn was used as reinforcement.

3. Results and discussion

While dealing with single polymer composites an issue of particular importance is the selection of the proper temperature for the thermal treatment leading up to the consolidation of the reinforcing elements without melting them completely. For example, a successful hot compaction of PET textile filaments was performed by Hine and Ward [6] only within 2°C of the T_m of the respective PET sample. In this way, various approaches have been used for the preparation of constructs with as different as possible T_m when the two-constituent approach has been used.

Following the experience of Karger-Kocsis and coworkers on polypropylene [14–16] as well as authors' recent work on PA 66 [24], in the present study it is attempted to prepare PA 6 film with T_m as low as possible using the fact that quenched PA 6 melt crystallises predominantly in the lower melting γ-modification [25, 26]. This film is used later as the matrix in the SPCs prepared afterwards. The role of the reinforcement is played by the high tenacity PA 6 commercial yarn. In order to enhance the subsequent processing an attempt was undertaken to increase the yarn's melting temperature via annealing. The thermal behaviour of the starting materials and the final SPC was tested by DSC measurements – the results are displayed in Figure 1. Surprisingly, all the samples studied show

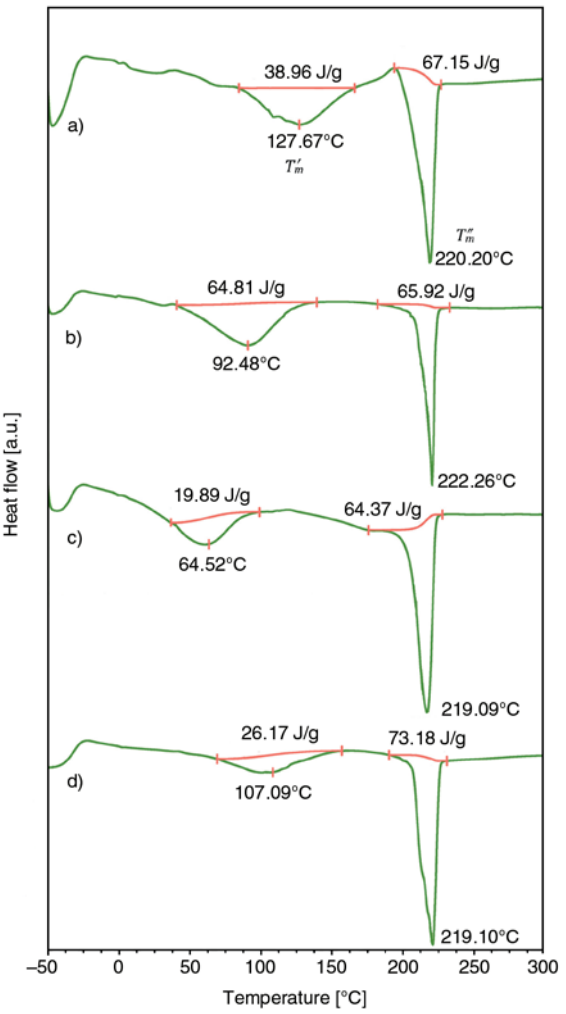

Figure 1. DSC traces of: a) PA 6 film (matrix), b) PA 6 yarn (reinforcement), c) PA 6 yarn (reinforcement) after annealing at 150°C for 360 min in a vacuum, d) PA 6-SPC

two melting peaks, a lower one (T_m') in vicinity of 100°C and a higher one (T_m'') at 220°C.

The observation that the highly drawn PA 6 displays also the presence of a lower-melting modification, Figure 1b, which is still present after annealing of the yarn at 150°C is rather unusual. Even more surprising is the result that the same fraction melts at a lower temperature after annealing (T_m' = 64.5°C instead of 92.5°C for the case without annealing, Figures 1c and 1b, respectively). At the same time, the amount of this lower melting fraction decreases threefold after annealing, see Figure 1. Regardless of the nature of this lower melting fraction, its presence in the two starting materials, the film and the yarn, is very favourable for composite processing since its early melting contributes to the good adhesion quality between the matrix and reinforcement.

It is quite evident that such a thermal behaviour is not a typical one for a neat homopolymer. One of the possible explanation for this observation is that the samples subjected to DSC analysis do not represent a neat homopolymer, but a polymer blend. Many companies are using this approach for getting uncommon for the respective homopolymer properties. Just for polyamides it is known that the company EMS, Germany, blends various polyamides, thus demonstrating unusual for the neat polyamide properties.

The clarification for this uncommon thermal behaviour could be a subject of an independent study as such a task is beyond the frame of this study because the melting parameters of the respective matrix and reinforcement were of interest only for selecting the proper processing temperatures. The latter has to be in such a range, where a complete melting of the reinforcement is excluded. As far as the matrix is concerned, there is no such limitation – the further the melting progresses, the better is the result. From this point of view, the 'unusual' thermal behaviour of the matrix and reinforcement, regardless of the reasons for such a behaviour, seems to be very favourable for manufacturing of single polymer composites, what is the main task of this study.

It is to be noted that as the relevant analysis (X-ray scattering) is missing, statements regarding polymorphic modifications might be hypothesis. However, notwithstanding this lack of evidence, the primary parameter of this study is the melting temperature.

The final PA 6-based SPC also demonstrates a two melting-peak phenomenon, Figure 1d, where the first one shows the same crystallinity as that of the annealed yarn (~10%), while the second peak is characterised by the highest degree of crystallinity (w_c = 36%), Table 1.

SEM images of the PA 6 yarns, which have been used as reinforcement are shown in Figure 2a, whereas the cross-sections of the final PA 6 single polymer composite at progressing magnifications are depicted in Figures 2b–2d. It is evident that the textile filaments are very homogeneous with respect to their diameters being around 50 μm, Figure 2a. The composite film clearly demonstrates a layered structure comprised of two outer film layers and a layer in-between of the uniaxially aligned yarn filaments. What is particularly important for

Table 1. Thermal (DSC) data (first peak of melting T_m', second peak of melting, T_m'', and degree of crystallinity, (w_c) as well as mechanical test data (tensile modulus, E, and ultimate tensile strength, σ_{uts}) of the PA 6 matrix, PA 6 yarn reinforcement, PA 6 single polymer composite (PA 6-SPC) with and without catalyst, all averaged from 5 specimens

No	Material	Thermal data [°C]		w_c [%]		Mechanical data			
						E [GPa]		σ_{uts} [MPa]	
		T_m'	T_m''	w_c'	w_c''	14 days	1 day	14 days	1 day
1	PA 6 film (matrix)	127.67	220.20	19.10	32.92	0.86 ± 0.3	1.5 ± 0.07	24.63 ± 2.4	47.75 ± 3.1
2	PA 6 yarn (reinforcement)	92.48	222.26	31.77	32.31	3.29 ± 0.2	–	760.8 ± 41.5	–
4	PA 6-SPC (without catalyst)	107.09	219.10	12.83	35.87	2.75 ± 0.2	4.04 ± 0.05	102 ± 20.4	271.52 ± 42.4
5	Improvement of PA 6-SPC (without catalyst) [%]	–	–	–	–	220	169	314	470
6	PA 6-SPC (with catalyst)	–	–	–	–	2.97 ± 0.51	5.31 ± 0.1	122.3 ± 14.4	359.07 ± 77.3
7	Improvement of PA 6-SPC (with catalyst) [%]	–	–	–	–	245	254	395	650

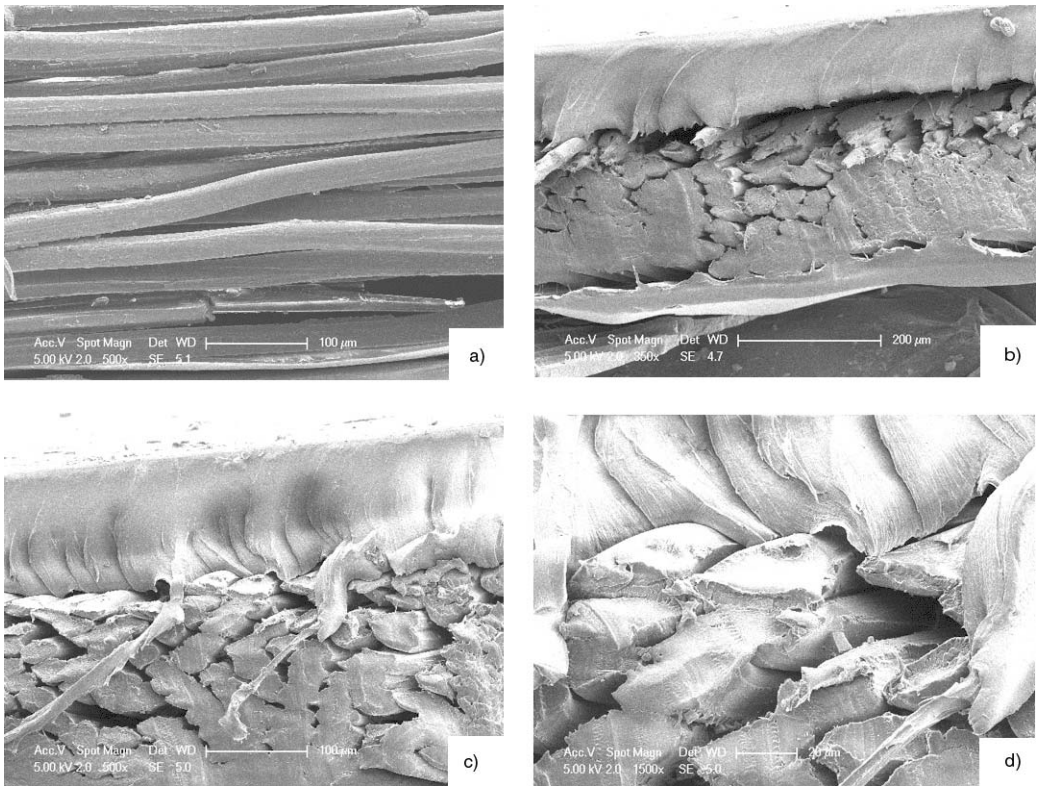

Figure 2. SEM micrographs of: a) PA 6 yarn (reinforcement), b)–d) cross section of PA 6-SPC at increasing magnifications

this reinforcing layer is the fact that during the hot pressing at the selected temperature, the fiber surfaces were melted resulting in the traditional hot compaction. Obviously, this process was enhanced by the fact that even in the highly drawn PA 6 material crystalline species with very low melting temperature (T_m' = 92.5°C and T_m' = 64.5°C after annealing, Figures 1b and 1c, respectively) were present.

The matrix film of the SPC preserved its homogeneity and did not penetrate into the filaments. In fact, in the present case one deals with a layered structure of the composite material as a result of the combination of the two processes, hot compaction and film stacking, Figures 2b–2d. As demonstrated by Hine *et al.* [9], such a combination of film stacking with hot compaction gives a better overall balance of mechanical properties and a wider temperature range for processing, compared to a standard hot compaction procedure without a film. Another advantage of this combination is the better wetting of the reinforcement compared to the traditional film stacking process, due to the partial melting of all the fiber surfaces [9]. The fact that the used PA 6 comprises a low-melting crystalline fraction (T_m' = 127.6°C, Figure 1a, amounting to 30% of the film mass, Table 1) also contributed in the same direction. The same holds for the reinforcing fibers (Figures 1b and 1c, Table 1). These low-melting crystalline fractions of the two constituents ensure good compaction and wetting between the composite elements during the hot pressing.

Stress-strain curves of the starting materials, the PA 6 film and the yarn as well as those of the final SPC are shown in Figure 3. The SPC samples were prepared in the presence or absence of a catalyst enhancing the transreactions. Results for the two series of samples, the dry (1 day) and wet (14 days) are given; the enlarged portions of the stress-strain curves used for the evaluation of the E modulus are also shown.

The reason for the experiments with a catalyst may be attributed to the well known fact that the condensation polymers (polyesters, polyamides, etc) undergo additional condensation and transreactions, also called exchange reactions if the appropriate conditions (temperature, vacuum, duration, catalyst) are available [28]. Since the processing temperature used for manufacturing of SPCs coincides with the temperature interval typical for the occurrence of transreactions, it would seem appealing to explore this opportunity for the creation of

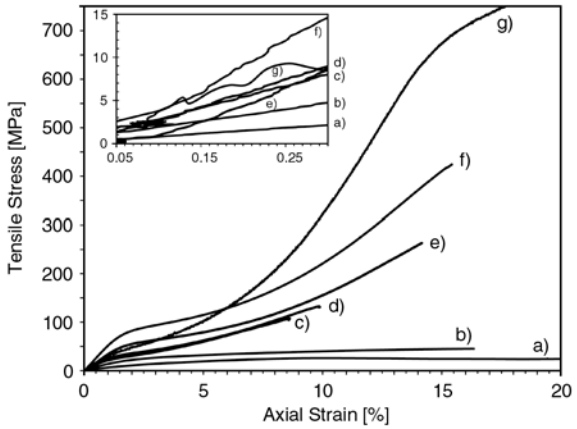

Figure 3. Stress-strain curves and their enlarged sections in the axial strain interval between 0,05 and 0,25% (insertion) of: a) 14 days PA 6 matrix, b) 1 day PA 6 matrix, c) 14 day PA 6-SPC without catalyst, d) 14 day PA 6-SPC with catalyst, e) 1 day PA 6-SPC without catalyst, f) 1 day PA 6-SPC with catalyst, and g) PA 6 yarn

chemical bonds between the matrix and the reinforcement and therefore, to reach the ideal case of interfacial adhesion.

Coming back to the tensile testing experiments, Figure 3, it should be noted that the starting materials behave quite differently. While the matrix films, Figures 3a and 3b, show a ductile type of deformation behaviour, particularly the wet sample, Figure 3a, the rest of the samples demonstrate somewhat brittle characteristics, Figures 3b–3g.

Of particular importance in this respect is the failure behaviour of the tested SPCs. The photograph displayed in Figure 4 was taken from a sample after tensile testing. It is quite evident that the expected delamination, being typical for such materials, is missing and a brittle mode of failure is observed.

It is also interesting to have a closer look at the enlarged stress-strain curves for the strain range 0.05–0.25% plotted in Figure 3. A more detailed inspection of these curves shows that the curve for the commercial yarn, Figure 3g, differs from the others with respect of its shape and position. This deviation from the general behaviour of the stress-strain curves in this narrow strain interval could originate from the fact that the sample under testing represents a multifilament yarn, where all the filament do not experience the loading at the same time but, to some extent, subsequently. The stress-strain curves in the insertion were used for the evaluation of the *E* modulus values, while the same curves in the larger strain range (0–20%), gave the strength values. The obtained results are summarized in Table 1.

Figure 4. Photograph of a PA 6-SPC after tensile testing

The PA 6 films have rather modest mechanical properties in contrast to those of PA 6 yarns. The yarns have an *E* modulus value, which is 3–4 times higher, while the tensile strength (σ_{uts}) is even higher, Table 1. The situation changes drastically when layered SPC is prepared – an improvement in the *E* modulus of 200%, and of the σ_{uts} values of 300–400% can be observed as compared to the starting isotropic film.

As expected, the application of transreaction catalyst shows quite impressive results: the improvement in *E* modulus is 30% (for the dry samples) and 8% (for the wet samples) and for the ultimate tensile strength these values are 32 and 20%, respectively, compared to the same samples without catalyst, Table 1. It is worth mentioning that the observation that the wet samples have in average two-fold lower mechanical properties as compared to the dry ones, Table 1, is in a very good agreement with the findings of Hine and Ward for PA 66 [3].

4. Conclusions

It should be noted that the combination of the hot compaction approach along with film stacking represents a promising route for manufacturing single polymer composites with superior mechanical properties. The first results of catalyst application for improving the adhesion quality are also encouraging. Experiments for the optimisation of the described technique with the involvement of other polymer condensates are in progress.

Acknowledgements

The authors would like to thank the Foundation for Research Science and Technology New Zealand for their financial support (Grant No. UOAX 0406).

References

[1] Capiati N. J., Porter R. S.: The concept of one polymer composites modeled with high density polyethylene. Journal of Materials Science, **10**, 1671–1677 (1975). DOI: 10.1007/BF00554928

[2] Ward I. M., Hine P. J., Norris K.: Polymeric materials. British Patent GB 2253420, Great Britain (1992).

[3] Hine P. J., Ward I. M.: Hot compaction of woven nylon 6,6 multifilaments. Journal of Applied Polymer Science, **101**, 991–997 (2006). DOI: 10.1002/app.22771

[4] Yan R. J., Hine P. J., Ward I. M., Olley R. H., Bassett D. C.: The hot compaction of SPECTRA gel-spun polyethylene fibre. Journal of Materials Science, **32**, 4821–4832 (1997). DOI: 10.1023/A:1018647401619

[5] Jordan N. D., Bassett D. C., Olley R. H., Hine P. J., Ward I. M.: The hot compaction behaviour of woven oriented polypropylene fibres and tapes. II. Morphology of cloths before and after compaction. Polymer, **44**, 1133–1143 (2003). DOI: 10.1016/S0032-3861(02)00810-8

[6] Hine P. J., Ward I. M.: Hot compaction of woven poly(ethylene terephthalate) multifilaments. Journal of Applied Polymer Science, **91**, 2223–2233 (2004). DOI: 10.1002/app.13343

[7] Hine P. J., Astruc A., Ward I. M.: Hot compaction of polyethylene naphthalate. Journal of Applied Polymer Science, **93**, 796–802 (2004). DOI: 10.1002/app.20517

[8] Ward I. M., Hine P. J.: The science and technology of hot compaction. Polymer, **45**, 1413–1427 (2004). DOI: 10.1016/j.polymer.2003.11.050

[9] Hine P. J., Olley R. H., Ward I. M.: The use of interleaved films for optimising the production and properties of hot compacted, self reinforced polymer composites. Composites Science and Technology, **68**, 1413–1421 (2008). DOI: 10.1016/j.compscitech.2007.11.003

[10] Teishev A., Incardona S., Migliaresi C., Marom G.: Polyethylene fibers-polyethylene matrix composites: Preparation and physical properties. Journal of Applied Polymer Science, **50**, 503–512 (1993). DOI: 10.1002/app.1993.070500314

[11] Marais C., Feillard P.: Manufacturing and mechanical characterization of unidirectional polyethylene-fibre/polyethylene-matrix composites. Composites Science and Technology, **45**, 247–254 (1992). DOI: 10.1016/0266-3538(92)90086-I

[12] Houshyar S., Shanks R. A., Hodzic A.: The effect of fiber concentration on mechanical and thermal properties of fiber-reinforced polypropylene composites. Journal of Applied Polymer Science, **96**, 2260–2272 (2005). DOI: 10.1002/app.20874

[13] Bárány T., Karger-Kocsis J., Czigány T.: Development and characterization of self-reinforced poly (propylene) composites: Carded mat reinforcement. Polymers for Advanced Technologies, **17**, 818–824 (2006). DOI: 10.1002/pat.813

[14] Karger-Kocsis J.: Verbundwerkstoff aus Polypropylenverstärkung und Polypropylenmatrix sowie verschiedene Verfahren zu dessen Herstellung. German Patent DE 102 37 803, Germany (2007).

[15] Thomas N. A., Singchin S., Karger-Kocsis J: Dynamic mechanical thermal analysis of all-PP composites based on β and α polymorphic forms. Journal of Materials Science, **43**, 3697–3703 (2008) DOI: 10.1007/s10853-008-2593-2

[16] Banik K., Abraham T., Karger-Kocsis J.: Flexural creep behavior of unidirectional and cross-ply all-poly(propylene) (PURE®) composites. Macromolecular Materials and Engineering, **292**, 1280–1288 (2007). DOI: 10.1002/mame.200700180

[17] Hinrichsen G., Kreuzberger S., Pan Q., Rath M.: Production and characterization of UHMWPE fibers LDPE composites. Mechanics of Composite Materials, **32**, 497–503 (1996). DOI: 10.1007/BF02280631

[18] Lacroix F., Lu H-Q., Schulte K.: Wet powder impregnation for polyethylene composites: Preparation and mechanical properties. Composites Part A: Applied Science and Manufacturing, **30**, 369–379 (1999). DOI: 10.1016/S1359-835X(98)00085-2

[19] Ogawa T., Mukai H., Osawa S.: Mechanical properties of ultrahigh-molecular-weight polyethylene fiber-reinforced PE composites. Journal of Applied Polymer Science, **68**, 1431–1439 (1998). DOI: 10.1002/(SICI)1097-4628(19980531)68:9<1431::AID-APP7>3.0.CO;2-C

[20] Fakirov S., Bhattacharyya D., Shields R. J.: Nanofibril reinforced composites from polymer blends. Colloids and Surfaces A: Physicochemical and Engineering Aspects, **313–314**, 2–8 (2008). DOI: 10.1016/j.colsurfa.2007.05.038

[21] Bhattacharyya D., Fakirov S.: Organoclay particulate, and nanofibril reinforced polymer-polymer composites: Manufacturing, modeling and application. in 'Nano- and micromechanics of polymer blends and composites' (eds.: Karger-Kocsis J., Fakirov S.) Hanser, Munich, 167–201 (2009).

[22] Duhovic M., Bhattacharyya D., Fakirov S.: All-PET nanofibrillar composites. Macromolecules, submitted (2009).

[23] Bhattacharyya D., Fakirov S.: Nano/microfibril reinforced single polymer composites: A novel concept. in '2nd International Conference on Multifunctional Materials & Structures, Qingdao, China' accepted (2009).

[24] Duhovic M., Maitrot P., Fakirov S.: Polyamide 66 polymorphic single-polymer composites. The Open Macromolecules Journal, in press (2009).
[25] Aharoni S. M.: n-Nylons: Their synthesis, structure and properties. Wiley, Chichester (1997).
[26] Fakirov S., Avramova N.: Applicability of Gibbs-Thomson equation to nylon 6. Journal of Polymer Science Part C: Polymer Letters, **20**, 635–641 (1982).
[27] Brandrup J., Immergut E. H., Grulke E. A.: Handbook of polymers. Wiley, New York (1999).
[28] Fakirov S. (ed.): Transreactions in condensation polymers. Wiley-VCH, Weinheim (1999).